Project No. 12-3430

Mitigating IASCC of Reactor Core Internals by Post-Irradiation Annealing

---

Reactor Concepts
Research Development and Demonstration

Gary Was
University of Michigan

In collaboration with:
Oak Ridge National Laboratory

Rich Reister, Federal POC
Jeremy Busby, Technical POC

NEUP Nuclear Energy University Programs
U.S. Department of Energy

Final Technical Progress Report
COVER PAGE

Federal Agency to which Report is submitted: DOE NE – Nuclear Energy University Program

Recipient: University of Michigan
Award Number: DE-AC07-05ID14517
Project Number: 3430 NEUP R&D FY 2012
Project Title: Mitigating IASCC of Reactor Core Internals by Post-Irradiation Annealing
Project Period: September 2012 to December 2016

Principle Investigator: Gary S. Was, University of Michigan, gsw@umich.edu, 734-763-4675
Report Submitted by: Gary S. Was, University of Michigan, gsw@umich.edu, 734-763-4675

Date of Report: May 31, 2016
Covering Period: September 2012 to December 2016
Report Frequency: Final

Working Partners: Zhijie Jiao, University of Michigan, zjiao@umich.edu

Cost-Sharing Partners: Jeremy Busby, Oak Ridge National Laboratory, busbyjt@ornl.gov
Maxim Gussev, Oak Ridge National Laboratory, gussevmn@ornl.gov

DOE Project Team: DOE Technical POC – Jeremy Busby, busbyjt@ornl.gov
DOE Federal POC – Richard Reister, Richard.reister@nuclear.energy.gov

Executive Summary

This final report summarizes research performed during the period between September 2012 and December 2016, with the objective of establishing the effectiveness of post-irradiation annealing (PIA) as an advanced mitigation strategy for irradiation-assisted stress corrosion cracking (IASCC). This was completed by using irradiated 304SS control blade material to conduct crack initiation and crack growth rate (CGR) experiments in simulated BWR environment. The mechanism by which PIA affects IASCC susceptibility will also be verified. The success of this project will provide a foundation for the use of PIA as a mitigation strategy for core internal components in commercial reactors.

Specifically, this program had the following objectives:

- Evaluate the response of a BWR-irradiated 304L SS following subjection to a range of post-irradiation annealing times and temperatures.
- Investigation of the irradiated microstructure of both the as-irradiated and following selected annealing conditions via both TEM and APT.
- Characterize the evolution of the localized deformation as both a function of the annealing condition and plastic strain.
- Determination of the effectiveness of selected PIA treatments in mitigating the IASCC susceptibility observed through both crack initiation and growth experiments.
- Linkage between the irradiated microstructure, localized deformation, and the IASCC susceptibility as a function of PIA treatments.

To complete these objectives, a total of 12 different annealing conditions were investigated to evaluate the hardening response as a function of annealing time and temperature. Based on this result, four PIA conditions: 500^{o}C: 1hr, 550^{o}C: 1hr, 550^{o}C: 5hr, and 550^{o}C: 20hr; were selected for further microstructural and IASCC susceptibility analysis, in addition to the as-irradiated state. Due to delays in the initial material acquisition, IASCC susceptibility analysis was only completed through a total of 5 crack initiation experiments and 1 crack growth rate experiment, in both simulated BWR-NWC and HWC environments. Predominate factors investigated regarding the PIA-induced changes in IASCC susceptibility include: irradiation hardening, microstructure, both dislocation loops and solute clusters, microchemistry, and localized deformation.

The major outcomes of this research program are summarized as follows:

- PIA treatments greater than 450^{o}C were highly effective in reducing the irradiated-induced microstructural defects in the as-received material.
    - The irradiation hardening for the project material was unaffected by annealing treatments at 450^{o}C, but was incrementally removed at higher temperatures and times, leading to full removal after 600^{o}C: 20 hr.

  - The average dislocation loop size does not change significantly after PIA at 500^{o}C:1h and 550^{o}C, 1 and 5 hr but the number density decreases after PIA. The number density becomes negligible after PIA at 550^{o}C:20h.
  - The number density of both Ni-Si and Al-Cu clusters decreases and the size increases after PIA due to thermal diffusion of solute atoms. The ratio of Ni to Si increases after PIA, due to the higher diffusion of Si relative to Ni.
  - Significant recovery of Cr and Ni segregation was observed after PIA at 550°C:5h but neither Cr nor Ni was fully recovered after 550°C:20h.
- PIA treatments at 500^{o}C: 1 hr, 550^{o}C: 1, 5, and 20 hr were observed to significantly change the deformation behavior during CERT experiments. Furthermore, the 550^{o}C: 20 hr condition was observed to significantly modify the measured localized deformation.
  - The yield stress of the material following PIA treatments was observed to closely correspond to the measured changes in the irradiation hardness.
  - Hardening is best described using a root-mean-square model for superposition of obstacles and was dominated by dislocation loops. A least squares analysis revealed that the hardening coefficient of loops was ~0.2. That for Ni-Si precipitates was less half this value and that for Al-Cu clusters was even smaller.
- PIA treatments at 550^{o}C: 1 hr and 550^{o}C: 5 hr were observed to fully remove the IASCC susceptibility of the as-received material. However, annealing at 550^{o}C: 20 hr showed a susceptibility to IASCC.
  - As compared to other neutron-irradiated experiments reported in the literature, our as-received material was observed to have a moderate IASCC susceptibility with an intergranular fracture of 48.4%. This measure was observed to decrease with increasing annealing, but there was still 20.6% intergranular fracture after 550^{o}C: 20 hr, which appears higher than the observed trend in literature.
  - Reduction in area of the final fracture surfaces was significantly enhanced by the annealing treatments, thus representing an increased ductility of the material and lower IASCC susceptibility following annealing.
  - As the measured CGR of an RCT specimen after annealing at 550^{o}C:20hr seem to be lower than similar as-irradiated specimens at similar K values from literature, thus indicating some mitigation from the PIA.
- From these results, it is apparent that PIA treatments had a significant impact on the irradiated microstructure, dislocation channeling, and cracking susceptibility. While the irradiation hardening and microstructural defect populations were removed in a manner similarly to previous results in literature, the as-received material appeared to be more resistant to the mitigation of IASCC susceptibility as compared to previous literature studies. There was no obvious step change in the irradiated microstructure that could account for the disappearance of IASCC after the 550°C: 1 and 5 hr anneals.

1. Introduction

1.1 Objective

The objective of this project is to utilize post-irradiation annealing (PIA) to identify the key processes responsible for IASCC, thereby establishing the PIA treatment that eliminates sensitivity to IASCC in neutron-irradiated austenitic stainless steels, and providing a foundation for the development of a PIA mitigation strategy for commercial reactors.

1.2 Background

Irradiation-assisted stress corrosion cracking (IASCC) of reactor core internals is a potential lifetime limiting degradation mechanism for LWRs. It has taken on new urgency with the growing interest in extending operating licenses for the current generation of plants to 60 years or beyond. What makes IASCC unique is that it is largely controlled by the persistent damage induced by irradiation. That is, while radiation affects the environment through radiolysis, the onset of cracking in LWR environments is controlled by the radiation-induced defects in the alloy [1]. Post-irradiation annealing (PIA) can partially recover radiation damage, thus potentially mitigating IASCC. Given that code qualification of new alloys could take one to two decades, and that an IASCC-resistant alloy has yet to be identified, PIA is one of the most promising near-term hopes for reducing IASCC in today's LWR fleet and to support life extension beyond 60 years. The benefits of PIA in mitigating IASCC in irradiated austenitic alloys have been demonstrated in a number of studies in the past decades [2]–[9]. These studies have demonstrated that IASCC is significantly reduced in irradiated austenitic alloys after PIA for specific time-temperature combinations, including full removal of IASCC susceptibility after PIA conditions as low as 500°C: 45 min. Furthermore, these studies incorporated irradiation by both neutrons and protons, for which agreement is excellent.

However, the linkage between reduction in SCC susceptibility and changes in microstructure is incomplete. For example, at 500ºC, the density of dislocation loops and possibly radiation-induced precipitates can be seen to decrease by 20-50% after 30 min, by >50% after 90 min and full recovery after 300 min, and the 600°C treatment will also substantially remove RIS after a few hours. Yet IASCC can be "healed" after only 45 min at 500°C. Further, all these studies were performed on tensile bars. There is only one study on crack growth in an annealed sample and the results were inconclusive due to a lack of microstructure analysis [10]. Therefore, it is not known whether PIA is effective in recovering the low crack growth rate (CGR) of the unirradiated alloy. Regarding the mechanism of IASCC and the role of PIA in reducing it, while many effects of irradiation have been proposed (radiation-induced sensitization, radiation hardening, etc.) localized deformation has emerged as a major contributor to IASCC [11]–[16], and some of the most recent data [13] has shown a stronger correlation between IASCC and localized deformation (as measured using the weighted average channel height on the sample surface), than with any other figure of merit. The localization of deformation into discreet channels that intersect grain boundaries and the surface provide a link to the observed cracking behavior that is lacking in most other proposed causes. However, all the previous PIA studies on neutron-irradiated material were conducted *before* the role of localized deformation in IASCC was appreciated. Thus, no data exists on whether PIA is effective in reducing localized deformation. Recent advances in microstructure analysis using atom probe tomography (APT) have also led to the discovery that Ni-Si precipitates and solute clusters in irradiated stainless alloys can be annihilated in the dislocation channel, which may also affect the degree of localized deformation [17]. Note that the Si content remains high in the channel, therefore, therefore it is hypothesized that PIA could lead to a reduction in the degree of localized deformation by removal of dislocation loops, defect clusters or radiation-induced precipitates, thus resulting in mitigation of IASCC.

In summary, the exact mechanism by which PIA eliminates IASCC is not clear since: the tools to investigate it were not available when these studies were conducted, the mechanisms controlling IASCC were not well understood, and no data exists on whether PIA can reduce the crack growth rate. With better tools, a more complete picture of the crack initiation and crack growth processes, and a better knowledge of the role of localized deformation in the IASCC process, we will be able to determine the way in which PIA reduces IASCC susceptibility and set the stage for development of a mitigation strategy for LWR core materials.

2. Experiment

2.1 Materials and Specimens

The specimens used for this project were obtained from through Studsvik Nuclear AB, having been originally irradiated during the operation of the Barsebäck 1 BWR in Sweden as Control Rod #1690. This section outlines the material composition and irradiation history as well as the experimental specimen geometries and the applied post-irradiation annealing treatments.

2.1.1 Alloy Composition

Control Rod #1690 was manufactured by ASEA-ATOM (now Westinghouse Electric Sweden AB) of 304L stainless steel (SS) by Vereinigte Edelstahlwerke AG and was delivered in a solution-annealed condition; no other heat treatments were performed during the fabrication of the control rod. The chemical composition of the material is shown in Table 2-1, in which the compositions are given in weight %. The chemical composition was determined both by ladle analysis of the non-irradiated material during fabrication and by an APT characterization of the irradiated material [18]. The two chemical compositions are quite comparable except for impurity traces of both aluminum and copper as seen by the APT.

2.1.2 Irradiation Condition

Control Rod #1690 was used in the operation of the Barsebäck 1 BWR in Sweden, but was withdrawn from the core for the entirety of its use, thus it was exposed to a lower neutron irradiation flux than normal. A summary of the irradiation history is shown in Table 2-2.

2.1.3 Post-Irradiation Annealing Treatments

Annealing treatments were conducted in an air furnace at varying times and temperatures: 450 – 600^{o}C for 1- 20 hrs. A total of twelve unique annealing conditions were performed, as well as two repeated conditions: 500^{o}C: 1hr and 600^{o}C: 5hr, to verify the consistency of the annealing treatment. The furnace used for the annealing treatments demonstrated a high temperature stability and there was a good agreement between the built-in and secondary thermocouple. The specimens were all removed from the furnace at ±2 min of their desired timing. Table 2.3 outlines the entire list of irradiated specimens that were utilized for this project as well as their applied annealing treatments. Note that tensile specimen T-2 was not shipped as it was damaged during the production of the specimen, while T-3 was irreparably damaged whilst cutting the tensile heads from the specimens. Specimen T-8 remains as a back-up specimen in case a problem develops with one of the selected specimens.

2.1.4 Tensile Bars and RCT Specimens

Studsvik Nuclear AB provided documentation detailing the fabrication of the irradiated specimens. A total of 5 RCT and 12 tensile samples were delivered, as well as an additional 18 smaller blanks which were left over from the fabrication of the other specimens. The RCT samples were fabricated per specifications, as shown in Figure 2-1 and Table 2-4, apart from RCT1 shown in Figure 2-2. RCT1 has a small notch at the back due to the limited source material and the machining of sample T3. However, this defect is not expected to affect the stress intensity at the crack tip, thus the sample is still considered useable. The tensile samples were machined in accordance with the initial design, shown in Figure 2-3 and Table 2-5. Although 10 tensile samples were originally ordered, 12 were included in the shipment, as T-1 and T-3 were machined incorrectly, i.e. they had misaligned flats along the gauge sections. It was also noticed that three samples had different sized flats, resulting from improper centering of the specimen during machining. T-5 was machined such that it only had a single large flat and one sample was also found to be slightly bent, as shown in Figure 2-4. In summary, of twelve tensile samples that were shipped, six were machined per specifications, three had flats which were not properly centered, two had misaligned flats, and one was slightly bent.

2.2 Microstructure Characterization

This section outlines the preparation procedure and analysis techniques used for the microstructural characterization of the material for this research project, including micro-hardness, TEM, and APT analysis.

2.2.1 Micro-Hardness Measurement

Micro-hardness measurements were made to evaluate the bulk changes in the irradiated microstructure. Prior to the measurements, specimens were mechanically polished with a succession of finer grits, ending with a 3 μm diamond polish. The specimens were then electropolished at room temperature for 15 seconds at 30V using a commercial Struers A2 solution at LAMDA at ORNL. After electropolishing, provided no defects or scratches were observed, the specimens were measured using a Vickers micro-hardness indenter at ORNL. Each specimen was measured at a load of 200 gf, with at least 30 independent indents, whereas the average hardness and standard deviation was then recorded.

2.2.2 Transmission Electron Microscopy (TEM) Analysis

TEM foils for dislocation loop analysis were prepared by jet thinning using a commercial Struers A2 solution at LAMDA at ORNL. Dislocation loops were examined with rel-rod technique using JEOL 2100 STEM at ORNL. Dislocation loops were imaged at different locations under the [110] zone axis. The number of loops characterized is dependent on the number density and in the as-irradiated condition, 670 loops were characterized.

Radiation induced segregation (RIS) was assessed in the BWR irradiate 304L SS. Energy-dispersive X-ray Spectroscopy (EDS) maps were taken from random high angle boundary using the FEI F200X S/TEM instrument equipped with ChemiSTEM at the LAMDA laboratory at ORNL using a map size of 1024x1024 pixels with a resolution of ~0.23 nm/pixels with a probe full width half max of ~1.5nm. Each scan had a duration of one hour with more than 100,000 counts/sec with dead times from 1-6%. ChemiSTEM has a much higher counting rate compared to typical STEM/EDS. The qualitative x-rays counts were converted to quantified weight percentages using the Bruker Esprit© 1.9 software package, which uses the Cliff-Lorimer calculations for each pixel. Prior to EDS measurement, grain boundary was tilted to edge-on position. Due to the limitation of available grain boundaries for RIS, only one grain boundary was measured, but multiple EDS maps were obtained from different segments of the grain boundary.

2.2.3 Atom Probe Tomography (APT) Analysis

Precipitates/solute clusters were analyzed using the atom probe tomography. Needle-shaped APT specimens were prepared by the standard lift-out method and focused ion beam milling using Quanta 3D at ORNL. Specimens were prepared from the electropolished 3-mm disk. Prior to the lift-out procedure, Pt was deposited to protect the material from ion beam damage. A final 5 kV clean-up procedure was utilized to minimize the Ga damaged regions and reduce the tip radius to ~50 nm. About 6 APT tips were made for each condition for APT analysis. APT specimens were analyzed using a LEAP-4000XHR microscope at the University of Michigan operated in electrical mode with a voltage pulse fraction of 20%. Specimen temperature was maintained at 50 K and detection rate was kept constant at 0.005 atom/pulse.

Reconstruction of the relative atom positions from the raw data was performed using the commercial software, IVAS 3.6.4 from CAMECA™. Solute clusters were analyzed using the maximum separation method. The nickel-silicon solute clusters were defined by the tenth order spacing of silicon atoms, whereas a suitable d_{max} (the maximum separation of tenth-order silicon atoms) was selected to best separate the clustered and randomized silicon atoms based on the spacing distribution. The aluminum-copper solute clusters were defined by the fourth order spacing of aluminum atoms, whereas a suitable d_{max} (the maximum separation of fourth-order aluminum atoms) was selected to best separate the clustered and randomized aluminum atoms based on the spacing distribution. For both cluster types an N_{min} was chosen equal to the maximum cluster size observed for a randomized experimental APT data.

2.3 Test Systems and Procedures

2.3.1 Constant Extension Rate Tensile (CERT) Test System

The CERT experiments required for this project were performed using the IM1 autoclave system in the Irradiated Materials Testing Laboratory (IMTL) at the University of Michigan. The IM1 loading system can strain up to four tensile bar samples simultaneously, while the application of load is controlled using a 50 kN servo motor. A linear variable differential transformer (LVDT) is mounted on the crosshead to measure displacement. Four pull rods connect each sample to the crosshead, and load is measured on each by a load cell. Each of the pull rods are sealed at the feed-through into the autoclave with a self-energizing graphite seal with an internal spring that expands under pressure. Each pull rod is connected to an Inconel 625 sample loading fixture. Electrical insulation is provided by zirconia washers located in the loading fixtures. After loading the specimen, the autoclave body is sealed to the autoclave head, thus preventing any leakage during the experiment.

2.3.2 Tensile Bar Annealing and Surface Preparation

To ensure the later success of crack initiation testing on the CERT tensile specimens for this project, multiple preparation steps were first required. Due to the high dose rates of the CERT specimens, all preparation work was completed at the ORNL hot cell facilities, largely using manipulators. The difficultly of completing the preparation work is exponentially increased within the hot cell facilities, as shown in Figure 2-5.

Prior to the annealing treatment of the designated tensile specimens, it was necessary to complete several cutting operations on the heads of the tensile specimens. The goal of these cutting operations was two-fold: first, the cutting removes ~50% of the specimen mass, thereby reducing the total dose rate; second, the cutting operation creates several small specimen slices that can be used to analyze the pre- and post-annealed hardness of the tensile specimens.

Following the cutting operations on the tensile specimens, the annealing treatments were performed. Prior to loading the specimens, the furnace was set to the required temperature, as determined by the average of both the built-in furnace thermocouple and a secondary thermocouple, and allowed to stabilize. Each of the tensile specimens were loaded into a stainless steel folder, which would act as an oxygen getter, with a corresponding slice specimen, for later hardness testing, while the RCT specimen was loaded into a separate folder.

The furnace was then opened and the three foil packets, i.e. two tensile specimens and one RCT, were loaded into the furnace, centered beneath the secondary thermocouple, after which the furnace door was closed. Upon closing the door, the temperature began to quickly return to the desired temperature, and the annealing time was recorded to begin at the point at which 95% of the desired temperature was reached, this timing was generally 3-5 minutes after closing the furnace door. After the desired annealing time was reached, the furnace was opened and the foil packets were then removed. These packets were then allowed to air cool back to room temperature.

During the original machining of the tensile specimens, EDM was used to cut the parallel flats on opposing sides of the gauge section. EDM leaves a thin, amorphous recast layer, which may affect the cracking behavior in a simulated-BWR environment. As such, the gauge section flats were mechanically polished to remove the EDM recast layer. However, due to the high radioactivity of the specimens this procedure was completed in a hot cell facility using manipulators. First both tensile heads were clamped in a small vice, to prevent any possible bending, and a polishing paper was carefully moved across the gauge flats. An 800-grit sandpaper was first utilized to remove the

EDM layer, while a 1200 grit paper was utilized to prepare the surface for a later electropolishing. The removal of the EDM layer was monitored by the usage of an in-cell camera.

Electropolishing was completed on the tensile specimens to create a final surface finish satisfactory for CERT testing in both simulated BWR environment and an inert argon environment. The electropolishing operation was completed in the hot cell fume hood. The electropolishing setup was quite simple, consisting of a power supply, a grid cathode, and a beaker of electrolyte. The electropolishing will be completed at 30V and consist of four 15 sec polishing increments, between each of which the specimen was flipped. This procedure was expected to remove roughly 20 μm of material based on prior experiments. After electropolishing, each specimen was observed via an optical microscope to verify a good surface quality.

2.3.3 CERT Test Procedure

All CERT tests were conducted in a simulated boiling water reactor normal water chemistry (BWR-NWC) environment. During each straining, system water pressure was maintained at 9.7 MPa and temperature at 288^{o}C, while the outlet dissolved oxygen and conductivity were maintained at 200 ppb and 0.2 μS/cm, respectively.

After pressurizing and achieving the desired temperature for the intended environment, the system was allowed to stabilize until conductivity had dropped below 0.2 μS/cm. Upon stabilization, dissolved gas was added to the primary water column and the target concentration was achieved by regulating the main column pressure with a back-pressure regulator. Following gas addition, the environment stabilized for an additional period of 12 hr before commencing straining. During this 12 hr period, conductivity control was initiated once the vessel outlet water conductivity again dropped below 0.2 μS/cm. Conductivity was controlled by adding small amounts of dilute H_2SO_4 to the primary water column with the peristaltic pump, which was set to operate whenever conductivity would decrease below the target.

Due to the crosshead arrangement, non-irradiated type 304L SS tensile bar specimens were used to occupy empty loading locations and provide load balance at the system crosshead. These specimens were selected such that they would have a similar yield stress as the irradiated specimen currently being examined.

Prior to straining, a preload of 20 MPa was applied to each specimen. At the end of the 12 hr stabilization period, straining was initiated by moving the crosshead with the servo motor. This displacement was completed at a rate of 1.65×10^{-7} in/s for all experiments, which corresponds to a strain rate of $3.0 \times 10^{-7}\ s^{-1}$. During the stabilization period and straining, all environmental and stress-strain data were recorded every 30 sec using the LabView data acquisition program. Recorded data includes inlet and outlet water pressure, inlet and outlet water conductivity, outlet dissolved oxygen, vessel internal and preheater temperature, LVDT displacement, and load cell readings.

2.3.4 Dislocation Channeling Characterization

As previously discussed, increased localized deformation has been closely correlated with increasing cracking susceptibility [13], however, the change in localized deformation following PIA treatments has never been measured for a neutron-irradiated material. Furthermore, more recent studies [14]–[16], have indicated that dislocation channels that are discontinuous at grain boundaries have a higher propensity of crack initiation.

For this study, the straining experiments were completed in small increments, such that we could more precisely identify point of crack initiation and study the development of the localized deformation. After each stress/strain increment the specimen was removed from the autoclave were examined using a JEOL JSM-6480 SEM. This examination measured any plastic strain through fiducial markings, as well as recording any sites of crack initiation and changes in the localized deformation.

The dislocation channel characterization focused on the changes in both the total dislocation channel density and the density of channel-grain boundary interaction sites, which were characterized as either continuous or discontinuous, with increasing plastic strain. A continuous channel-grain boundary site refers to a location where a dislocation channel intersects a grain boundary, but is then able to transmit across said boundary, i.e. a continuous channel. Whereas a discontinuous interaction site is one where the channel was unable to transmit across the grain boundary. By comparing the densities of both continuous and discontinuous interaction sites, one can measure the relative propensity that a condition has for forming continuous channels, and how this may change with both PIA treatments and additional strain.

Following each stress/strain increment both the gage flats were fully imaged at 500x magnification. This magnification allowed for a balance of both image quality and imaging time, while the large-scale imaging also allows for a spatial correlation of images following each additional strain increment.

2.3.5 Crack Growth Rate (CGR) System Overview

The CGR testing system, IM5 is similar to the IM1 system used for CERT testing as concerns the water loop and general operation. However, the IM5 system also has the addition of an AT5 based DCPD system used to control *K* value and monitor the crack growth rate. Due to the planned testing of highly irradiated specimens, IM5 was designed as a mobile system, such that an experiment could be performed in a hot cell, thus significantly reducing the dose to the operator. As such the whole autoclave containing the RCT sample was moved into a hot cell for testing, while the water loops and controls remained outside of the hot cell for easy access during the experiment. Figure 2-6 shows the images of test system.

2.3.6 CGR Specimen Preparation and Loading

Due the annealing treatment, a slight oxide layer was developed on the RCT specimens that underwent PIA treatments, despite the stainless steel oxygen getter that was utilized. This oxide layer would be detrimental to the later spot welding of the DCPD probes, thus it had to be removed via mechanical polishing. In the hot cells at ORNL the RCT specimens were mounted onto a specially designed apparatus, which slowly rotated the specimens while an 800-grit sandpaper was applied to the specimen; special attention was also given to front flats of the RCT specimens. After completing the annealing and mechanical polishing the RCT specimens were shipped to the University of Michigan.

Crack growth was measured using the reversed Direct Current Potential Drop (DCPD) technique, which has long been used for crack growth monitoring in high temperature water environments. As shown in Figure 2-7 (a), the DCPD monitoring system consists of a DC power supply, relays, nano-volt meter, data acquisition unit, servomotor and Skala controller. DC power supply provides stable current (2.5 A for 0.5 T RCT) to a specimen. The current is reversed once per second through solid-state relays to correct for thermocouple effects. The current and potential probe leads were spot-welded to the RCT specimen as shown in Figure 2-7 (b). The potential drop resulting from crack propagation in the specimen is measured by a nano-volt meter. Data acquisition and instrument control are all integrated in a DOS program called AT5, which was developed by Dr. Peter Andresen at GE Global Research Center. A data processing program called HIKO, based on DotNetFX2.0 was also used in this study.

The current leads and potential probes need to be spot welded onto the RCT sample for DCPD measurement. Due to the radioactivity of neutron-irradiated samples, the welding should be implemented in hot cell via manipulator. Figure 2-8 shows the RCT sample after spot welding.

2.3.7 CGR Experimental Conditions and Crack Growth Procedures

CGR tests were conducted in a BWR environment, including both NWC and HWC. Temperature and pressure of the testing system are 288°C and 10.3 MPa, respectively. The water in a 3.5 L autoclave was refreshed three times per hour with a flow rate of 180 mL/min. The conductivity of inlet DI water was 0.056 μS/cm. Inlet dissolved oxygen (DO) was controlled at 2 ppm for NWC and dissolved hydrogen (DH) was controlled at about 100 ppb for HWC. DO and conductivity of inlet/outlet water were continuously monitored using a Thornton 770Max DO/conductivity meter.

The electrochemical potential (ECP) of the RCT specimen was continuously monitored during the CGR test with a Cu/Cu_2O reference electrode. At the same time, the redox potential between a 1.0

cm^2 Pt flag and the reference electrode was also recorded. The measured potentials were converted to potentials vs standard hydrogen electrode (SHE) by subtracting 0.273 V.

During heating, the DCPD potential reading increases with temperature because of the increasing resistivity of metallic materials. So, the initial crack length to sample width ratio, *a/W*, from direct measurement should be recorded and reset in AT5 once the DCPD potentials stabilize at the target temperature. If a fatigue pre-crack was introduced in air at room temperature before beginning a stress corrosion cracking test in high temperature water. In this case, the final *a/W* in air needs to be set as the initial *a/W* prior to growing the crack at the testing temperature.

After loading the sample in the autoclave, the current and potential wires for DCPD measurement were spot-welded to the CT specimen as described above. The wires in each pair were twisted in order to cancel magnetic fields. A thermocouple for temperature control was placed at the crack plane in the autoclave. Once the temperature, conductivity and DO reached the target levels, the *a/W* for DCPD readings was reset to the initial value. After that, the system was ready for controlling *K* on sample. The tare load from high pressure water was accounted for in AT5. The temperature inside the autoclave, inlet and outlet pressure, inlet and outlet conductivity, and inlet and outlet DO were continuously recorded during the entire test period.

The crack was introduced by fatigue in the testing environment, i.e. in-situ fatigue pre-cracking. The maximum *K* was slightly lower than that being used for the next constant *K* step. At the beginning of the test, low loading ratio *R,* and high frequency *f*, were used to introduce cracking at a fast rate and to leave beach marks as evidence on the fracture surface for tracking the crack growth in each step. Later, to initiate the transition from TG to IG, *R* was decreased to 0.6 and the frequency was lowered from 0.1 to 0.01, and then to 0.001 Hz. After 0.001 Hz fatigue, a trapezoidal load form was applied with a holding time of 9000 seconds. Subsequently, constant *K* control was started.

The CGR is highly dependent on the *K* value applied on the sample. To reliably measure the CGR at a certain *K* value, the value of *K* should be kept constant during the test. Per ASME standard E-399, *K* is a function of *a/W* and load:

$$K = \frac{P}{B\sqrt{W}} f\left(\frac{a}{W}\right) \tag{2.1}$$

where:

$$f\left(\frac{a}{W}\right) = \frac{\left(2+\frac{a}{W}\right)\left[0.76+4.8\frac{a}{W}-11.58\left(\frac{a}{W}\right)^2+11.43\left(\frac{a}{W}\right)^3-4.08\left(\frac{a}{W}\right)^4\right]}{\left(1-\frac{a}{W}\right)^{3/2}} \tag{2.2}$$

For which *P* is applied load, *B* is the sample thickness, *W* is the sample width and *a* is the crack length. So, the applied force should be adjusted as the crack grows to maintain a constant *K*. AT5 has a built-in auto *K* control function which can adjust the applied load automatically once a minimum increase (set to 0.01 in the program) in *a/W* is achieved.

It is very important to sustain the crack growth when changing the *K* value. d*K*/d*a* control was used for a smooth transition for both increasing and decreasing *K*. Trapezoid waveform was normally used during *K* transition. AT5 also has this built-in function. The rate of change of *K* with *a* (d*K*/d*a*) is calculated based on the *a/W* and *K* values from two neighboring steps. As the crack grows, a change in *K* will be made based on the d*K*/d*a* value. The threshold for the *K* change was set to 0.02 ksi·in$^{1/2}$.

When the test was finished in high temperature water, the autoclave system was cooled to room temperature. The sample was cracked open at room temperature using fatigue loading. To minimize the plastic deformation at the crack front formed in the environment, *K* was controlled at the same (or lower) level as that last used in high temperature water. After growing a post-test crack about 0.5 mm, the RCT specimen was fatigued at high frequency until it broke.

2.3.8 Post-Failure Fractography

Fractography was performed on each fractured tensile bar following the CERT test using a JEOL JSM-6480 SEM. Low magnification images of the gage surface were taken to indicate the locations of IG fracture and secondary cracking, while the edges of the main IG crack and secondary cracks were imaged at higher magnification.

The fracture surfaces of each specimen were also examined in detail to characterize the nature of failure by viewing the fracture surface perpendicular to the tensile axis. Regions of intergranular (IG), transgranular (TG), mixed (IG+TG), and ductile type failure were identified. Higher magnification imaging (>500x) was performed in regions of note.

Reduction of area (RA) was calculated using the total area of the fracture surface viewed perpendicular to the tensile axis. The area of the fracture surface was determined using the Image J™ imaging software program particle analysis feature. The RA is determined by dividing the difference in area between the fractured surface (viewed parallel to the tensile direction) and the original cross-sectional area by the original cross sectional area.

Regions of IG, mixed, TG, and ductile fracture were characterized by area and expressed as an area-based percentage of the total fracture surface. Using the Image J™ program, each fracture regions were cut from the overall view of the fracture surface and area was determined using the particle analysis feature of the software. This area divided by the total fracture surface area yielded the percentage of fracture type.

Similarly, following the post-test fracture of RCT samples, the failed sample was removed and the fracture surfaces were examined by a JEOL JSM-6480 SEM. The fracture surface was examined for evidence of each step change during the crack growth rate test. The morphology of the fracture surface, especially transgranular (TG) or intergranular (IG) features and the transition between TG and IG, was confirmed. The area of intergranular fracture surface was measured and divided by the width of sample to calculate the average length of IGSCC growth. The measured crack length from fracture surface analysis was compared with that from DCPD measurement. The ratio between them was used as correction factor for crack length and crack growth rate.

Table 2-1: Chemical composition of the 304L stainless steel both of the un-irradiated material via ladle analysis and the irradiated material via APT [18] in wt%. The primary difference is the addition of Al and Cu impurities seen by APT.

Method	C	Si	Mn	Cr	Co	N	Ni	P	S	Al	Cu	Fe
Ladle (Un-irradiated)	0.025	0.30	1.09	18.35	0.029	0.024	10.57	0.013	0.003	-	-	Bal.
APT (Irradiated)	0.035	0.40	1.13	18.34	0.15	-	11.6	0.02	0.001	0.02	0.12	68.01

Table 2-2: Summary of the irradiation damage for Control Rod #1690; as this control rod was withdrawn from the core for the entirety of its service life, it was exposed to a rather low neutron flux, though for an extended period of time, culminating in a total damage of 5.9 dpa.[1]

Control Rod Id.	Time (hrs.)	Flux ($n/cm^2 \bullet s$) (E> 1 MeV)	Fluence (n/cm^2) (E> 1 MeV)	Dose(1) (dpa)
1690	95608	$1.2 \bullet 10^{13}$	$4.16 \bullet 10^{21}$	5.9

(1) Assuming 1 dpa = $7 \bullet 10^{20}$ n/cm^2 (E > 1 MeV)

Table 2-3: Overview of the specimens utilized for this project, as well as their applied annealing treatments.

Specimen Type	Specimen ID	Annealing Condition
Sample Blank	5	500°C: 1hr
Sample Blank	5A	450°C: 20hr
Sample Blank	9	450°C: 5hr
Sample Blank	9A	450°C: 1hr
Sample Blank	11	550°C: 1hr
Sample Blank	11A	600°C: 20hr
Sample Blank	15	550°C: 5hr
Sample Blank	15A	550°C: 20hr
Sample Blank	16	500°C: 20hr
Sample Blank	16A	600°C: 5hr
Sample Blank	17	600°C: 1hr
Sample Blank	17A	600°C: 5hr
Sample Blank	18	500°C: 1hr
Sample Blank	18A	500°C: 5hr
Tensile	T1	500°C: 1hr
Tensile	T2	Unusable
Tensile	T3	Unusable
Tensile	T4	As-Irradiated
Tensile	T5	500°C: 1hr
Tensile	T6	As-Irradiated
Tensile	T7	550°C: 5hr
Tensile	T8	As-Irradiated
Tensile	T9	550°C: 20hr
Tensile	T10	550°C: 5hr
Tensile	T11	550°C: 1hr
Tensile	T12	550°C: 20hr
Tensile	T13	550°C: 1hr
RCT	RCT1	500°C: 1hr
RCT	RCT2	As-Irradiated
RCT	RCT3	550°C: 20hr
RCT	RCT4	550°C: 5hr
RCT	RCT5	550°C: 1hr

Table 2-4: Dimensions of the fabricated RCT specimens in comparison to their nominal values and tolerances. Several minor deviations are noted but were judged to have no or little effect on test results.

Specimen ID	W	C	a	B	B_n	b_1 b_2	D_1 D_2	h_1 h_2	H_1 H_2	H_3 H_4	H_1+H_2 H_3+H_4
Nominal	16	20	6.4	8	7.2	.4	4	4.4	10.8	10.8	21.6
Tolerance	±.08	±.24	±.24	±.16	±.16	-	±.08	±.08	±.08	±.08	±.16
RCT1	16.30	19.89	6.83	8.08	7.19	.47 .35	4.04 4.01	4.51 4.27	10.87 10.81	10.78 10.90	21.68 21.68
RCT2	16.14	20.03	6.43	8.05	7.36	.43 .32	4.06 4.13	4.43 4.38	11.19 10.45	11.23 10.42	21.64 21.65
RCT3	16.10	19.99	6.52	8.06	7.30	.26 .55	4.09 4.15	4.39 4.27	10.82 10.79	10.72 10.90	21.61 21.62
RCT4	16.03	20.02	6.33	8.05	7.31	.37 .40	4.15 4.04	4.33 4.47	10.75 10.92	10.72 10.97	21.67 21.69
RCT5	16.00	19.96	6.44	8.10	7.24	.55 .27	4.05 4.15	4.59 4.29	10.74 10.84	10.73 10.85	21.58 21.58

Table 2-5: Dimensions of the fabricated tensile specimens, with the measured dimensions corresponding to Figure 2.3. Note that samples T1 and T3 have misaligned gage sections; samples T4, T5, and T7 have flats that were not properly centered; and sample T5 is slightly bent, as can be seen in Figure 2.4.

Specimen ID	A	B	C	D	E	F
Nominal	1.7	33	16	2	3.5	6
Tolerance	±.05	±.15	±.05	±.05	±.05	±.05
T1	1.63	33.07	16.16	2.00	3.51	5.96
T3	1.44	33.06	16.11	1.90	3.47	6.01
T4	1.68	33.03	15.97	2.02	3.49	5.99
T5	1.66	33.06	16.08	1.99	3.49	6.00
T6	1.70	33.16	16.03	2.03	3.49	6.02
T7	1.69	33.16	16.03	2.0	3.51	6.01
T8	1.69	33.19	16.08	1.93	3.49	6.01
T9	1.71	33.18	16.4	1.93	3.50	5.99
T10	1.69	33.26	16.06	1.94	3.49	5.99
T11	1.71	33.03	16.11	1.92	3.56	5.96
T12	1.72	33.07	16.09	1.93	3.49	5.99
T13	1.71	33.05	16.07	1.93	3.45	6.01

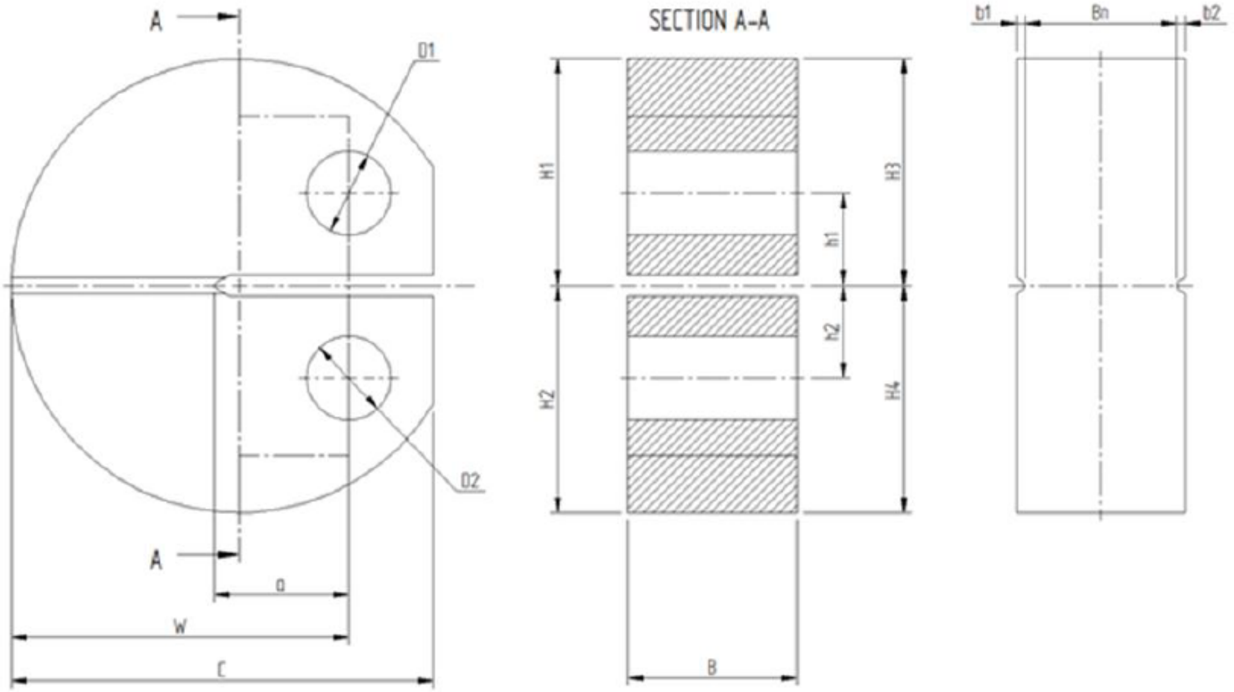

Figure 2-1: Diagram of the RCT samples manufactured for this project. The labeled dimensions were measured for each sample as seen in Table 2.3 to verify that the specimens were fabricated in accordance to the designed dimensions and tolerances.

Figure 2-2: Image of sample RCT1 from both sides. It is clearly evident that a small amount of material was removed during the fabrication of tensile sample T3; however, this should not significantly affect the stress intensity during the CGR test.

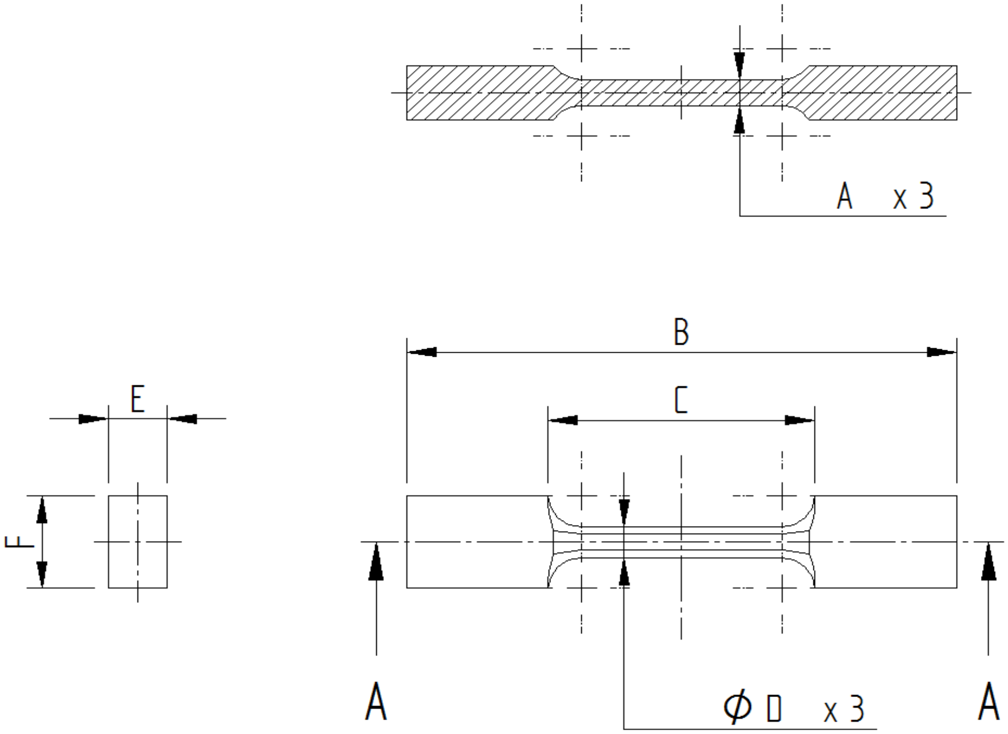

Figure 2-3: Schematic of the tensile specimens that were manufactured for this project, with the labeled dimensions that were measured for each sample as seen in Table 2.4.

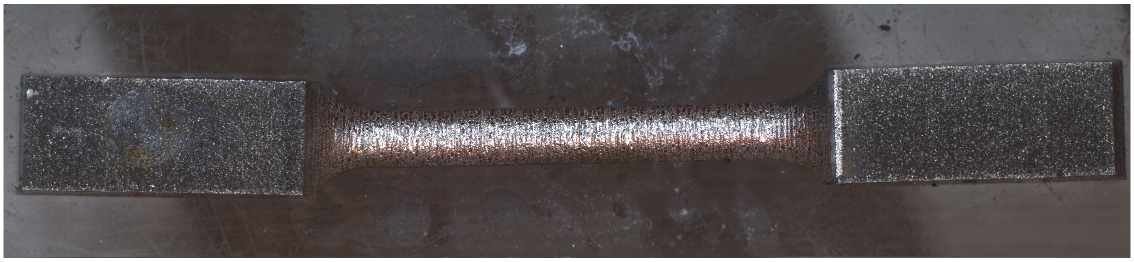

Figure 2-4: Side view of sample T5, which was likely deformed during the handling of the sample post-fabrication.

Figure 2-5: Image of the hot cell facility at ORNL, wherein the tensile specimen preparation was completed. The difficulty of the specimen cutting and polishing was exponentially increased using large manipulators and in-cell tools that were required to complete the work on the small scale (<30 mm) specimens.

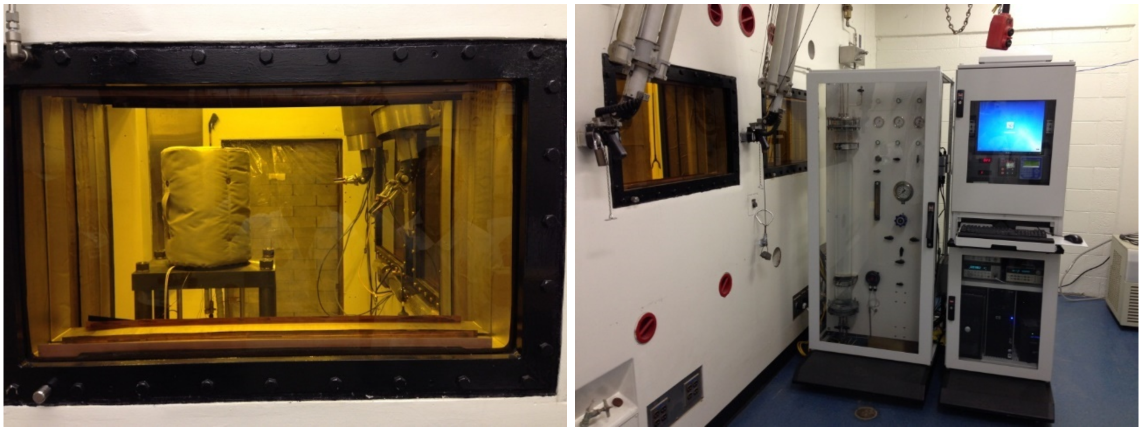

Figure 2-6: Images of CGR test system IM5 in hot cell #2.

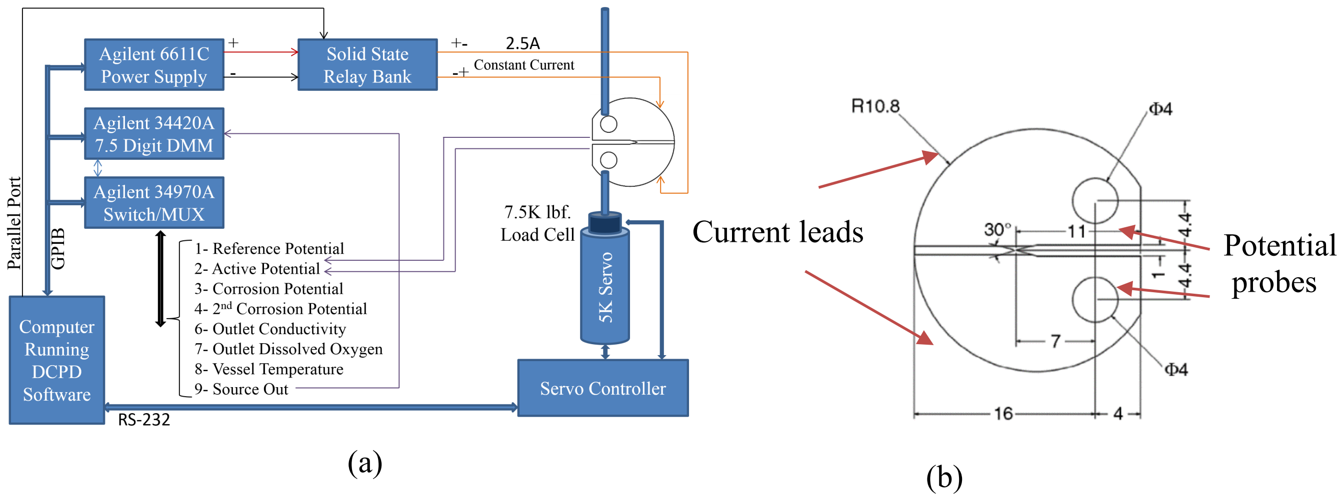

(a)

(b)

Figure 2-7: DCPD monitoring system. (a) a schematic of DCPD instrumentation and circuit diagram, and (b) arrangement of current and potential probe leads on the 0.5T RCT specimen

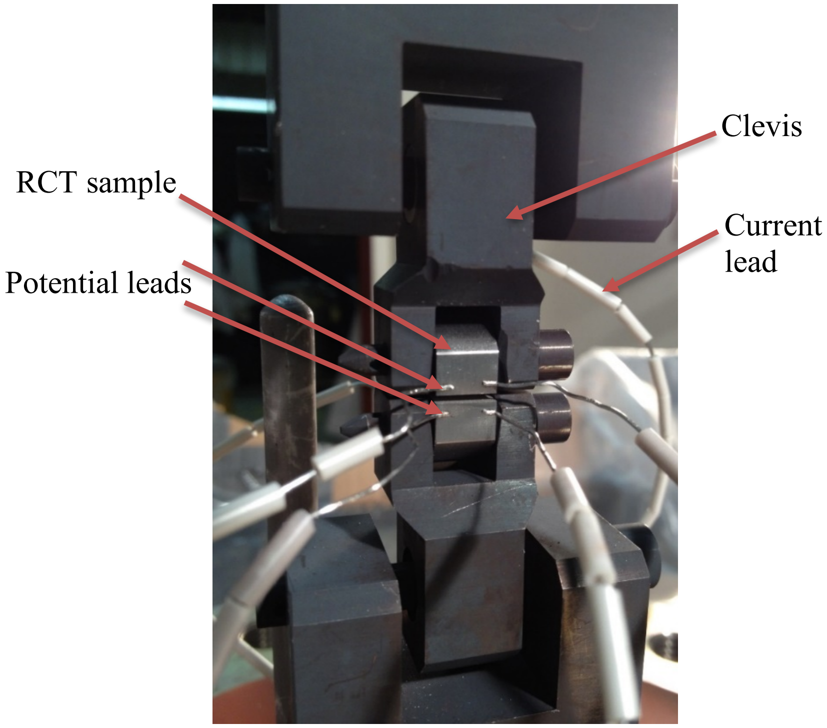

Figure 2-8: RCT sample spot welded in a hot cell.

3. Results

3.1 Irradiated Microstructure

This section presents a summary of the results of the microstructural analysis, completed on the as-irradiated condition and multiple annealing conditions. The microstructural analysis includes the effect of annealing on the Vickers micro-hardness, dislocation loop size and density, solute cluster size and density, and the grain boundary segregation.

3.1.1 Hardness

Vickers micro-hardness has been often used in literature as a simple method to evaluate the bulk changes in the irradiated microstructure following PIA treatments, as a greater reduction in hardening has been observed to correspond to a greater removal of irradiation defects such as dislocation loops and solute clusters. As such, to select the specific annealing conditions for microstructure analysis, CERT and CGR experiments, a wide range of annealing temperatures and times were applied to the as-received sample blanks listed in Table 2-3, and using the procedure outlined in section 2.1.1.

Four different temperatures: 450°C, 500°C, 550°C, and 600°C with times: 1, 5, and 20 hr at each temperature were utilized, as these time/temperature combinations were expected to fully bound the complete removal of irradiation hardening. The hardness measurements for the selected temperatures are shown in Table 3-1 and Figure 3-1, where the irradiation hardening is plotted as a percentage of the as-irradiated condition.

The irradiation hardening ($\Delta H_{v,\,Irr}$), is the increase in the hardness due to the presence of irradiation defects and is calculated from the following expression:

$$\Delta \mathrm{H}_{\mathrm{v,Irr}} = \mathrm{H}_{\mathrm{v,Irr}} - \mathrm{H}_{\mathrm{v,Unirr}} \,, \tag{3.1}$$

where $H_{v,Irr}$ is the measured hardness of the as-irradiated 304L stainless steel, and $H_{v,Unirr}$ is the measured hardness of the unirradiated 304L stainless steel. As no archive material is available, the hardness of the unirradiated materials was assumed to be that of a 304L stainless steel, which was measured as 157.95 H_v. Similarly, the post-PIA irradiation hardening ($\Delta H_{v,\,PIA}$) can be calculated via equation 3.1, where the measured hardness after PIA ($H_{v,\,PIA}$) is substituted for the as-irradiated measurement ($H_{v,\,Irr}$). The percentage of as-irradiated hardening remaining is then calculated as:

$$\%\text{ of As irradiated hardening} = \frac{\Delta \mathrm{H}_{\mathrm{v,PIA}}}{\Delta \mathrm{H}_{\mathrm{v,Irr}}} \,. \tag{3.2}$$

Overall, it was observed that annealing at 450°C, had a negligible impact on the irradiation hardening up to times of 20 hours. However, temperatures of 500°C, 550°C, and 600°C showed successively greater removal of hardening with increasing time and temperature. Following annealing at 600^{o}C: 20hr, the measured hardness had returned to a value expected for an unirradiated 304L stainless steel.

Using the criterion outlined in previous quarterly reports, annealing conditions of 500^{o}C: 1hr, 550^{o}C: 1hr, 550^{o}C: 5hr, and 550^{o}C: 20hr, were selected for both more detailed microstructural analysis and application to the CERT and CGR specimens. Following the annealing of the CERT and CGR samples, small slices from the tensile heads were used to confirm the removal of hardness. The results for these slices was outlined in previous reports, but there was a good agreement in hardening removal as compared to the data in Table 3-1.

3.1.2 Dislocation Loops

The faulted dislocation loops in the as-irradiated 304L SS and after PIA at 500°C: 1hr, 550°C:1 and 5hr were characterized using rel-rod dark field technique. TEM images of dislocation loops are shown in Figure 3-2. Dislocation loops were confirmed in all examined PIA conditions. However, annealing at 550°C: 20hr resulted in a low density of large loops (Figure). Because of the very low density of loops, rel-rods were not observed and dislocation loops were imaged bright field under a two-beam condition. In addition to loops, stacking fault tetrahedral were observed as shown in the insert of Figure .

The average dislocation loop diameter and density in 304L SS irradiated to 5.9 dpa in BWR and after various post-irradiation annealing conditions are given in

Table . The initial average dislocation loop diameter after irradiation was 8.3 nm and it was 9.6 nm after PIA at 500°C: 1hr. The average loop size was 8.9 nm and 8.0 nm after PIA at 550°C: 1hr and 5hr, respectively. The comparison of loop size at different annealing conditions is shown in Figure 1-4. The dislocation loop sizes are virtually the same after annealing at 550°C for 5h. Significant increase in dislocation loop size was observed after 550°C for 20h, in which the loop size was about 26 nm. The loop density reduced significantly from 1.1×10^{23} m^{-3} at the as-irradiated condition to 8.2×10^{22} m^{-3} after annealing at 500°C: 1hr, to 3.2×10^{22} m^{-3} at 550°C: 1hr, to 1.3×10^{22} m^{-3} at 550°C: 5hr. The number density became negligible after annealing at 550°C: 20hr compared to the number density in the as-irradiated condition. In other words, the loop density reduced to ~3/4 of its initial density after PIA at 500°C: 1hr and to ~1/10 after PIA at 550°C: 5hr. Post-irradiation annealing at 550°C for 20 hours resulted low number density of large loops.

The size distribution of dislocation loops in 304L SS irradiated to 5.9 dpa at in BWR environment and after various post-irradiation annealing conditions is shown in Figure 1b. It appears that smaller dislocation loops are preferably annealed out at the 500°C for 1hr condition and in fact, the density of large loops (>13nm) shows increase in population compared to the as-irradiated condition. However, this is not observed for annealing at 550°C condition, in which the dislocation density decreases across the whole size spectrum.

3.1.3 Solute Clusters

Condition	Density (10^{23} /m^3)	% of As-Irradiated	Diameter (nm)	Ni-Si Ratio	Volume Fraction (%)
As-Irradiated	3.88 ± 0.59	100%	9.24 ± 0.71	5.13 ± 0.13	2.47 ± 0.08
500°C: 1 hr	2.83 ± 0.46	72.8%	10.79 ± 0.90	5.12 ± 0.48	2.44 ± 0.21
550°C: 1 hr	2.35 ± 0.11	60.5%	12.34 ± 0.09	5.43 ± 0.27	2.97 ± 0.05
550°C: 5 hr	1.21 ± 0.47	31.2%	18.09 ± 4.68	7.61 ± 0.59	3.59 ± 0.91
550°C: 20 hr	0.70 ± 0.07	18.0%	20.23 ± 1.43	7.95 ± 0.03	2.96 ± 0.16

Two types of solute clusters were observed in 304L SS irradiated to 5.9 dpa in BWR; Ni-Si rich clusters and Al-Cu rich clusters. They are shown in Figure 3-5 for the as-irradiated condition. Evolution of the Ni-Si and Al-Cu clusters after PIA is shown in

Figure 3-6 and the number density, diameter, Ni-Si or Al-Cu ratio and volume fraction for Ni-Si and Al-Cu clusters are given in

Table and

Table 1, respectively.

The Ni-Si clusters are mainly precursors of the γ′ or G phase as the concentrations of Ni and Si have not reached that for phase formation (75% Ni and 25%Si). The number density in the as-irradiated condition is 3.88×10^{23} m^{-3} and decreases to 2.83×10^{23} m^{-3} after PIA at 500°C: 1hr and to 2.35×10^{23} m^{-3} after PIA at 550°C:1hr. The density further decreases to 0.7×10^{23} m^{-3} after annealing at 550°C: 20hr, which is only ~18% of the as-irradiated number density. The cluster size, however, increases from ~9 nm at the as-irradiated condition to 20 nm after annealing at 550°C: 20hr. Due to the increase in the cluster size the volume fraction does not change significantly after annealing: ~2.5% in the as-irradiated condition and ~3.0% after annealing at 550°C: 20hr.

The Al-Cu shows the same trend as Ni-Si cluster after annealing. The number density in the as-irradiated condition is 2.92×10^{23} m^{-3} and it decreases to 2.46×10^{23} m^{-3} after PIA at 500°C: 1hr and to 1.57×10^{23} m^{-3} after PIA at 550°C: 1hr. The density further decreases to 0.9×10^{23} m^{-3} after annealing at 550°C:20hr, which is ~32% of the as-irradiated number density. The cluster size, increases from ~6 nm at the as-irradiated condition to ~13 nm after annealing at 550°C: 20hr. The volume fraction of Al-Cu clusters is rather small, ~0.035% in the as-irradiated condition and ~0.016% after annealing at 550°C: 20hr.

3.1.4 Grain Boundary Segregation

Radiation-induced segregation was examined in 304L SS in the as-irradiated condition and PIA at 550°C for 5 and 20 hours. Figure and Figure are the ChemiSTEM elemental images showing segregation of Cr, Ni and Si at the grain boundary in the as-irradiated and PIA at 550°C:20h condition, respectively. Depletion of Cr, Fe and enrichment of Ni, Si and P are evident from composition profile across the grain boundary in the as-irradiated condition (Figure).

In the as-irradiated condition, the depletion of Cr is ~5.5% and enrichment of Ni and Si are 13.4% and 2.2% respectively (Table). The depletion of Cr decreases to 3.2% after annealing at 550°C:5h and 1.4% after annealing at 550°C:20h. Enrichment of Ni drops to ~3.2% after annealing at 550°C:20h, which corresponds to 23% of Ni enrichment in the as-irradiated condition. There is only 0.13% of enrichment of Si at the grain boundary after annealing at 550°C:20h, which is ~6% of Si enrichment at the as-irradiated condition.

Composition profiles for Cr, Ni, Si and P for the as-irradiated and 550°C PIA conditions are shown in Figure . Besides the recovery of the segregated elements by thermal annealing, the segregated peaks appear to broader after annealing.

3.2 CERT Experiments

This section presents a description of the incremental CERT test results obtained from the irradiated and PIA tensile bars. CERT tests were conducted at 288°C under simulated BWR-NWC conditions. The stress-strain behavior of each specimen is first presented with comments about the observed mechanical behavior. A summary of the mechanical properties is then presented followed by images of each fracture surface after completion of the CERT tests. More detailed information regarding each of the strain increments was outlined in previous quarterly reports.

3.2.1 Prediction of Yield Stress and Incremental Straining Experiments

Prior to beginning the incremental straining experiments, it was necessary to first predict the yield stress of both the as-irradiated condition and following each annealing treatment. Previous studies have shown that the change in irradiation hardening is linearly related to the change in the yield stress as seen in Equation 3.3 [19].

$$\Delta\sigma_y = X * \Delta H_v \tag{3.3}$$

Where X is the linear correlation factor; prior work by Busby *et al.* found that for irradiated austenitic stainless steels, an average correlation factor of X = 3.03, best fits the available data. However, the correlation factors for individual data sets had more variability, ranging from 2.63

to 3.83 [19]. Using the average correlation factor of 3.03 and the unirradiated hardness and yield stress of 157.95 H_v and 211.5 MPa, respectively, an initial prediction of the yield stress for our initial two specimens, T-4 (as-irradiated) and T-9 (550^{o}C: 20 hr) were calculated based on the hardness measurements taken after PIA treatments, as shown in Table 3-6. Based on these predictions straining increments to 40, 60, 80, and 100% were made for these two specimens as listed in Table 3-7. The as-irradiated specimen T-4 showed a very close agreement between the predicted and measured yield stress. However, for the T-9 specimen, the actual hardness was originally incorrectly measured, thus resulting in a miscalculated yield stress prediction. As such, an additional stress increment was required to reach the correct yield stress. After remeasuring the hardness of the T-9 specimen, it was found to be much higher than originally expected, but the new value correctly matched the measured yield stress.

Utilizing these measured yield stresses a new correlation factor was fit to our specific material, which was then used to predict the yield stresses of the T-5 (500^{o}C: 1hr),T-13 (550^{o}C: 1hr), T-7 (550^{o}C: 5hr), and T9 (550°C: 20hr) specimens. As shown in Figure 3-11, the final correlation factor for these five specimens was calculated as $X = 2.47$. While this correlation factor is lower than those previously seen in literature, the difference is likely an effect of the PIA treatments, as the previous correlation factors only examined as-irradiated microstructures [19]. Figure 3-12 shows a near prefect 1-to-1 comparison between the final predicted and measured yield stresses utilizing this fitted correlation factor.

Table 3-7 shows a complete list of the incremental straining experiments that were applied to each of the examined specimens, including the target stress/strain for each increment as well as the final value. Overall, there was a good agreement between the target and achieved stress/strain, excluding the yield stress for specimen T-9 specimen and the 0.5% ε_p increment for the as-irradiated T-4 specimen. The T-7 increment to 10% ε_p was purposely halted early for examination due to the occurrence of significant necking.

3.2.2 Stress-Strain Behavior

Stress-strain curves for each of the tested conditions: as-irradiated, 500^{o}C: 1 hr, 550^{o}C: 1 hr, 550^{o}C: 5 hr, and 550^{o}C: 20 hr are shown in Figure 3-13. The elastic deformation portion of each curve has been corrected to subtract system compliance by normalizing to the expected Young's modulus for an austenitic stainless steel.

The as-irradiated condition displayed a yield stress drop and subsequent strain softening. as typical of the irradiated condition of a solution-annealed stainless steel. Annealing at 500^{o}C:1 hr slightly reduced the yield stress, while completely removing the yield stress drop and strain softening behavior, instead displaying an extremely slight strain hardening behavior. Annealing at 550^{o}C: 1 and 5hr, further reduced the yield stress and resulted in a slight strain hardening behavior, with higher elongations and onset of necking at ~7% plastic strain. Annealing at 550^{o}C:20 hr caused a further drop in the yield stress and an increase in the elongation. Furthermore, this condition displayed a clear strain hardening behavior, up to about 8.5% plastic strain.

3.2.2 Mechanical Properties

Mechanical properties of the varying annealing treatments, as determined from the CERT tests, are summarized in Table 3-8. The table is organized by annealing condition, showing the yield stress, maximum stress, uniform and total elongation. For the as-irradiated condition, uniform elongation and maximum stress both occurred at the yield point (~0.5%) because of strain softening.

Overall, it was observed that the yield stress was reduced in proportion to the residual hardening following the annealing treatments. Furthermore, it was seen that the annealing treatments also lead to a change in the mechanical behavior, from a strain softening to strain hardening, and an increase in the ductility of the specimen.

3.2.3 Fractography

Following CERT testing, the fracture and gage surfaces were fully examined by SEM. Areas of IG or TG cracking were quantified to determine %IG, %TG, %mixed IG/TG, and %ductile failure. Examples of each type of fracture can be seen in Figure 3-14. Reduction in area was also determined based on the full area of the fracture surface. Each sample fracture surface is shown in Figure 3-15.

The results of the fractography classification and reduction of area analysis after CERT are summarized in Table 3-9 and Figure 3-16. The %IG varied between 48.4% and 0%, and was observed to largely decrease in response to increasing annealing time and temperature. However, while the IASCC susceptibility was fully removed for the 550^{o}C: 1 and 5 hr annealed specimens, as evidenced by the fully ductile fracture surfaces, the 550^{o}C: 20 hr specimen still displayed some residual IASCC susceptibility. Reduction of area followed a similar trend as total elongation in that it increased with increasing annealing, however, specimen T-5 (PIA 500^{o}C) showed a much higher reduction in area as compared to T-4 (as-irradiated), despite an only slightly higher final elongation.

3.2.4 Dislocation Channeling

As previously mentioned, the degree of localized deformation was measured via SEM following each stress/strain increment. However, due the highly strained region that occurs during the advancement of a crack tip, measurements of the dislocation channel density were only taken for increments which displayed no significant crack growth. Furthermore, the as-irradiated material displayed an unexpected resistance to localized deformation as significant populations of dislocation channels were only observed post-yield, following the addition of bulk plastic strain. Previous literature studies for irradiated material have observed significant localized deformation below the specimen yield stress [20]–[22].

The measured dislocation channel densities, grain boundary interaction site densities, and ratio of discontinuous to continuous interaction sites for each strain increment are shown in Table 3-10. As multiple specimens exhibited regions of enhanced strain, where the eventual crack initiation later occurred, the measured channel densities are averaged over this region (~1mm of gage length) where later crack initiation was observed, rather than over the entire gage length. Comparison of the dislocation channel density with strain for the examined conditions: as-irradiated, 500^{o}C: 1hr, 550^{o}C: 1, 5, and 20hr, is shown in Figure 3-17. The density of dislocation channel-grain boundary interaction sites is given in Figure 3-18, while the ratio of discontinuous to continuous interaction sites is presented in Figure 3-19.

It is observed that the as-irradiated, PIA: 500^{o}C: 1hr, and PIA: 550^{o}C: 1 hr conditions have very similar dislocation channel densities, while the 550^{o}C: 5 hr sample exhibited a decrease in the density. The 550^{o}C: 20hr had a significantly reduced density regardless of the plastic strain. The interaction site density seems to change in proportion to the total dislocation channel density regardless of the annealing condition.

3.3 CGR Experiments

This section presents a summary of the CGR test results obtained from the RCT 3 (PIA 550^{o}C: 20hr), including crack propagation in both 288°C BWR-NWC and 288°C BWR-HWC. Due to delays in the project, only the PIA 550^{o}C: 20hr was tested.

3.3.1 Testing Steps and CGRs

RCT-3 was selected for the first test on neutron-irradiated samples. The main purpose of the CGR test is to determine the *K* dependence of the CGR rate and the effect of environment change on CGR. The post-irradiation heat treatment of sample RCT-3 was expected to have removed much of the damage due to irradiation in reactor. To compare the SCC susceptibility between different samples, it is preferable to test them at the same *K* levels. Meanwhile, the applied *K* values should meet the validity criterion. Based on the *K* validity check of the as-irradiated sample and RCT3, three *K* values were selected: 18, 14, 11 MPa•m$^{1/2}$.

Figure 3-20 shows the *a/W* and corrosion potential of RCT-3 during the pre-cracking stage. The pre-cracking steps were started when the corrosion potential of sample stabilized. $K_{\max}$ was set to 18 MPa•m$^{1/2}$. The CGR decreased as *R* was increased from 0.4 to 0.6. It decreased further as the frequency was decreased. The CGRs have been corrected after the fracture surface was analyzed.

To study the effect of hydrogen addition, the environment was switched from NWC to HWC as the CGR stabilized at 5.9×10^{-7} mm/s. K was kept at 18 MPa•m$^{1/2}$. As shown in Figure 3-21, the CGR dropped significantly to 1.5×10^{-8} mm/s after the switch. Then the environment was switched back to NWC, requiring ~650 hr before the CGR stabilized at a value of 6.6×10^{-7} mm/s, which was very consistent with the previous value in NWC. There are some jumps in a/W (up to 0.002) which may be due to the break of ligaments on the crack propagation path.

To study the CGR dependence on K, the K value was first dropped from 18 to 14 MPa•m$^{1/2}$. As shown in Figure 3-22, there is a large jump in a/W (~0.033) after the K was held at 14 MPa•m$^{1/2}$. It is very unusual to see such a large jump. This jump was confirmed to due to the break of ligament on the fracture surface which is shown in Figure 3-24. The CGR at 14 MPa•m$^{1/2}$ finally stabilized at 2.9×10^{-7} mm/s. Then K was further dropped to 11 MPa•m$^{1/2}$. Unexpectedly, two large jumps in a/W (over 0.14) occurred. The final a/W was around 0.92 when the test was stopped.

3.3.2 Fractography and IGSCC

The sample was opened and the fracture surface was analyzed with SEM. Figure 3-23 shows the fracture surface from the side views. The images show that the crack is in plane and follows the side grooves well.

Figure 3-23 shows the plane view image of fracture surface. The fracture surface is intergranular excepting the pre-cracking and the post-test fracture region, which are due to cyclic loading and mechanical overloading at room temperature respectively. The large crack on the left side was due to the post-test loading procedure. It should be noted that there is a boundary between the upper part and the lower part in the IGSCC region. The enlarged images from the starting and ending parts of the boundary show that the two parts of IGSCC region are not on the same plane and the interface between them is transgranular and almost perpendicular to the fracture surface. Such interface would not crack open until the opening of the main crack is larger than the distance between the two crack propagating planes. So, the main crack front should be beyond the crack front at the interface. The could explain why DCPD underestimated the crack length. The jumps in a/W were probably was caused by the sudden opening of the interface.

3.3.3 DCPD Estimation and Actual CGR

The crack lengths measured by DCPD and SEM are listed in Table 3-11. The post-cracking correction factor is the ratio between the real length (by SEM) and the length measured by DCPD. For the pre-crack region, the length measured by DCPD is close to the real length. However, DCPD under estimated the crack length significantly for the IGSCC region. Therefore, the CGRs measured by DCPD were adjusted with the post-cracking correction factors listed in Table 3-11. Meanwhile, the *K* values were also recalculated with the applied load and the corrected crack length. The *K* validity was checked using the corrected *K* values and the yield strength of this sample which is estimated to be 415 MPa. The results are listed in Table 3-12.

Table 3-1: Change in the as-irradiated hardness due to specific annealing treatments. Overall the hardness was seen to decrease with increasing temperature and time. The irradiation hardening was determined using a value of H_v = 157.95 for the hardness of 304L stainless steel.

Sample Blank ID	PIA treatment	As-Irradiated Hardness (H_v)	PIA Hardness (H_v)	Irradiation Hardening (H_v)	Post-PIA Irradiation Hardening (H_v)	% of As-Irradiated Hardening
17	600C: 1hr	371.67	228.95	213.71	71.00	33.22
17A	600C: 5hr	371.67	185.38	213.71	27.43	12.83
9	450C: 5hr	341.50	310.42	183.55	152.48	83.07
9A	450C: 1hr	341.50	329.09	183.55	171.14	93.24
18	500C: 1hr	334.75	321.00	176.80	163.05	92.22
18A	500C: 5hr	334.75	304.81	176.80	146.86	83.07
16	500C: 20hr	350.33	286.61	192.38	128.67	66.88
16A	600C: 5hr	350.33	184.61	192.38	26.67	13.86
11	550C: 1hr	341.67	287.28	183.71	129.33	70.40
11A	600C: 20hr	341.67	150.42	183.71	-7.52	-4.10
5	500C: 1hr	339.75	308.05	181.80	150.10	82.56
5A	450C: 20hr	339.75	309.81	181.80	151.86	83.53
15	550C: 5hr	337.42	248.28	179.46	90.33	50.33
15A	550C: 20hr	337.42	220.19	179.46	62.24	34.68

Table 3-2: Dislocation loop size, number density in 304L SS irradiated to 5.9 dpa in BWR and after various post-irradiation annealing conditions.

Condition	Density (m^{-3})	% of As-Irradiated Density	Average Diameter (nm)
As-Irradiated	11.1×10^{22}	100%	8.3
500°C: 1 hr	8.21×10^{22}	74.0%	9.6
550°C: 1 hr	3.25×10^{22}	29.3%	8.9
550°C: 5 hr	1.27×10^{22}	11.4%	8.0
550°C: 20 hr	0.05×10^{22}	0.4%	26

Table 3-3. Ni-Si cluster size, density and volume fraction in 304L SS irradiated to 5.9 dpa in BWR and after various post-irradiation annealing conditions.

Condition	Density (10^{23} /m^3)	% of As-Irradiated	Diameter (nm)	Ni-Si Ratio	Volume Fraction (%)
As-Irradiated	3.88 ± 0.59	100%	9.24 ± 0.71	5.13 ± 0.13	2.47 ± 0.08
500°C: 1 hr	2.83 ± 0.46	72.8%	10.79 ± 0.90	5.12 ± 0.48	2.44 ± 0.21
550°C: 1 hr	2.35 ± 0.11	60.5%	12.34 ± 0.09	5.43 ± 0.27	2.97 ± 0.05
550°C: 5 hr	1.21 ± 0.47	31.2%	18.09 ± 4.68	7.61 ± 0.59	3.59 ± 0.91
550°C: 20 hr	0.70 ± 0.07	18.0%	20.23 ± 1.43	7.95 ± 0.03	2.96 ± 0.16

Table 1-4: Al-Cu cluster size, density and volume fraction in 304L SS irradiated to 5.9 dpa in BWR and after various post-irradiation annealing conditions.

Condition	Density (10^{23} /m^3)	% of As-irradiated	Diameter (nm)	Al-Cu Ratio	Volume Fraction of Al (%)
As-Irradiated	2.92 ± 0.20	100%	5.68 ± 0.56	2.13 ± 0.60	0.035 ± 0.006
500°C: 1 hr	2.46 ± 0.10	84.4%	6.19 ± 0.36	2.20 ± 0.06	0.027 ± 0.003
550°C: 1 hr	1.57 ± 0.11	53.8%	9.54 ± 0.66	1.19 ± 0.05	0.021 ± 0.002
550°C: 5 hr	2.61 ± 0.47	89.4%	11.00 ± 0.63	1.14 ± 0.08	0.041 ± 0.006
550°C: 20 hr	0.93 ± 0.26	31.8%	13.15 ± 1.16	0.69 ± 0.02	0.016 ± 0.001

Table 3-5. Grain boundary concentrations in the as-irradiated condition and after PIA at 550°C for 5 and 20 hours.

	GB Cr (wt%)	ΔCr (wt%)	% of As-Irr ΔCr	GB Ni (wt%)	ΔNi (wt%)	% of As-Irr ΔNi	GB Si (wt%)	ΔSi (wt%)	% of As-Irr ΔSi
As-Irradiated	12.83	-5.52	100	23.98	13.41	100	2.48	2.18	100
550°C:5h	15.11	-3.24	59	14.7	4.13	31	0.65	0.35	16
550°C:20h	16.92	-1.43	26	13.72	3.15	23	0.43	0.13	6

Table 3-6: Prediction of the yield stress following PIA based on change in hardness.

Specimen	Measured Hardness (H$_v$)	Predicted Yield Stress (MPa)	Measured Yield Stress (MPa)
T-4 (As-Irradiated)	348.0 ± 9.6	681.3 ± 23.8	685.5
T-5 (500°C: 1 hr)	326.9 ± 9.5	629.1 ± 23.5	633.4
T-13 (550°C: 1 hr)	298.5 ± 13.9	558.9 ± 34.4	553.2
T-7 (550°C: 5 hr)	266.7 ± 10.2	480.2 ± 25.2	483.6
T-9 (550°C: 20 hr)	247.9 ± 14.2	433.7 ± 35.1	421.3

Table 3-7: List of the tensile straining increments that were applied to the four tensile specimens tested for this project, including the maximum stress and plastic strain following each increment.

Specimen	Target value of stress or strain	Maximum Stress (MPa)	Fraction of Yield Stress (%)	Total Plastic Strain (%)
T-4 (As-Irradiated)	40% σ_y	270.6	39.5	0.00
	60% σ_y	401.5	58.6	0.00
	80% σ_y	539.5	78.7	0.00
	100% σ_y	685.5	100.0	0.13
	0.5% ε_p	682.8	99.6	0.74
	1.5% ε_p	657.2	95.9	1.51
	ε_f	328.5	47.9	2.00
T-5 (500°C: 1 hr)	80% σ_y	497.7	78.6	0.00
	100% σ_y	633.4	100.0	0.12
	1.0% ε_p	642.4	101.4	1.10
	1.5% ε_p	636.7	100.5	1.63
	2.0% ε_p	607.8	96.0	2.11
	ε_f	471.0	74.4	2.58
T-13 (550°C: 1 hr)	80% σ_y	446.0	80.6	0.00
	100% σ_y	553.2	100.0	0.08
	1.0% ε_p	555.1	100.3	1.07
	2.0% ε_p	558.6	101.0	2.05
	3.0% ε_p	564.0	102.0	3.11
	4.0% ε_p	565.8	102.3	4.07
	5.0% ε_p	571.1	103.2	5.10
	7.0% ε_p	569.2	102.9	7.19
	9.0% ε_p	557.7	100.8	9.35
	ε_f	515.8	93.2	11.61
T-7 (550°C: 5 hr)	80% σ_y	377.4	78.0	0.00
	100% σ_y	483.7	100.0	0.13
	2.0% ε_p	502.0	103.8	2.06
	4.0% ε_p	510.5	105.6	4.04
	6.0% ε_p	512.0	105.9	6.08
	10.0% ε_p	512.6	106.0	9.47
	ε_f	470.1	97.2	12.12
T-9 (550°C: 20 hr)	40% σ_y	130.8	31.0	0.00
	60% σ_y	196.2	46.6	0.00
	80% σ_y	261.6	62.1	0.00
	100% σ_y	341.1	81.0	0.00
	100% σ_y	415.6	98.6	0.08
	1.0% ε_p	437.7	103.9	1.06
	2.0% ε_p	454.4	107.9	2.02
	3.0% ε_p	463.6	110.0	3.00
	5.0% ε_p	478.6	113.6	5.00
	ε_f	491.5	116.7	11.43

Table 3-8: Change in the mechanical properties due to specific annealing treatments: 500°C: 1hr and 550°C: 20 hr.

Specimen	Yield Stress (MPa)	Maximum Stress (MPa)	Uniform Elongation (%)	Total Elongation (%)	Reduction in Area (%)
T-4 (As-Irradiated)	685.5	685.5	0.00	2.00	28.6
T-5 (500°C: 1 hr)	633.4	642.4	0.95	2.58	46.8
T-13 (550°C: 1 hr)	553.2	559.2	6.52	11.61	83.8
T-7 (550°C: 5 hr)	483.6	512.6	6.27	12.12	84.0
T-9 (550°C: 20 hr)	421.3	491.5	8.71	11.43	73.0

Table 3-9: Change in the relative areas of fracture mode for the as-irradiated and PIA treatments: 500°C: 1hr and 550°C: 20 hr.

Specimen	%IG fracture	%Mixed fracture	%TG fracture	%Ductile fracture
T-4 (As-Irradiated)	48.40	28.62	3.62	19.41
T-5 (500°C: 1 hr)	34.86	12.82	36.58	15.74
T-13 (550°C: 1 hr)	0.00	0.00	0.00	100.00
T-7 (550°C: 5 hr)	0.00	0.00	0.00	100.00
T-9 (550°C: 20 hr)	20.60	25.04	35.28	19.08

Table 3-10: Change in the dislocation channel and interaction site densities in the failure region. Also compared is the percentage of discontinuous sites. A plastic strain of 0.00 corresponds to the density observed at the yield stress.

Specimen	Plastic Strain (%)	Channel Density (#/mm^2)	Continuous Site Density (#/mm^2)	Discontinuous Site Density (#/mm^2)	Discontinuous/ Continuous site ratio
T-4 (As-Irradiated)	0.00	121 ± 19	21.2 ± 7.3	139 ± 22	6.5
	0.74	1337 ± 169	332 ± 67	1747 ± 229	5.3
T-5 (500^{o}C: 1 hr)	0.00	3.5 ± 2.9	0.0 ± 0.0	6.9 ± 5.8	-
	1.00	1903 ± 246	239 ± 99	3019 ± 424	12.7
	1.50	2462 ± 232	307 ± 78	3454 ± 553	11.2
	2.00	2718 ± 297	325± 116	4239 ± 553	13.1
T-13 (550^{o}C: 1 hr)	0.00	180 ± 48	42 ± 18	230 ± 66	5.5
	1.00	2448 ± 228	398 ± 68	3540 ± 520	8.9
	2.00	2602 ± 153	451 ± 51	3618 ± 225	8.0
	3.00	2737 ± 274	417 ± 48	4010 ± 446	9.6
	4.00	2869 ± 206	427 ± 95	4201 ± 306	9.8
	5.00	2856 ± 192	405 ± 65	4105 ± 296	10.1
	7.00*	5099 ± 344	765 ± 115	7365 ± 498	9.6
T-7 (550^{o}C: 5 hr)	0.00	99 ± 38	14 ± 12	151 ± 58	10.9
	2.00	2137 ± 220	262 ± 69	3289 ± 332	12.6
	4.00	2617 ± 376	405 ± 132	3891 ± 579	9.6
	6.00*	3657 ± 494	438 ± 79	5588 ± 736	12.8
T-9 (550^{o}C: 20 hr)	0.00	8.8 ± 5.5	0.0 ± 0.0	16 ± 10	-
	1.00	132 ± 46	21 ± 13	190 ± 61	9.1
	2.00	174 ± 76	44 ± 38	260 ± 81	5.9
	3.00	499 ± 115	100 ± 49	694 ± 132	6.9
	5.00	585 ± 136	107 ± 56	835 ± 156	7.8

*Specimens T-7 and T-13 were observed to begin to neck at ~6% ε_p, thus the sharp increase in dislocation channel density is believed to be a direct result of the necking, and does not accurately represent the changing localized deformation with strain.

Table 3-11: Results of crack length measurements and correction factor.

	Pre-Crack	IGSCC
Length by DCPD (mm)	0.725	2.157
Length by SEM (mm)	0.856	6.018
Correction factor	1.18	2.79

Sample	Environment	Corrected *K* (MPa.m$^{1/2}$)	Corrected CGR (mm/s)	*K* validity, %		
				E399	ΔYS/2	ΔYS/3
RCT-3 (PIA:550°C:20 hr)	NWC	18.9~19.5	5.9×10^{-7}	84	119	138
	HWC	19.5~19.6	1.5×10^{-8}	85	121	141
	NWC	19.7~31.3	6.6×10^{-7}	118	168	196
	NWC	25.9~28.1	2.9×10^{-7}	153	218	254
	NWC	24.2~25.3	5.5×10^{-7}	149	212	246

Table 3-12: Corrected *K* and CGR of RCT-3.

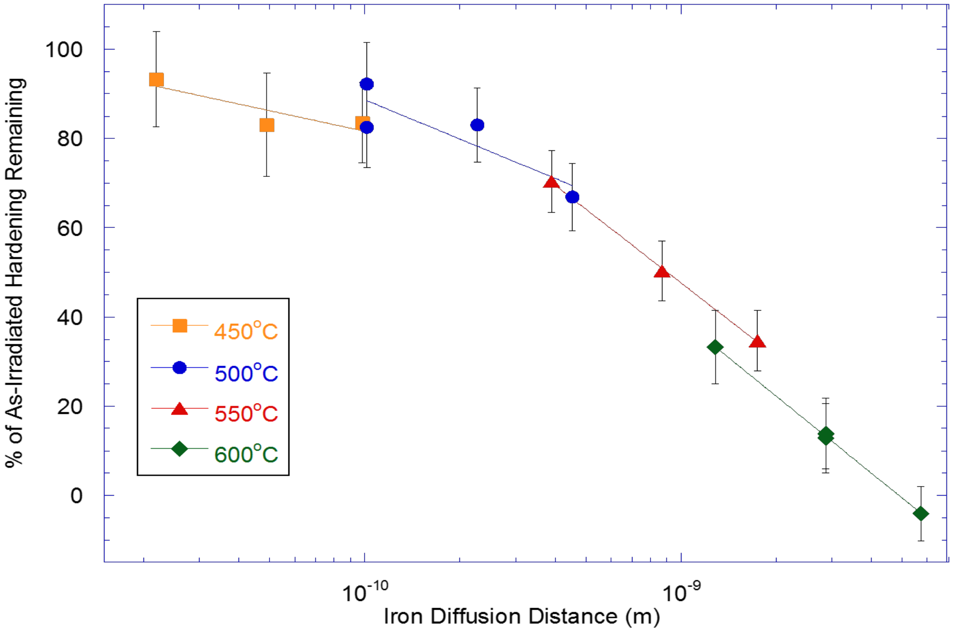

Figure 3-1: Change in the residual irradiation hardening due to specific annealing treatments.

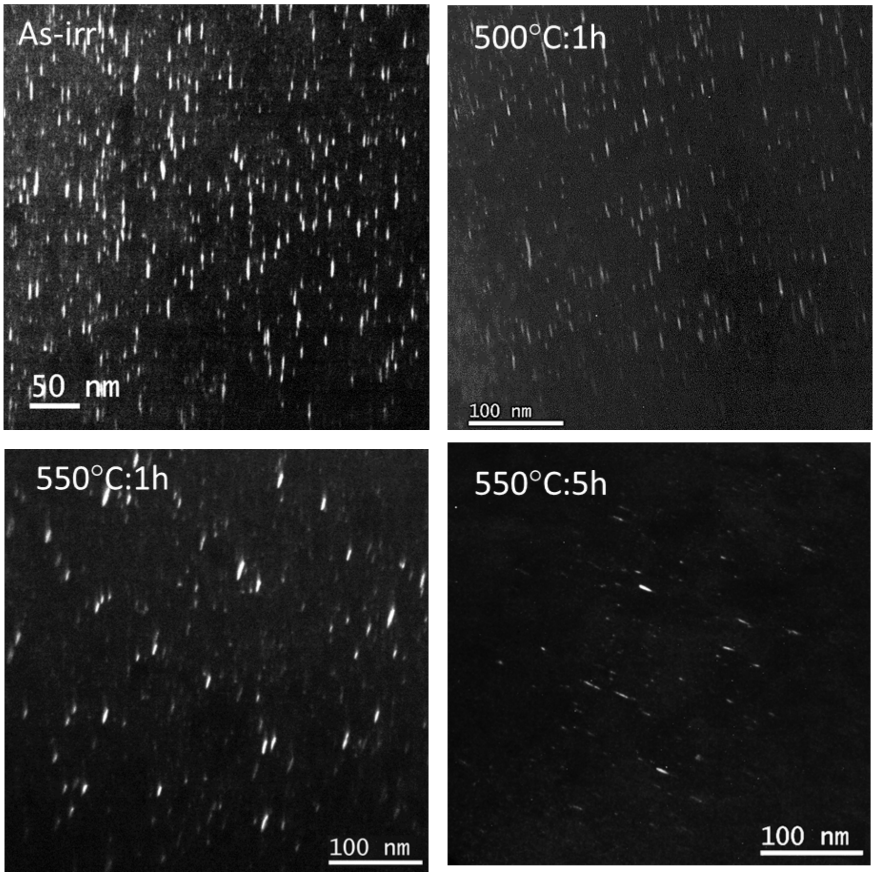

Figure 3-2. Rel-rod dark field TEM image showing the faulted dislocation loops in 304L SS irradiated to 5.9 dpa in BWR after various post-irradiation annealing conditions.

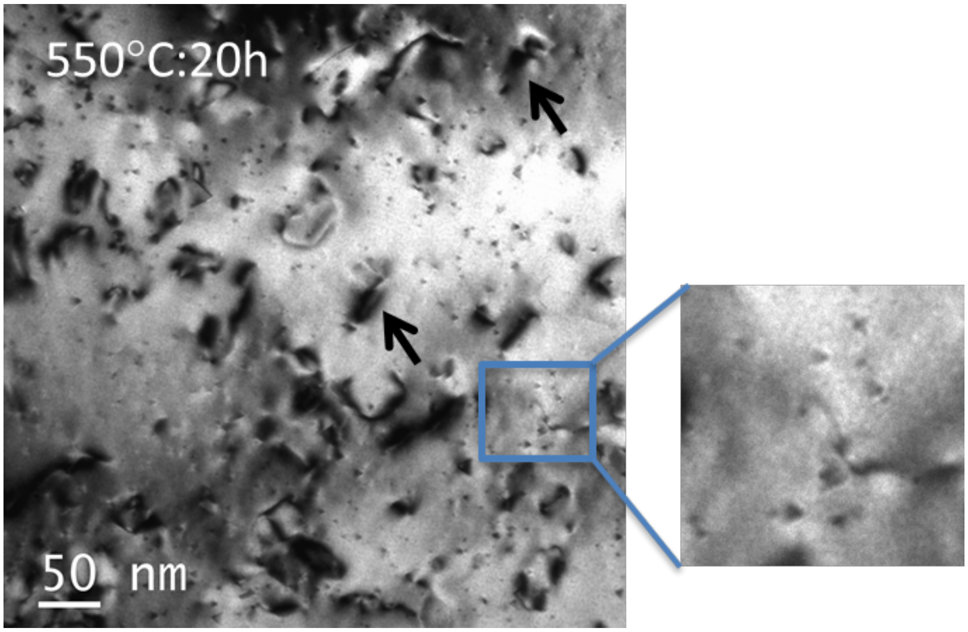

Figure 3-3. Dislocation loops (as indicated by arrows) and small stacking fault tetrahedral (as shown in the insert) in 304L SS after post-irradiation annealing at 550°C for 20 hours.

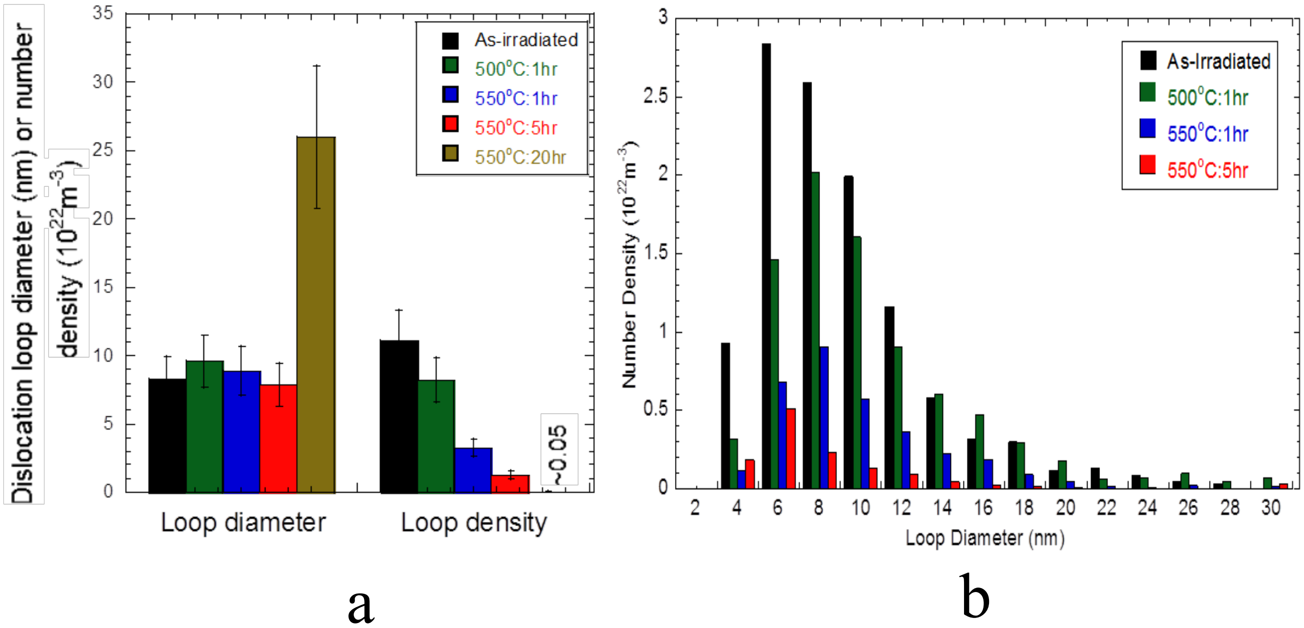

Figure 1-4. Comparison of (a) size and number density, and (b) size distribution of faulted dislocation loops in 304L SS irradiated to 5.9 dpa in BWR and after various post-irradiation annealing conditions.

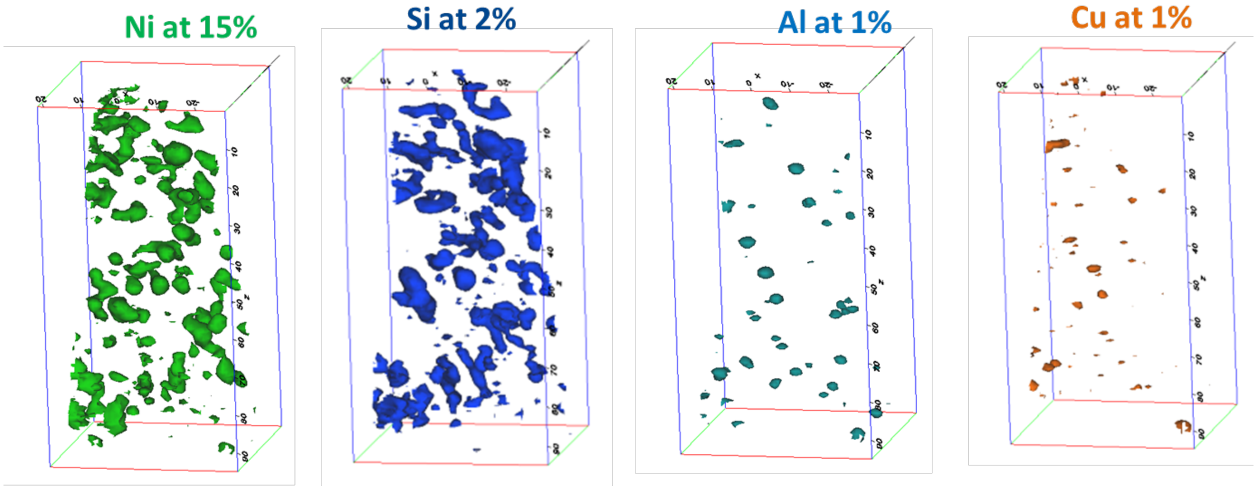

Figure 3-5. Ni-Si and Al-Cu clusters as observed in 304L SS irradiated to 5.9 dpa in BWR. Clusters are shown using isoconcentration surface plots from APT atom maps.

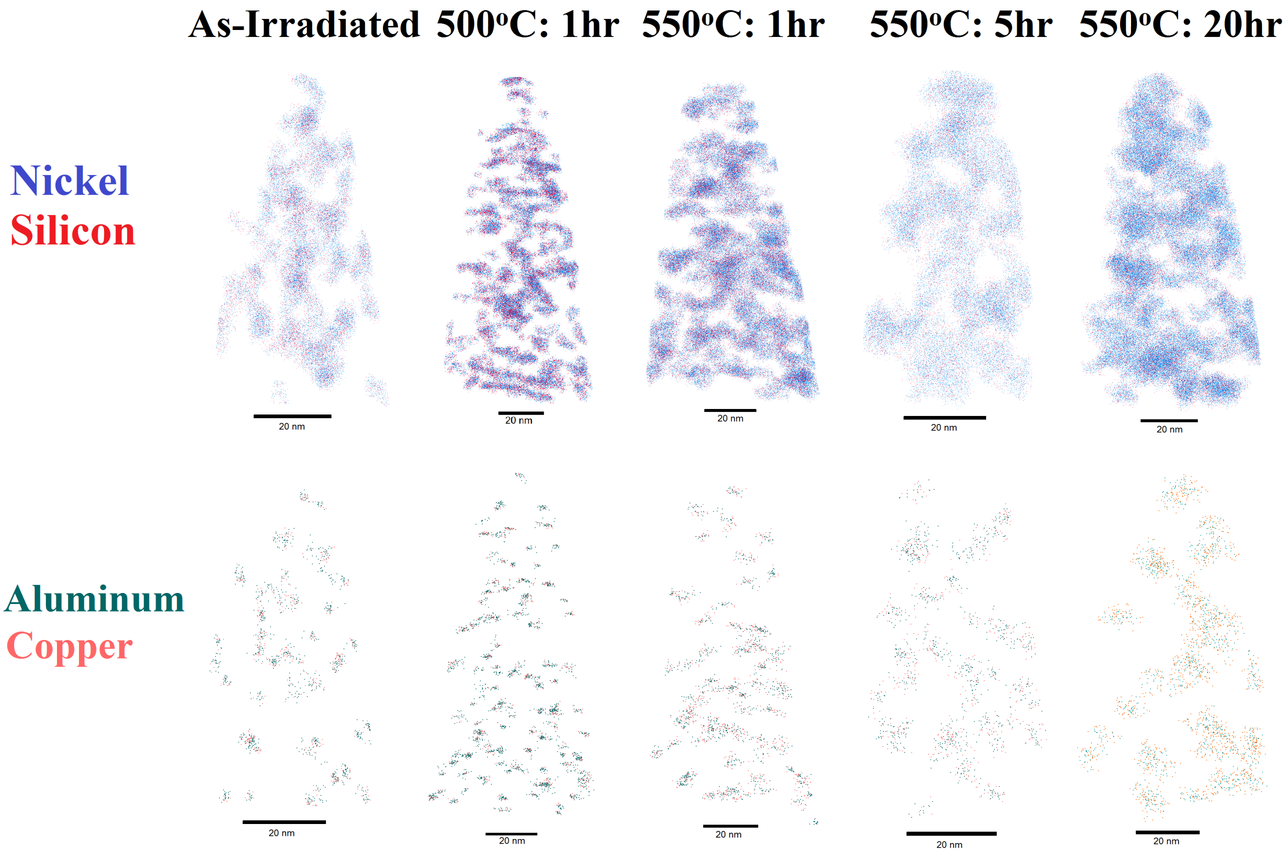

Figure 3-6. Evolution of Ni-Si and Al-Cu clusters in 304L SS irradiated to 5.9 dpa in BWR after various post-irradiation annealing conditions.

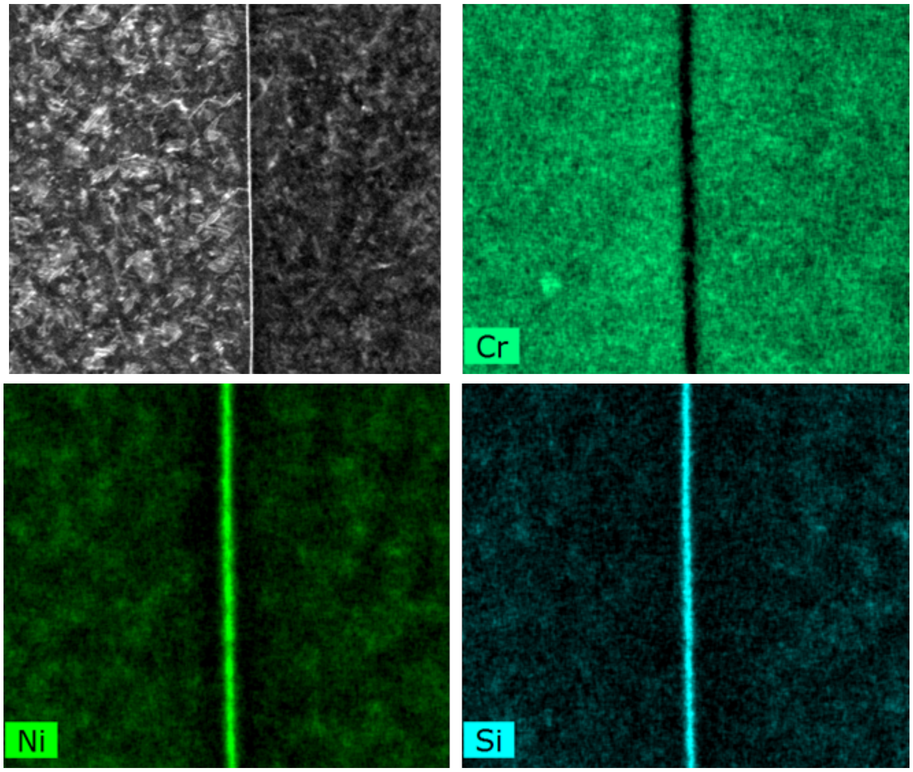

Figure 3-7. Radiation-induced segregation in 304L SS irradiated to 5.9 dpa in BWR as revealed by ChemiSTEM image. Depletion of Cr and enrichment of Ni and Si are evident.

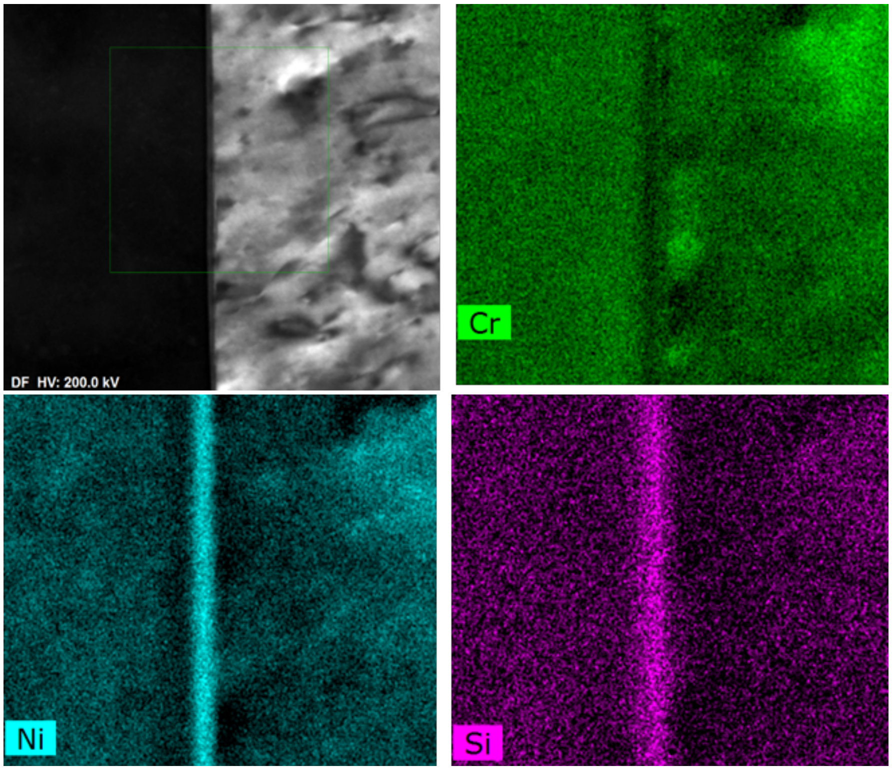

Figure 3-8. Radiation-induced segregation in 304L SS irradiated to 5.9 dpa in BWR and post-irradiation annealing at 550°C for 20 hr as revealed by ChemiSTEM image. Depletion of Cr and enrichment of Ni and Si are still evident.

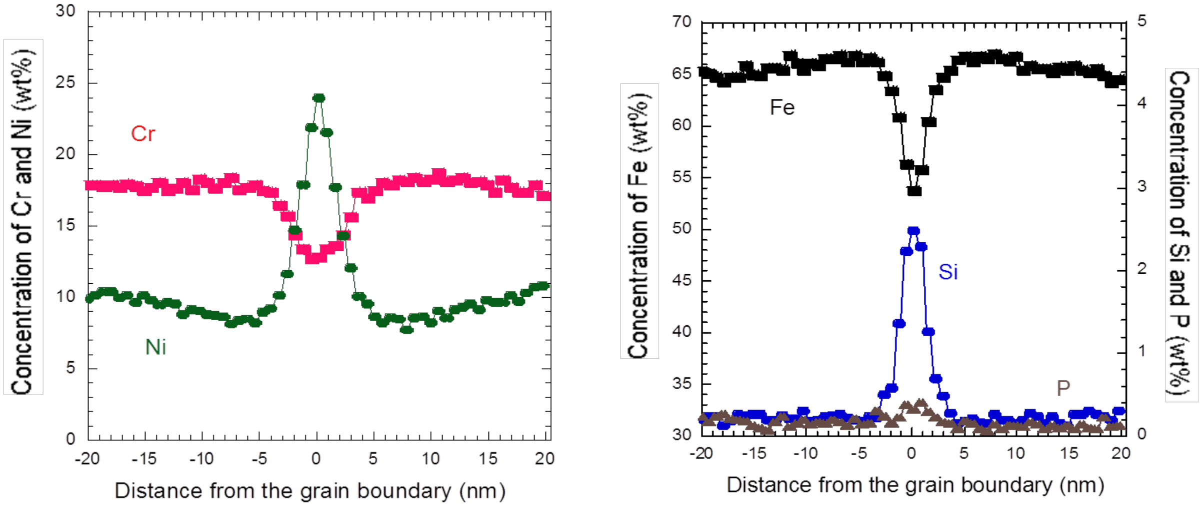

a b

Figure 3-9. Composition profile across the grain boundary in 304L SS irradiated to 5.9 dpa in BWR for (a) Ni and Cr, and (b) Fe, Si and P.

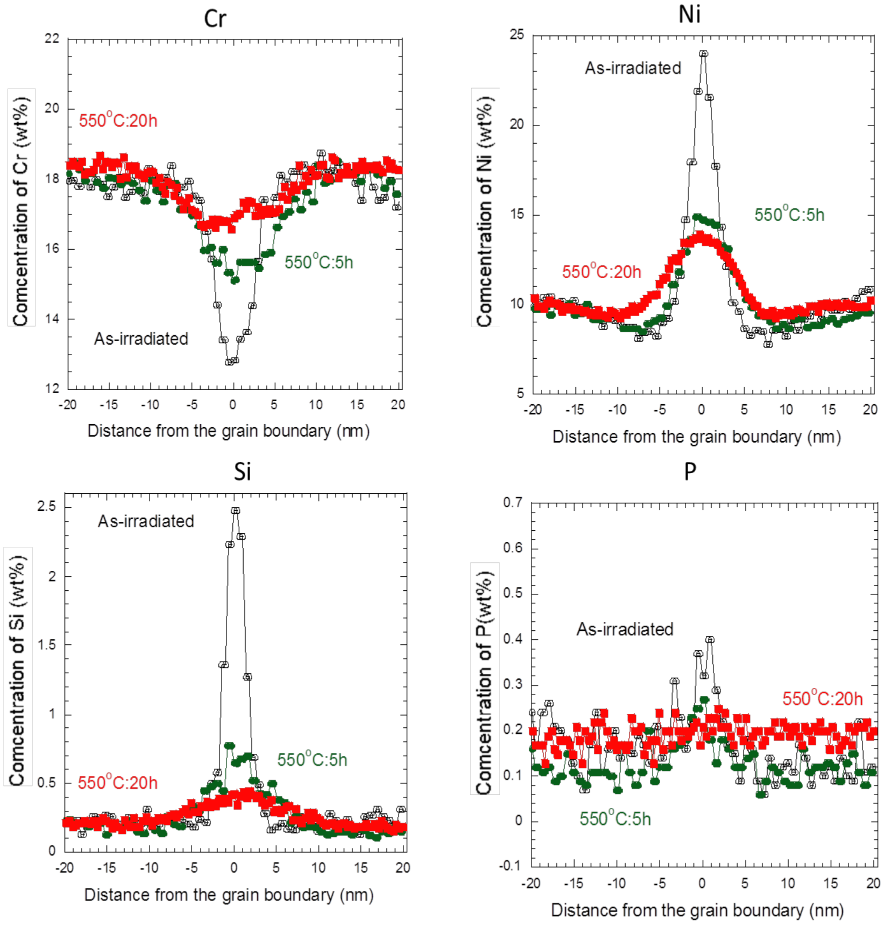

Figure 3-10. Effect of post-irradiation annealing on the segregation profiles of Cr, Ni Si and P in 304L SS irradiated to 5.9 dpa in BWR.

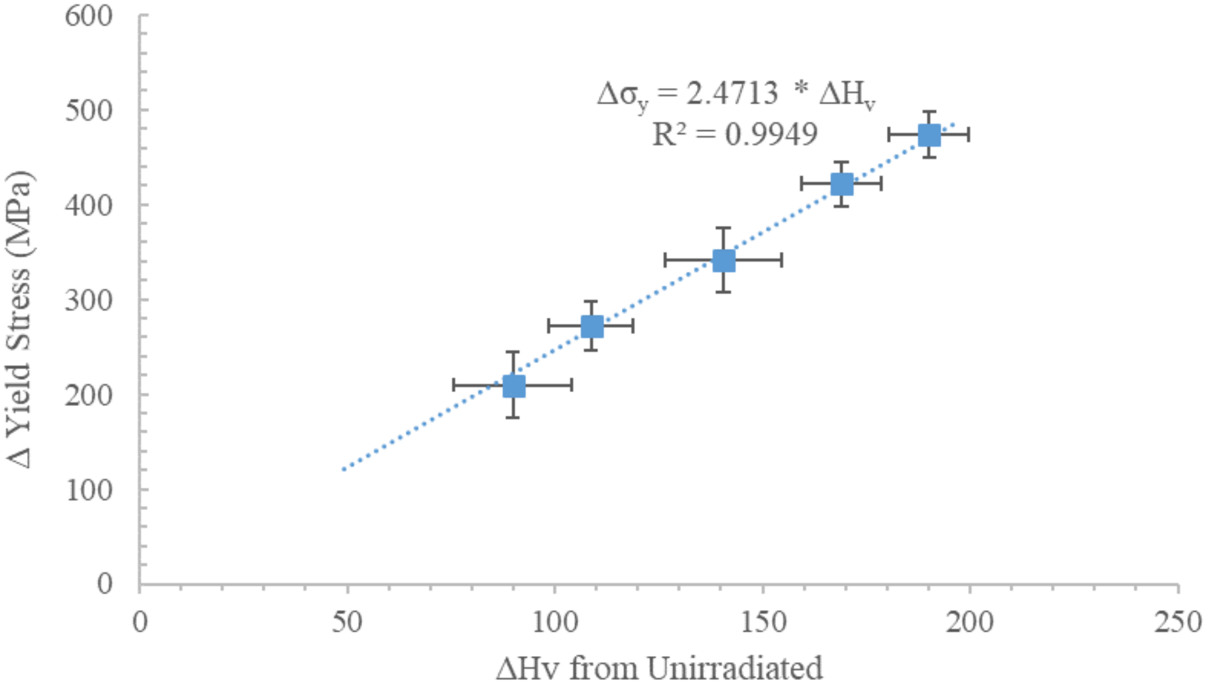

Figure 3-11: Comparison between the measured change in yield stress and the change in hardness from the base unirradiated condition ($\sigma_y = 211.5$ MPa, $H_v = 157.95$) used to predict the yield stress.

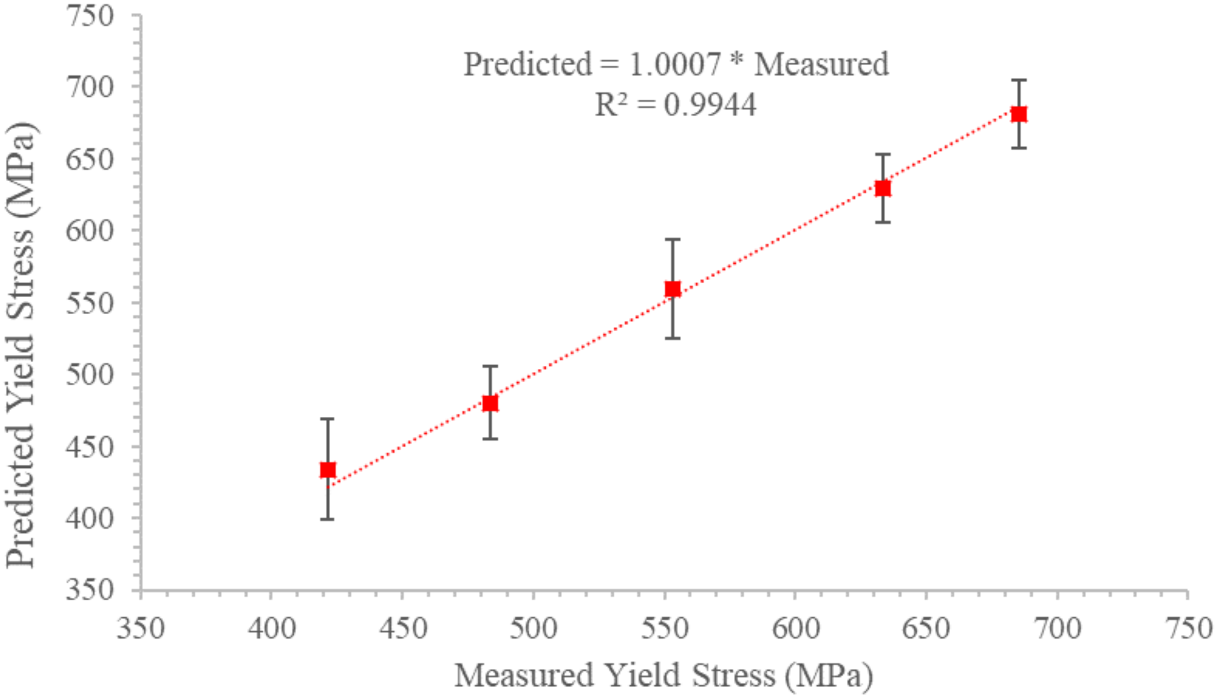

Figure 3-12: Comparison between the predicted yield stress values using a correlation factor of 2.47 and the measured values experimentally.

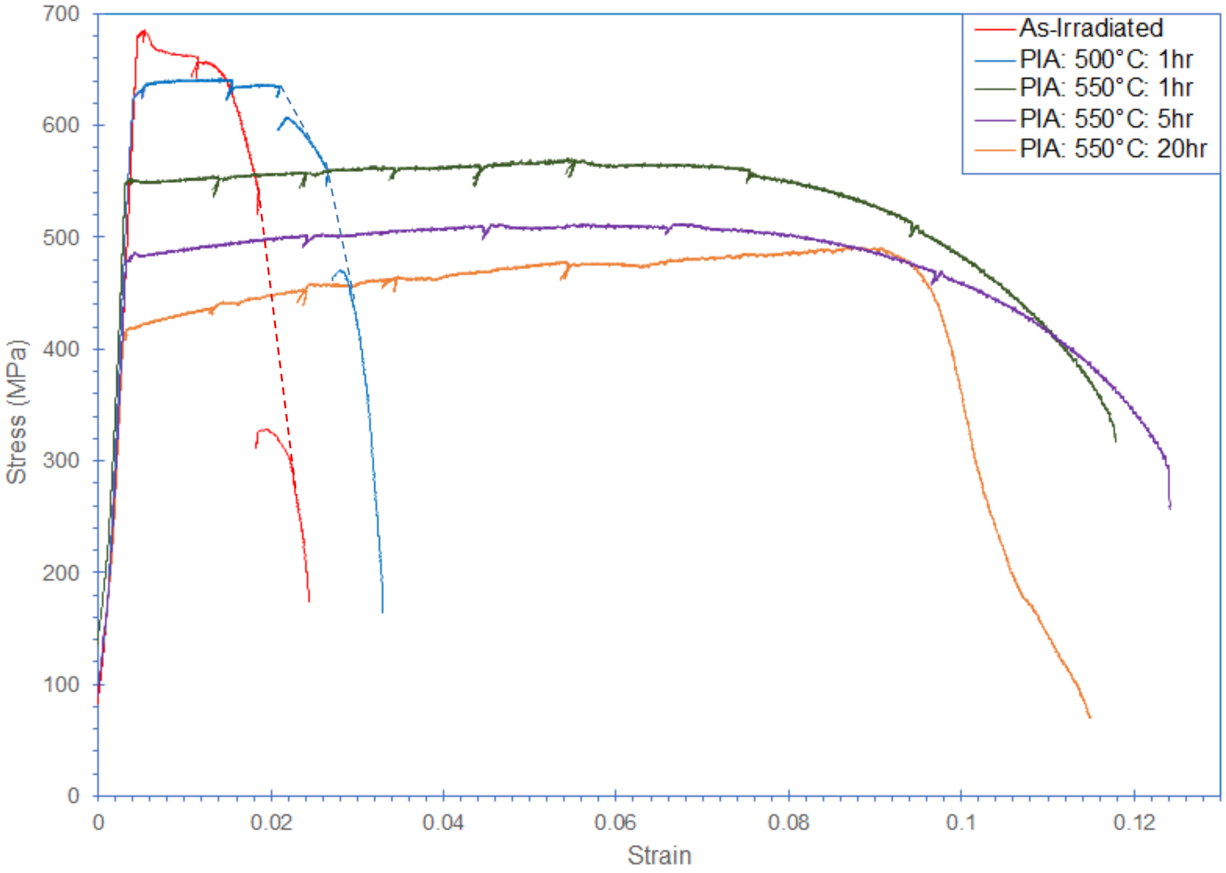

Figure 3-13: Change in the stress strain behavior because of specific annealing treatments: 500°C: 1hr, 550°C: 1hr, 550°C: 5hr, and 550°C: 20 hr.

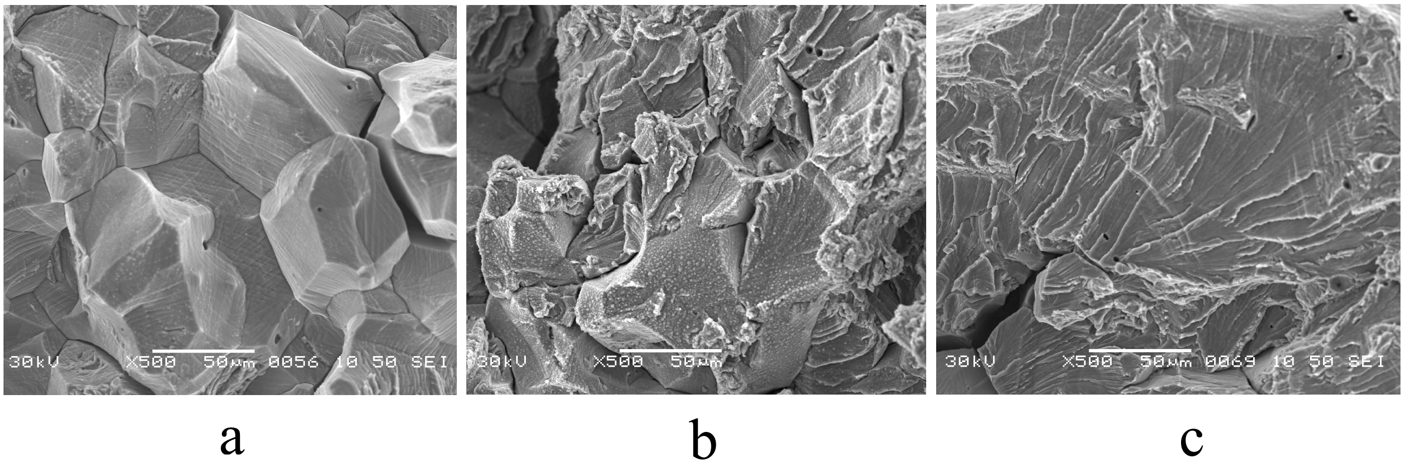

Figure 3-14: Example images from the T-5 (PIA 500°C: 1hr) specimen of the three primary modes of failure that were observed during the crack growth of the as-irradiated and PIA specimens: a) intergranular, b) mixed intergranular-transgranular, c) transgranular.

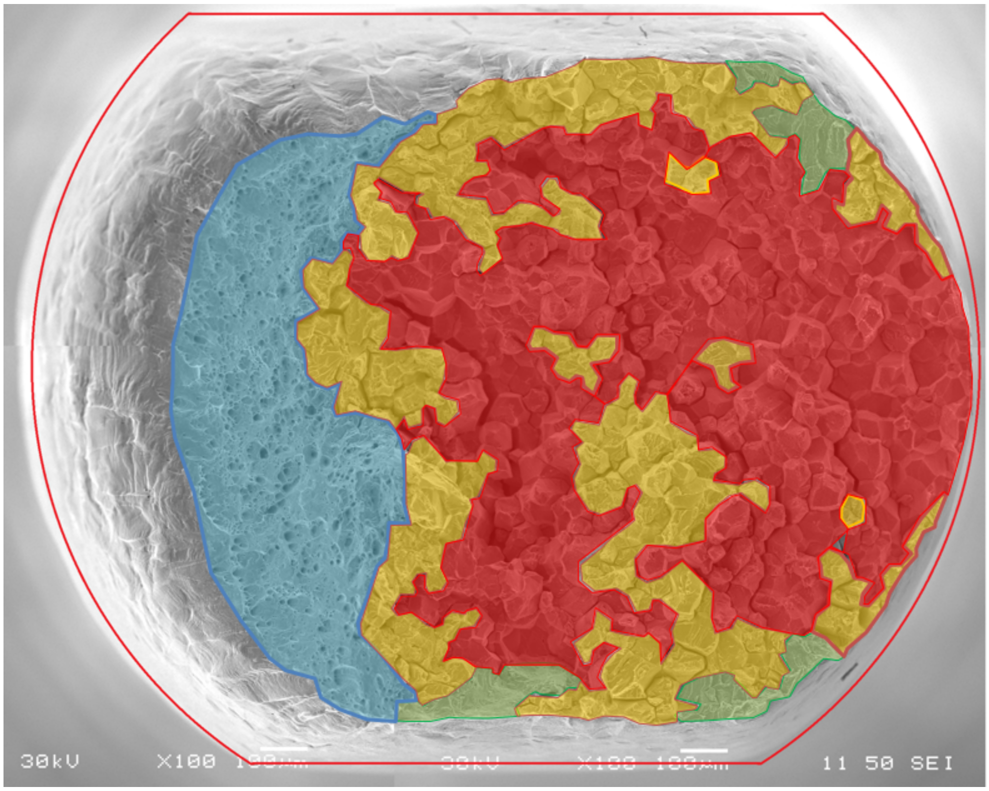
30kV X100 100µm
30kV X100 100µm 11 50 SEI

a

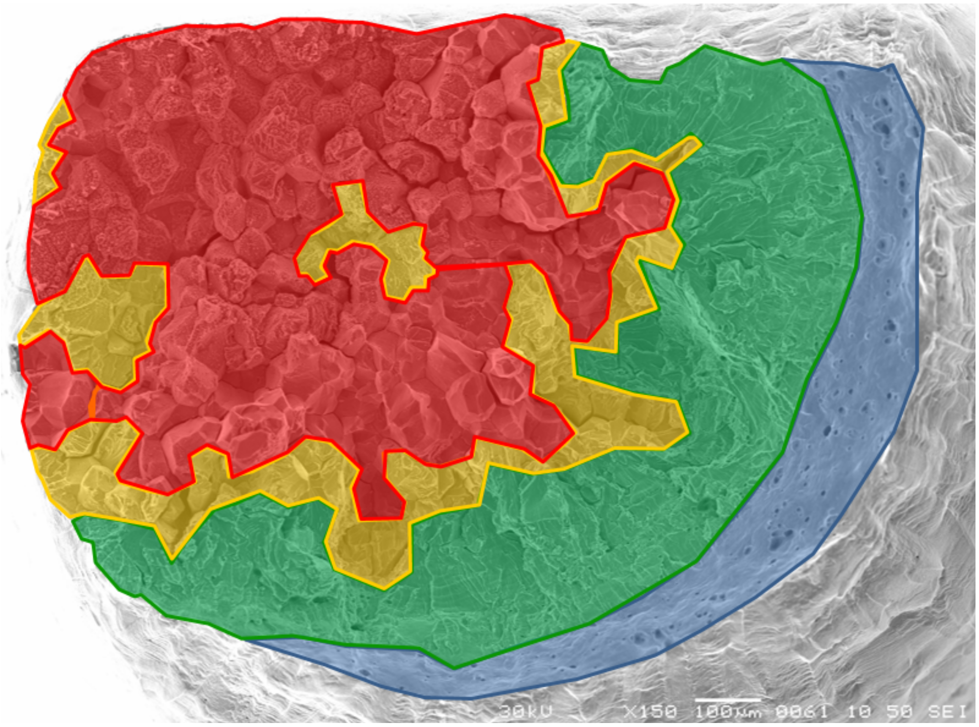
30kV X150 100µm 0061 10 50 SEI

b

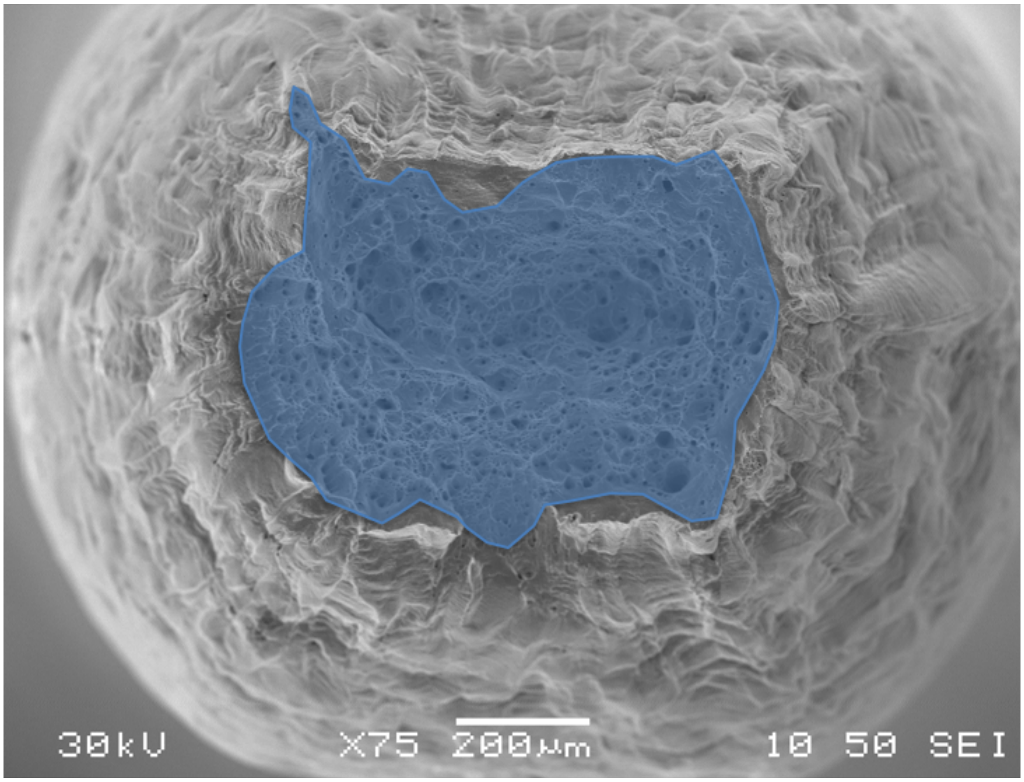

c

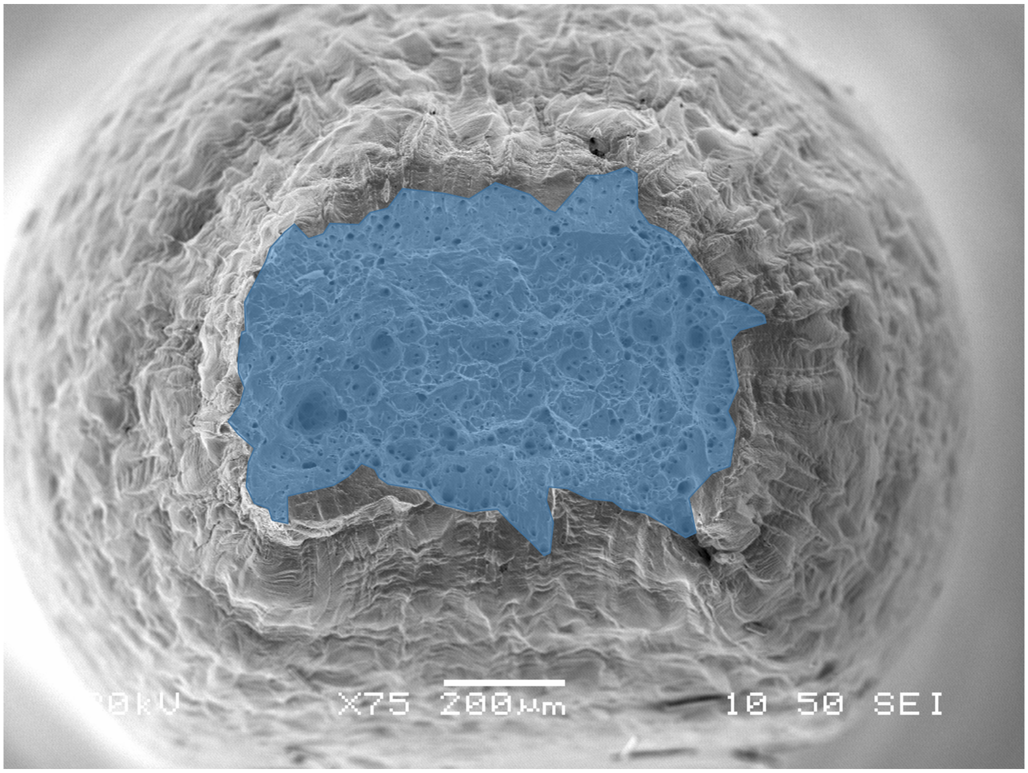

d

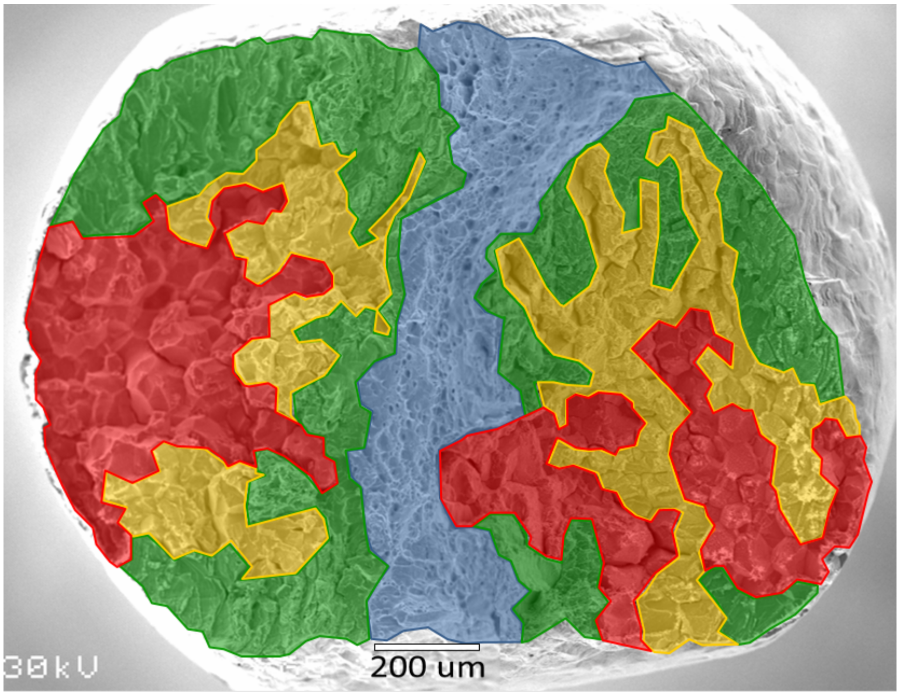

Figure 3-15: Comparison of the final fracture surface of the CERT tensile specimens: a) as-irradiated, b) PIA: 500°C: 1hr, c) PIA 550°C: 1hr, d) PIA 550°C: 5hr and e) PIA: 550°C: 20hr. Red is utilized to represent areas of intergranular failure, while green shows regions of transgranular propagation. Orange represents mixed IG/TG, while blue is ductile fracture.

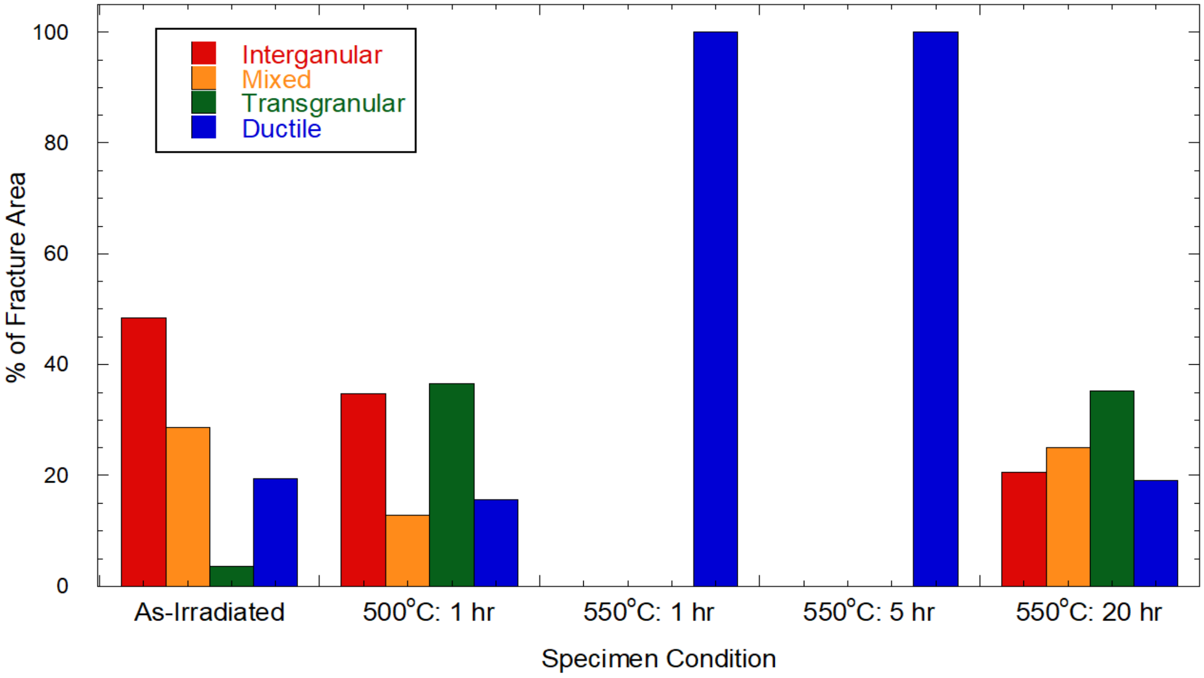

Figure 3-16: Change in the fracture morphology of the as-irradiated, PIA: 500°C: 1hr, PIA: 550°C: 1, 5, and 20 hr conditions.

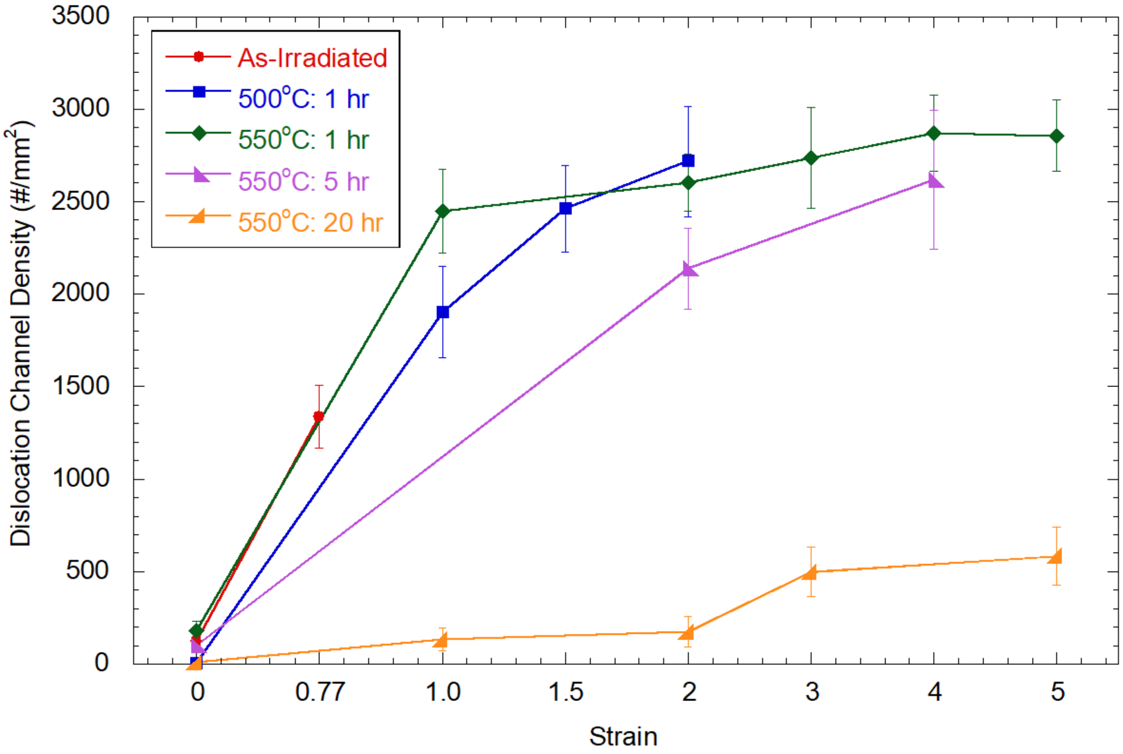

Figure 3-17: Change in the dislocation channel density of the failure region in response to increasing plastic strain, prior to crack growth or specimen necking.

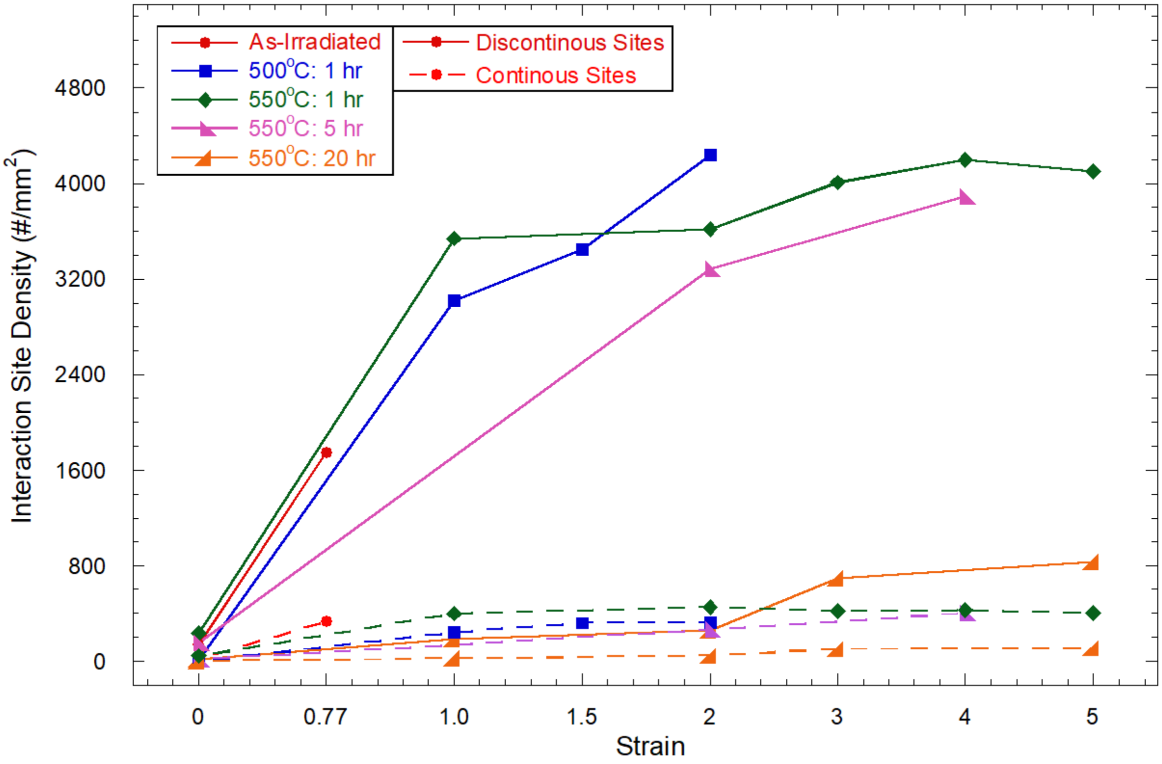

Figure 3-18: Change in the grain boundary-dislocation channel interaction site density of the failure region in response to increasing plastic strain.

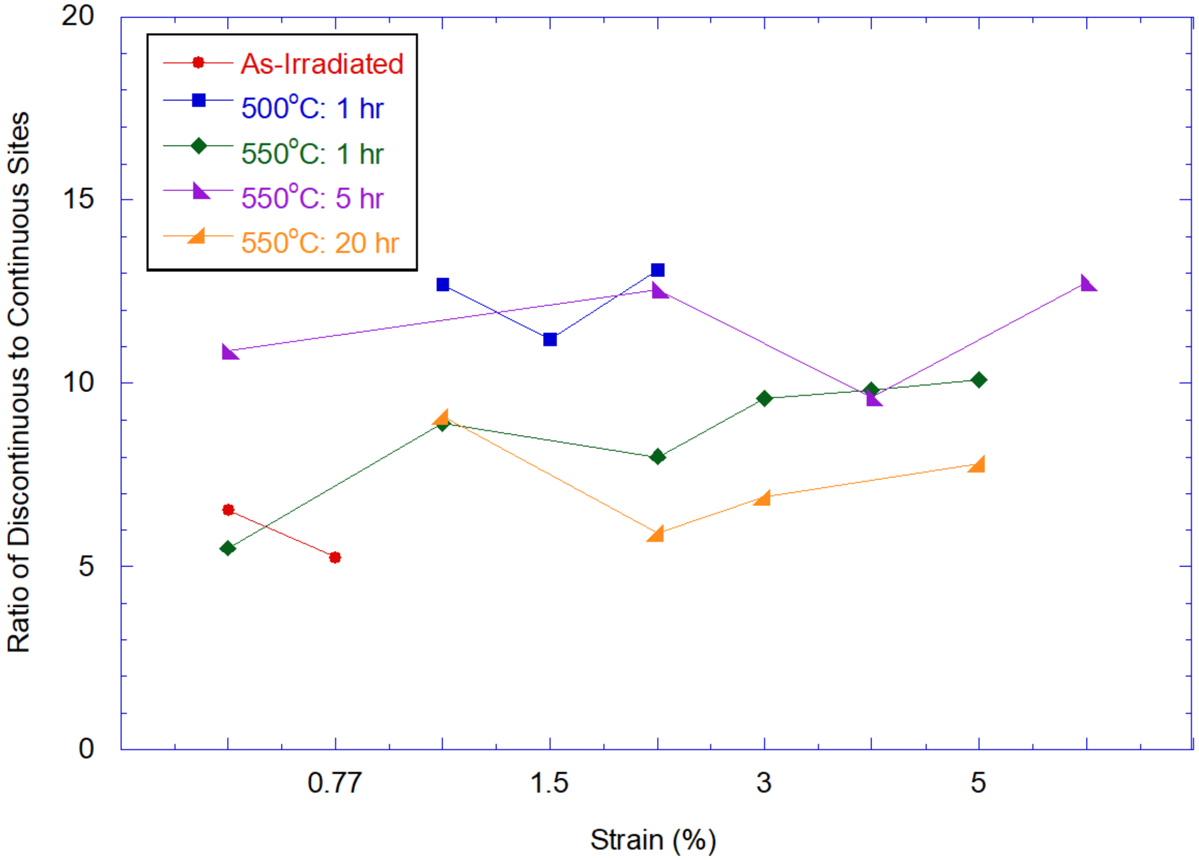

Figure 3-19: Change in the ratio of discontinuous to continuous grain boundary-dislocation channel interaction sites in the failure region. The ratio varies between ~5 to 15, but displays no trend with either PIA nor strain.

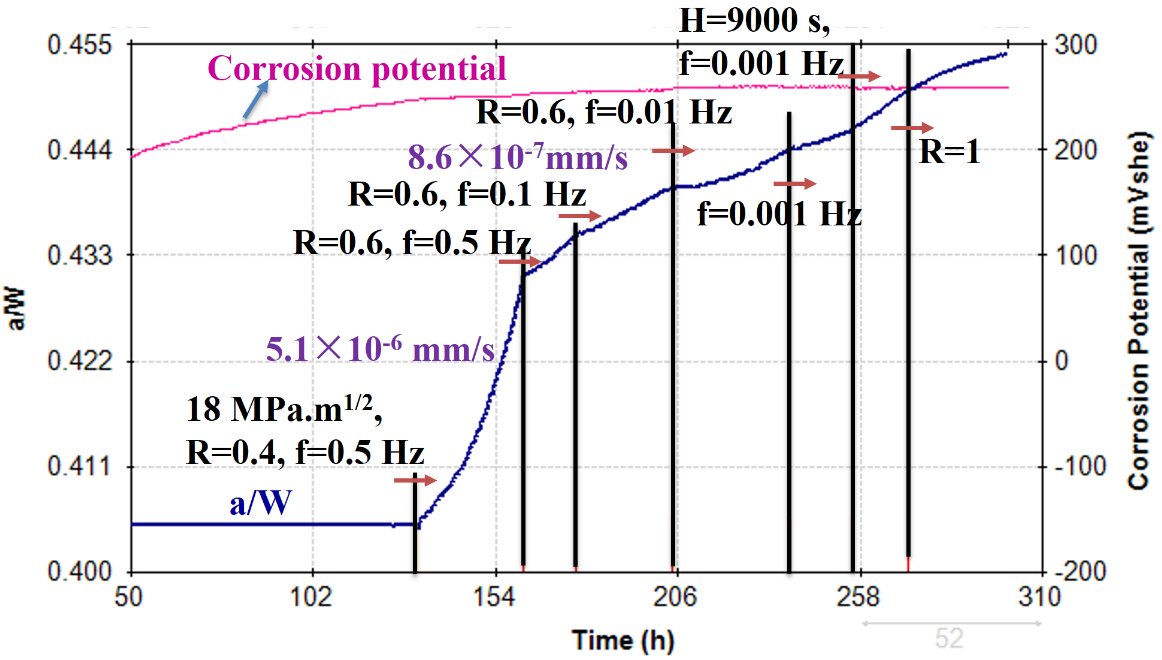

Figure 3-20: *a/W* and corrosion potential of RCT-3 in 288 °C water containing 2 ppm O_2.

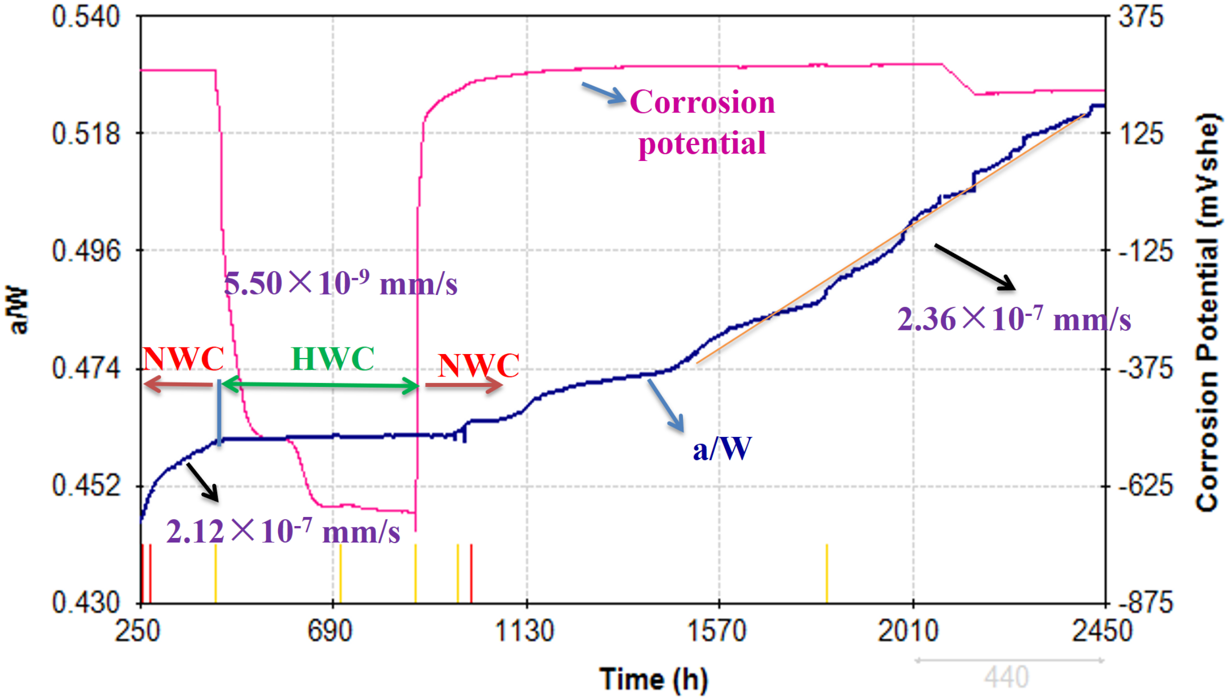

Figure 3-21: *a/W* and corrosion potential of RCT-3 in 288 °C water at *K* of 18 MPa•m$^{1/2}$.

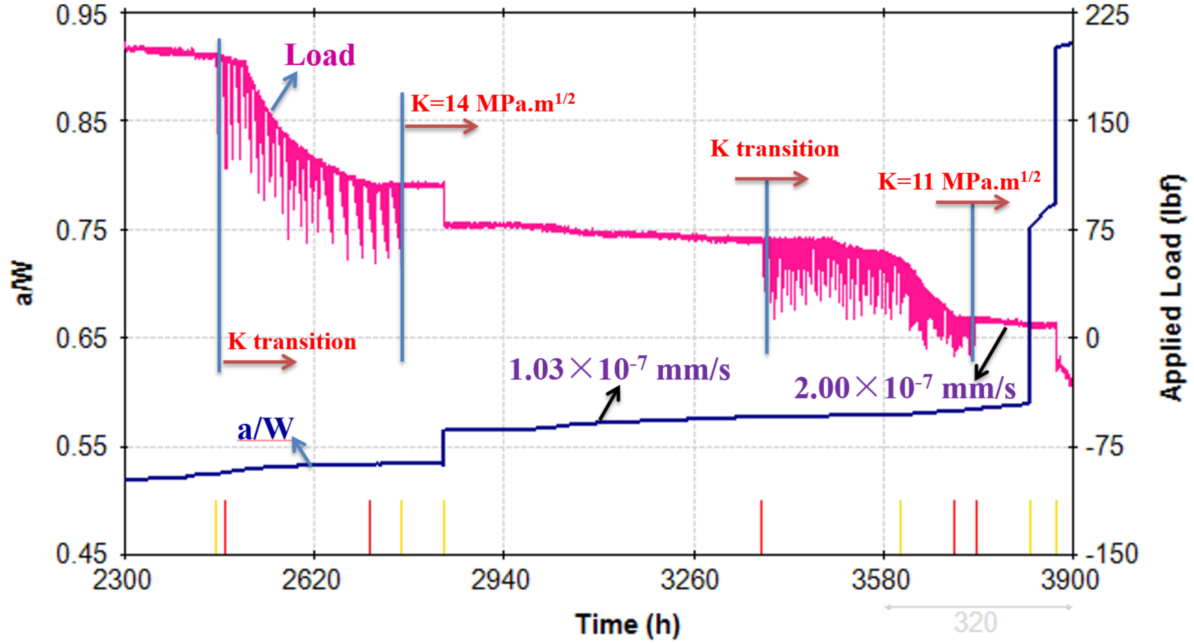

Figure 3-22: *a/W* and applied load of RCT-3 in 288 °C water during *K* transition from 18 to 11 MPa•m$^{1/2}$. The corrosion potential of sample was maintained at 218±2 mV (vs SHE).

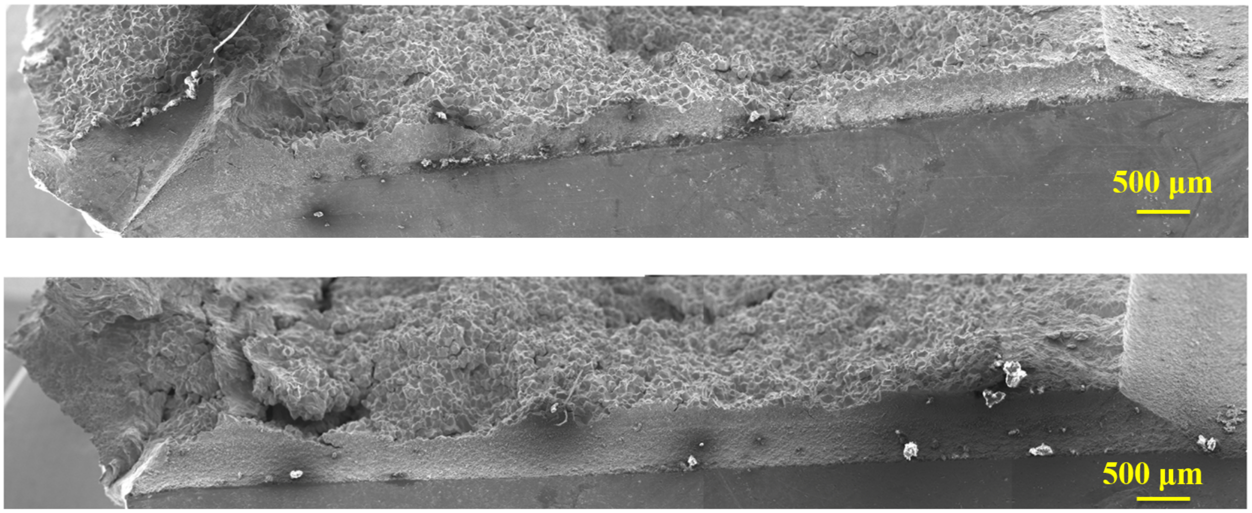

Figure 3-23: Side view images of fracture surface.

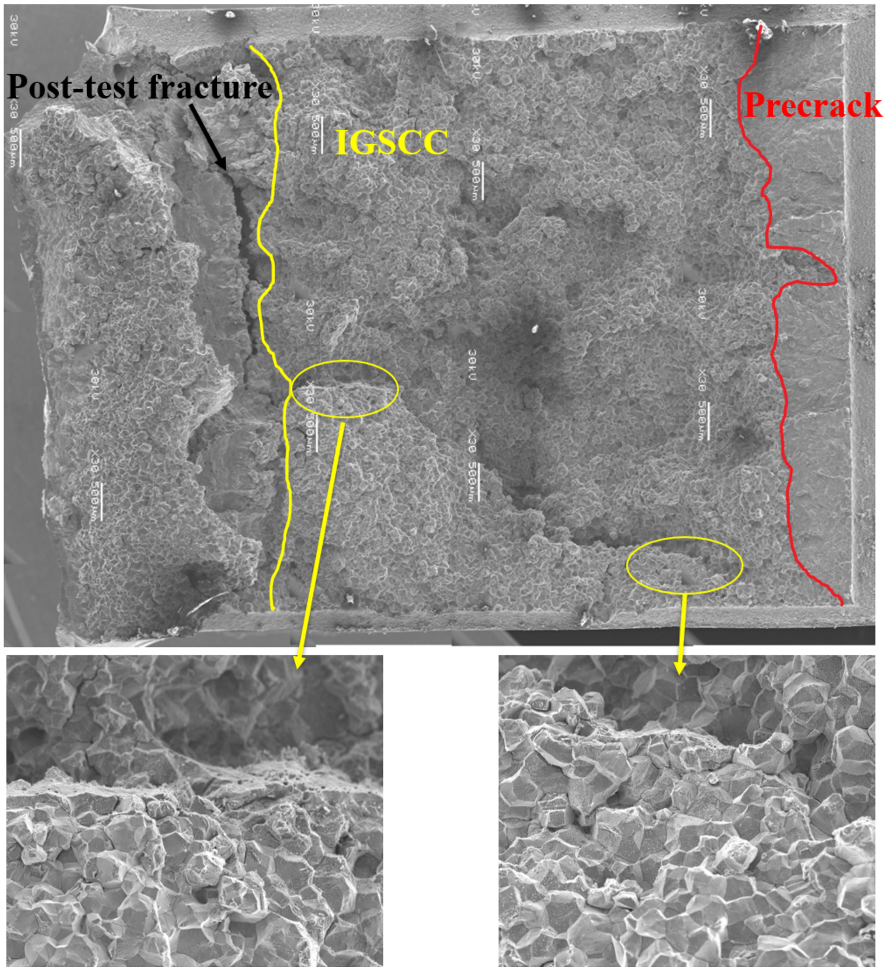

Figure 3-24: Fracture surface of RCT-3.

4. Discussion

4.1 Effect of PIA on the Irradiated Microstructure

4.1.1 Hardness

Micro-hardness measurements can provide an indication of the residual irradiated microstructure following post-irradiation annealing. Due to the ease in completing these measurements, the removal of hardness due to post-irradiation annealing is the most extensively studied attribute of neutron-irradiated specimens. Unfortunately, due to the cost and difficulty of studying neutron-irradiated material the available sources are still quite limited.

The change in the irradiation hardening with respect to the severity of the annealing treatment is shown in Figure 4-1, in which the black data points indicate hardening measurements from this study and the red data points are from other neutron irradiations in the literature [2]–[5], [8], [23]. Overall the data from this study appears to follow a similar trend with annealing parameter as other neutron-irradiated material in literature; though this material exhibits a slightly higher resistance to hardening removal at the moderate annealing temperatures of 500-550^{o}C.

4.1.2 Dislocation Loops

Annihilation of dislocation loops by annealing is by a diffusion mechanism driven by the vacancy supersaturation. Dislocation line tension and the stacking fault energy of the faulted loop cause the supersaturation of vacancies at the defects. During post-irradiation annealing, thermal vacancies are absorbed by faulted, interstitial loops, resulting in the decrease in loop size and annihilation of dislocation loops. The rate of absorption, and hence rate of change in loop size (dx/dt), is shown in the following equation [24]:

$$\frac{\mathrm{d}x}{\mathrm{d}t} = \frac{2D_{\mathrm{at}}}{b}\exp(-\Gamma b^2/kT) \times \left[\exp(-Ub^2/xkT) - \frac{\Sigma x_{\mathrm{i}} \exp - Ub^2/x_{\mathrm{i}}kT}{\Sigma x_{\mathrm{i}}}\right] \tag{4.1}$$

The first term shows the effect of stacking fault and the second term in the parenthesis shows the effect of dislocation line tension which is dependent on loop size. In the above equation, x is the radius of dislocation loop. D_{at} is atomic self-diffusion coefficient and $D_{\mathrm{at}} = b^3\, C_{eq}D$, C_{eq} is the thermal equilibrium concentration of vacancies. The term U ($\approx Gb^2/2$) is the dislocation line tension, Γ is the stacking fault energy, k is the Boltzmann constant, T is the absolute temperature, G is the shear modulus, and b is the magnitude of the Burgers vector.

The critical loop size can be calculated from the equation 4.1 by setting $\mathrm{d}x/\mathrm{d}t=0$, below which the loop size decreases with annealing time. The critical size at 500°C is calculated to be ~ 11 nm based on the size distribution of dislocation loops in the as-irradiated condition. It can be seen from Figure 3-4b that there is preferential annihilation of loops less than 11nm at 500°C which is consistent with the prediction of equation 4.1. The critical size (~13nm) calculated for annealing at 550°C does not change much from annealing at 500°C. If this is the case, loops larger than 13 nm are expected to coarsen and the mean loop size is expected to increase when coarsening dominates. However, the loop size distributions (Figure 3-4b) do not show significant coarsening of large loops at 550°C. Instead, annihilation of loops of all sizes but some very large loops (>30nm) was observed. Furthermore, the mean loop size showed virtually no change after annealing at 550°C up to 5 hours (Table 3-2). It is noteworthy that equation 4.1 holds only when the number of vacancies is conserved. As dislocation loops appear to shrink regardless of loop size at 550°C, external sources and sinks for vacancies must be activated and have contributed to annihilation of dislocation loops. As there are no cavities observed in the irradiated alloy, it is not clear what the external source of vacancies could be. One possible explanation is that there might exist cavities that are small enough and are not resolved by TEM.

As shown in equation 4.1, annealing temperature is critical for the annihilation of loops and therefore the effectiveness of PIA treatment. In fact, annealing at 400°C for 45 minutes does not change loop population in proton-irradiated stainless steels as shown in [6]. Renterghem *et al.* [8] also found that annealing at 400°C had almost no effect on the radiation-induced defects in AISI 304 that was irradiated up to 24 dpa in the decommissioned Chooz A reactor. In another study of a CW316 thimble tube irradiated at around 320°C up to 80 dpa in a commercial nuclear power reactor [9], the Frank loop density reduced to ~19% of the as-irradiated density after annealing at 500°C: 6h. They found that, after annealing at 550°C for 6 hours for both AISI304 and CW316, some large loops existed, however, rel-rod technique did not reveal faulted loops so they concluded that the large loops were probably perfect loops. Fukuya [3] found that the population of faulted loops barely changed after annealing at 400°C:1h and the density reduced to ~1/5 of the as-irradiated density after annealing at 550°C:1h in cold-worked SUS 316 stainless steels irradiated to 25 dpa in a PWR. In our study of BWR irradiated 304L SS, there is only ~29% of loops remaining after annealing at 550°C: 1h and ~11% left after 550°C: 5h (

Table). Annealing at 550°C for 20 hours results in negligible number density of dislocation loops compared to the as-irradiated condition.

Comparison of annihilation of dislocation loops with literature data is shown in Figure . Our study is in line with literature regarding the effectiveness of PIA temperature on annihilation of dislocation loops. The optimal annealing temperature to reduce loop population appears to be around 550°C. Annealing at this temperature would reduce the loop density significantly and longer annealing time can annihilation or unfault all Frank loops without the need of increasing temperature. Annealing temperatures of 400°C and below barely change the Frank loop population and temperatures 600°C and higher can potentially change the initial microstructure.

4.1.3 Solute Clusters

The effect of PIA on Ni-Si and Al-Cu clusters is shown in Figure 2. In general, both types of clusters exhibit an increase in size and a decrease in number density after PIA. Dissolution of solute clusters involves diffusion of solutes back into solution, which depends on the diffusivity of the solute at the annealing temperature. Clusters become larger and more diffuse after annealing because of the diffusion of solute away from the central core of the clusters. This is different from typical precipitate coarsening process, in which large precipitates grow larger at the expense of smaller ones. *Therefore, the increase of cluster size after PIA is not due to coarsening, rather the result of solute diffusion.* Silicon is known to be a faster diffuser than nickel in stainless steel [25] and while aluminum and copper have similar diffusion rates in iron [26], [27], aluminum is more heavily segregated in the clusters, while having a lower bulk concentration, thus driving the faster observed diffusion of aluminum. This results in the increase in Ni-to-Si ratio and decrease in Al-to-Cu ratio in the clusters after annealing as shown in Figure 2. Figures 4-4 and 4-5 show the normalized evolution of the nickel-silicon and aluminum-copper clusters from the as-irradiated to 550^{o}C: 20 hr annealed condition. Note that in the as-irradiated condition, the Ni-to-Si ratio of the central core of the cluster is ~5:1, which is greater than the 3:1 ratio in the γ' (Ni_3Si) phase. The ratio increases to ~6.5:1 after annealing at 550°C:1h and further increases to ~10:1 after annealing at 550°C:20h. The increase in Ni-to-Si ratio after annealing is consistent with the earlier data in Table 3-3 but differs in value as the table shows the integrated ratios over all observed clusters at each condition. Fast diffusion of Si after annealing leads to depletion of Si in the outer region of the clusters. In the case of annealing at 550°C:20h, only the center ~2 nm of the cluster shows enrichment of Si even though the cluster is more than 8 nm in diameter as defined by enrichment of Ni. Because the large difference in the extent of enrichment of Ni and Si, the ratio of the integrated nickel and silicon in the cluster is ~15:1, which is higher than the 10:1 at the core.

Ni-Si-rich clusters are commonly observed in irradiated stainless steels. In neutron irradiated 304/316SS at high doses, they are typically in the form of γ' or G phase, which can be characterized using traditional TEM dark field technique. However, because of the resolution limitation of traditional TEM, precipitates less than 2 nm or solute clusters may be difficult to characterize. For instance, the average size of γ' in SUS 316 stainless steels irradiated to 25 dpa in a PWR is around 2 nm [3] and there is a high probability of missing some small precipitates using TEM. Fukuya *et al.* [3] found that the average size of γ' is nearly constant after annealing at 400, 500 and 550°C for an hour with slight increase in number density in the SUS316. Van Renterghem *et al* [9] also found the size γ' barely changed after annealing at 500°C for 6h in CW316 and slightly increased after annealing at 550°C for 6h. The γ' appeared to have dissolved after annealing at 550°C for 6h. The inconsistency with literature regarding the annihilation of γ' or Ni-Si clusters is probably due to the characterization technique used. Electron diffraction in the TEM cannot detect solute clusters when they are still in the precursor stage of the γ' phase. Thus, if the γ' particles become Ni-Si clusters after annealing due to diffusion of Ni and Si, they would not be detected by TEM and they are considered "dissolved" from the TEM point of view. But there might still be solute clusters which can be detected by APT.

4.1.4 Relation between Irradiation Hardening and Microstructure

The relationship between the measured irradiation hardening and the evolution of the irradiated microstructure has been often studied for many decades [28]–[30]. Most often the irradiated microstructure exists as a distribution of barriers that impede dislocation motion, and can be measured through the dispersed barrier hardening model as given by:

$$\Delta\sigma_{y,i} = \alpha_i M\mu b\sqrt{N_i d_i} \tag{4.2}$$

Where $\Delta\sigma_{y,i}$ represents the increase in the yield stress arising from obstacles of density, N_i, and size, d_i, and strength factor of α_i. M, μ, and b represent the Taylor factor, shear modulus and Burgers vector of the material, respectively. The strengthen factor ranges between 0 and 1, where a value of 1 represents a perfectly hard barrier, around which a dislocation must bow. As multiple irradiation defect types exist in an irradiated material, a method is needed to measure the superposition of multiple defects of varying strengths, sizes, and densities. The most common superposition methods in literature [29] include the linear sum (LS) and root-square-sum (RSS) as shown in Equations 4.3 and 4.4, respectively.

$$\Delta\sigma_{y,LS} = \sum_i \Delta\sigma_{y,i} \tag{4.3}$$

$$\Delta\sigma_{y,RSS} = \sqrt{\sum_i \left(\Delta\sigma_{y,i}\right)^2} \tag{4.4}$$

The LS method is most often used when the various obstacle types are at dissimilar strengths or if they influence dislocation movement at differing length scales. In these cases, the defects do not influence one another, thus the overall strengthening is simply a sum of each of the individual barrier strengths. In the case of barriers with similar strengths, the RSS method is preferred. When the barriers are of similar strengths then a moving dislocation is unable to distinguish between the two defect types, thus the sum of the areal densities of each defect type must be combined to account for the effective defect spacing [30].

Often in literature the barrier strengths of common irradiation defects, i.e. dislocation loops, black dots, precipitates, are assumed based on prior work [3], [8], [29], [31], however, as this project covers an extensive set of annealing with a well-documented microstructural analysis, it is possible to calculated the respective strengthening factors of dislocation loops (α_L), Ni-Si (α_{Ni}), and Al-Cu (α_{Al}) solute clusters, using both the LS and RSS methods given by:

$$\Delta\sigma_{y,LS} = \alpha_L M\mu b\sqrt{N_L d_L} + \alpha_{Ni} M\mu b\sqrt{N_{Ni} d_{Ni}} + \alpha_{Al} M\mu b\sqrt{N_{Al} d_{Al}} \quad , \tag{4.5}$$

$$\left(\Delta\sigma_{y,RSS}\right)^2 = (\alpha_L)^2\left(M\mu b\sqrt{N_L d_L}\right)^2 + (\alpha_{Ni})^2\left(M\mu b\sqrt{N_{Ni} d_{Ni}}\right)^2 + (\alpha_{Al})^2\left(M\mu b\sqrt{N_{Al} d_{Al}}\right)^2 . \tag{4.6}$$

For the as-irradiated and PIA conditions of 500°C:1hr, 550°C: 1 and 20 hrs, $\Delta\sigma_y$ was calculated as the difference between the measured yield stress and that of the unirradiated 304L condition (211.5 MPa). N and d are the respective number densities and sizes measured at each condition, while the constants: $M = 3.06$ [30], $\mu = 76$ GPa, and $b = 0.255$ nm [31]. After inserting the known quantities into Equations 4.5 and 4.6, a least squares fit with an intercept of zero was applied to calculate the unknown strengthening factors for each defect type, as can be seen in Table 4.1. Using the linear sum method, the three defect types were found to have relatively similar strengths, though the strength of dislocation loops was calculated to be higher. The RMS method provided values similar to those using the LS, though the calculated strength of the dislocation loops and Ni-Si solute clusters were comparably increased, while the strength of the Al-Cu clusters was near negligible. Unfortunately, there is little existing literature in measuring the strength factors of solute clusters, though prior work by Toyama *et al.* [31] calculated an $\alpha_{Ni} = 0.11$ for solute clusters enriched in nickel and silicon. Furthermore, literature has suggested the strengthening factor of dislocation loops to typically be in the range of 0.2-0.5 [29], [30]. As such, it seems more likely that the RSS method is more applicable in predicting strengthening from the irradiated microstructure for the material studied in this project, as the calculated values are more like those typically found in related literature.

It is worth noting as well that these calculations assume that the strengthening factor for each defect type remains constant with annealing, and thus the strengthening effect is directly related to the changes in defect density and size. This is likely not the case for solute clusters, as the strengthening for these defects likely arises more from the solute concentrations, thus during annealing although the cluster itself expands in size the solute concentration becomes less. As such it is likely that while an as-irradiated solute cluster may be of a smaller size, it is likely more difficult for moving dislocation to cut through as compared to the larger solute clusters observed after annealing at 550^{o}C: 20 hr, due to the difference in solute concentration. This effect is planned to be investigated in a later more detailed study.

4.1.5 Grain Boundary Segregation

Radiation-induced segregation causes composition gradients of Cr, Ni, Fe, Si etc. at the grain boundary. The removal of composition gradients by post-irradiation annealing is governed by the equilibrium vacancy concentration and the composition gradients at grain boundaries drive the motion of thermal defects during annealing [6] The modified inverse- Kirkendall (Perks) model developed by Allen et al. [32] was successfully used to simulate the behavior of composition gradients of the major alloying elements during post-irradiation annealing of 304 SS alloys by Busby et al. [6].

The effect of PIA on the composition profiles across the grain boundary for Cr, Ni, Si, and P is shown in Figure and its effect on the magnitude of RIS is shown in Figure a. Annealing at 550°C for 5 hours results in significant reduction in grain boundary segregation for all the elements. However, the recovery rates appear to be different and they are probably linked to their diffusivities at the annealing temperature. There is still significant depletion of Cr and enrichment of Ni after annealing at 550°C for 20 hours. In contrast, P has returned to the bulk concentration after annealing at this annealing condition. Figure b shows the remaining RIS of Cr, Ni and Si after post-irradiation annealing normalized to the as-irradiated condition. The recovery is in the order of Si > Ni > Cr at 550°C, as expected by their respective diffusion rates [25]. The faster recovery of Si than Ni is consistent with the observation of annealing of Ni-Si clusters in which the faster diffusion of Si leaves a higher Ni-to-Si ratio after annealing. The recovery of grain boundary Cr after annealing is compared to the literature data in

Figure . It is in line with the literature data and confirms that the removal of RIS is a thermal diffusion controlled process.

4.2 Effect of PIA on Localized Deformation

Localized deformation and its response to PIA treatments was measured via SEM following each stress/strain increment as previous literature studies have observed close correlations between dislocation channeling and IASCC susceptibility [13], [14]. However, as these literature studies are quite recent, there have been no previous localized deformation studies on PIA of neutron-irradiated samples, and data on neutron-irradiated localized deformation itself is quite limited. As such, it is difficult to find a comparative benchmark for our measured results of dislocation channel density; however, a previous work performed by Stephenson *et al.* [22] using 4-point bend tests on neutron-irradiated stainless steel specimens, displayed a comparative level of dislocation channel density as our as-irradiated condition. This similarity in dislocation density with strain was observed despite the differences in alloy and irradiation condition, as shown in Figure 4-8. Overall, there is a good agreement between the measured dislocation channel density as compared to plastic strain, particularly below 2% strain. However, the 4-point bend specimens measured by Stephenson *et al.* continue to increase in dislocation channel density at strains above 2%, whereas the PIA material from this project were observed to saturate at a specific level of deformation. It is unknown whether this is a factor of the as-irradiated material (as this project's as-irradiated specimen displayed crack initiation by 1% strain), the straining method (i.e. tensile vs. 4-point bend), or if it a variable of the different alloys examined.

The dislocation channel density was observed to be relatively unaffected by the annealing at 500°C: 1hr and 550°C: 1hr, but was reduced following the 550°C: 5 hr annealing, and significantly reduced after PIA at 550°C: 20 hr. This result seems to suggest that the density of dislocation channels is primarily affected by the irradiation defect densities, which agrees with previous work by Jiao *et al.* [13], in which the dislocation loop density was the primary contributor to the development of localized deformation. Recall that the as-irradiated population of faulted dislocation loops was completely removed after annealing at 550°C: 20 hr. However, the high channel density observed in the 550°C: 1hr annealing condition, which had a significant reduction in the dislocation loop density as well as high ductility, appears to counter this theory.

It has been theorized that localized deformation contributes to IASCC susceptibility through the build-up of dislocations at the interaction site between a discontinuous channel and a grain boundary [15], [16], as evidenced by the higher cracking fraction of discontinuous channels. With regards to PIA treatments, it is expected that the with a decrease in the irradiated microstructure, the dislocation channel density may be reduced by the same relative amount, however, our results instead indicate a threshold level which is required for significant dislocation channeling. Thus, in the case of the as-irradiated state and lower annealing treatments, i.e. 500°C: 1hr and 550°C: 1hr, a significant portion of the plastic deformation could only be through the formation of dislocation channels, hence the higher density. While for the 550°C: 20hr condition most of the plastic strain could be homogeneously accommodated, hence the much lower observed channel density. However, it can be speculated that even for the 500°C: 1hr and 550°C: 1hr conditions a certain portion of the bulk plastic strain may have been homogeneously distributed. The relative amount of strain included in dislocation channels, may reflect on the resultant IASCC susceptibility.

It has been observed that the strain included in dislocation channels can be related to the channel density and height [15], and thus by comparing to bulk plastic strain the amount of strain homogenously distributed can be learned. Unfortunately, this study did not include a measurement of average channel heights after each straining increment, which may have further supported this theory in the case that the 550°C: 1hr had a lower average height as compared to the as-irradiated and 500°C: 1hr conditions, which showed similar dislocation channel densities, but a much increased IASCC susceptibility.

It also appears that the slip transmission of dislocation channels across grain boundaries depends more on material conditioning, as the ratio of discontinuous to continuous interaction sites remains relatively unaffected by PIA over the range of annealing treatments examined for this project, as previously shown in Figure 3-19.

4.3 Effect of PIA on the IASCC Susceptibility

As previously mentioned, the IASCC susceptibility of neutron-irradiated tensile specimens is often measured as the % of intergranular fracture on the fracture surface in literature. As such, for the sake of comparing to previous PIA results, this value will be utilized for comparing the relative removal of IASCC susceptibility. Following CERT straining to failure, the fracture and gage surfaces were fully examined by SEM; where the separate fracture regions were quantified to determine %IG, %TG, % mixed IG/TG, and % ductile failure.

The as-irradiated tensile specimen was observed to have the highest degree of IASCC susceptibility, with 48.4% of the final fracture area by a pure intergranular fracture, 28.6% of the region showed a mixed intergranular-transgranular fracture, while only 3.6% showed a pure transgranular failure and the remaining 19.4% was the final ductile failure of the specimen. As seen in Figure 4-9, this susceptibility of 48.4% IG failure is moderate as compared to other PIA studies in the literature. Only two cases reported in the literature had a lower %IG fracture of the as-irradiated material: a 316L steel at 12 dpa [2] and a 304 at ~4 dpa [4]. In general, most other studied alloys had both a higher degree of irradiation damage and higher %IG fracture in the as-irradiated condition [2], [3], [8].

Annealing at 500°C: 1hr and 550°C:20 hr resulted in a lower percentage of pure intergranular fracture of 34.9% and 20.6% respectively. The degree of mixed mode fracture seemed to vary between the studied conditions while the about of transgranular fracture was significantly enhanced after annealing to ~30% of the fracture area for both examined conditions. It is worth noting that characterizing IASCC susceptibility by %IG produces a higher susceptibility for the 550°C: 20 hr condition than expected. This tensile specimen initiated multiple cracks, presumably around the same strain level, and two crack began to grow from opposite sides of the tensile specimen slightly off plane from one another. After both cracks progressed through roughly 50% of the cross section, the specimen failed as a shear between the two separate crack planes. As such the final fracture, cross section displays two independent crack fronts, thus a higher percentage of pure intergranular fracture. Annealing at both 550°C: 1 and 5hr caused a full mitigation of IASCC susceptibility and displayed a 100% ductile fracture.

Figure 4-9, shows the change in % of intergranular failure with varying PIA treatments for both this material and several similar alloys in literature. By comparison, many of the other alloys studied in literature display a faster removal of IASCC susceptibility than the 304L alloy studied in this project when examining all four PIA conditions, though the exact reason for this behavior is not known. A possible exception to this is a 304 alloy at 18 dpa studied by Katsura *et al.* [2]; this material displayed a much higher as-irradiated susceptibility (95% IG), but was seen to stabilize at ~45% intergranular fracture after annealing 500°C: 10 hr. However, due to the lack of additional annealing treatments, the behavior of the 304 alloy after annealing at higher temperatures is unknown. However, if one excludes the 550°C: 20 hr annealing condition, it is clear that the mitigation of IASCC susceptibility follows a very similar trend to that in literature.

As there is a wide variety of initial alloy conditions and test environments (the previously shown literature data was a mixture of CERT experiments in both simulated BWR-NWC and PWR environments), it is a standard practice to normalize each independent material by the susceptibility of the as-irradiated material, as shown in Figure 4-10. Due to both the lower initial susceptibility of our examined material, and its apparent resistance to IASCC mitigation, the variance of our results from the previously completed PIA literature on neutron-irradiated materials becomes more evident. The 500°C: 1hr condition displayed ~70% of the as-irradiated susceptibility, with 550°C: 1 and 5hr conditions having 0% susceptibility, while the 550°C:20 hr condition has ~40% of IASCC susceptibility remaining. The 500°C: 1hr, 550°C: 1 and 5hr conditions still fit within the range of literature data, though the 500°C: 1hr condition clearly lies within the upper limit. Both due to its relatively high %IG and the lack of more experiments after high temperature annealing, the 550°C:20 hr clearly lies outside the literature trend as the other high temperature specimens have been fully mitigated of IASCC susceptibility, increasing that the suspicion that this 550°C: 20 hr specimen may have an unknown issue causing it to be an enhanced susceptibility.

4.4 Key Processes Responsible for IASCC Susceptibility

Since IASCC was discovered, significant progress has been made in understanding the underlying mechanism. Many factors including radiation-induced segregation (RIS), yield strength/irradiation hardening, localized deformation, have been shown to correlate with IASCC, but unfortunately, none of these alone is sufficient to cause IASCC. It is worth noting that, even though factors such as yield strength and localized deformation have been linked directly to IASCC, they should be considered secondary in root analysis as they all originate from the fundamental irradiated microstructure. In fact, PIA affects irradiation hardening and localized deformation by changing the underlying irradiated microstructures. The primary cause of IASCC should be traced to the "persistent" damage induced by irradiation. The two dominant microstructures induced by irradiation are dislocation loops and solute clusters (Ni/Si clusters or γ'-phase) in 304 stainless steels.

In general, the irradiated microstructure is expected to influence the irradiation hardening, and hence possibly IASCC susceptibility, as a function of the defect density and average size. Based on the theoretical hardening in a matrix, these factors are compared as a function of $\sqrt{Nd}$, where N is the number density of the irradiation defect and d is the average defect size [33]. Figure 4-11 compares the IASCC susceptibility, as measured by the fraction of intergranular fracture, and the $\sqrt{Nd}$ of the three observed microstructural defects: dislocation loops, Ni-Si and Al-Cu solute clusters, displayed in orange. It can be observed that the theoretical impact of the microstructure generally decreases with a decreased IASCC susceptibility, excepting the Al-Cu clusters at the 550°C: 5hr condition as previously discussed. However, while the 550°C: 1 and 5hr conditions have a higher theoretical impact from the residual microstructure as compared to the 550°C: 20hr condition, they displayed a full mitigation of IASCC susceptibility.

While previous PIA literature has indicated a clear relation between IASCC susceptibility and the irradiation hardening or yield stress [3], likely in relation to the reduction of the irradiated microstructure. In general, this study has also indicated a general trend between the irradiation hardness and yield stress and the measured IASCC susceptibility, as shown in Figure 4-11, where the mechanical properties are displayed in blue. Once again this trend is broken by the the PIA treatment of 550°C: 20hr, whereas 550°C: 1 and 5hr conditions have a higher irradiation hardening, but a reduced susceptibility. It is important to note that the fraction of intergranular fracture area, is not the only representation of the IASCC susceptibility of a material, but the overall ductility is also relevant. Figure 4-11 displays a comparison between the intergranular fracture and the ductility, as measured by 1/ε, where a good agreement is observed between an increased ductility and decreased IASCC susceptibility. Though once again the 550°C: 20 hr condition shows a rather high ductility while also having an increased IASCC susceptibility.

The decrease in both the depletion of chromium and enrichment of nickel and silicon grain boundary segregation with annealing is also displayed in Figure 4-11, where the RIS data is plotted in green. With an increase of annealing time and temperature the segregation is increasingly reduced, but the lack of a complete data set makes a full comparison to the IASCC susceptibility difficult.

Overall, it was observed that PIA treatments are successful in reducing the irradiated microstructure, irradiation hardening, and IASCC susceptibility of 304L stainless steel BWR-irradiated to a dose of 5.9 dpa. While the irradiated microstructure, radiation-induced segregation, and hardening were all incrementally decreased with increasing annealing time and temperature, IASCC susceptibility was not evenly reduced. A full mitigation of IASCC occurred after 550^{o}C: 1 and 5hr annealing treatments, but IASCC susceptibility was still displayed after 550^{o}C: 20hr annealing. Based on this data, it is suspected that the 550^{o}C: 20 hr tensile specimen examined is an outlying result as compared to the remaining data. However, due to the small size of the data set, and the high value of neutron-irradiated material, it is difficult to fully remove the specimen, and a later examination is planned to study the specific irradiated microstructure of this specimen.

Table 4-1: Calculation of the strengthening factors (α) of the irradiated microstructure following annealing treatments, via both the linear sum and root-square-sum methods.

Calculation Method	Calculated Strengthening Factor (α)		
	Dislocation Loop (α_L)	Ni-Si Clusters (α_{Ni})	Al-Cu Clusters (α_{Al})
Linear Sum (LS)	0.127 ± 0.040	0.025 ± 0.069	0.060 ± 0.074
Root-Square-Sum (RSS)	0.190 ± 0.096	0.089 ± 0.076	0.016 ± 0.091

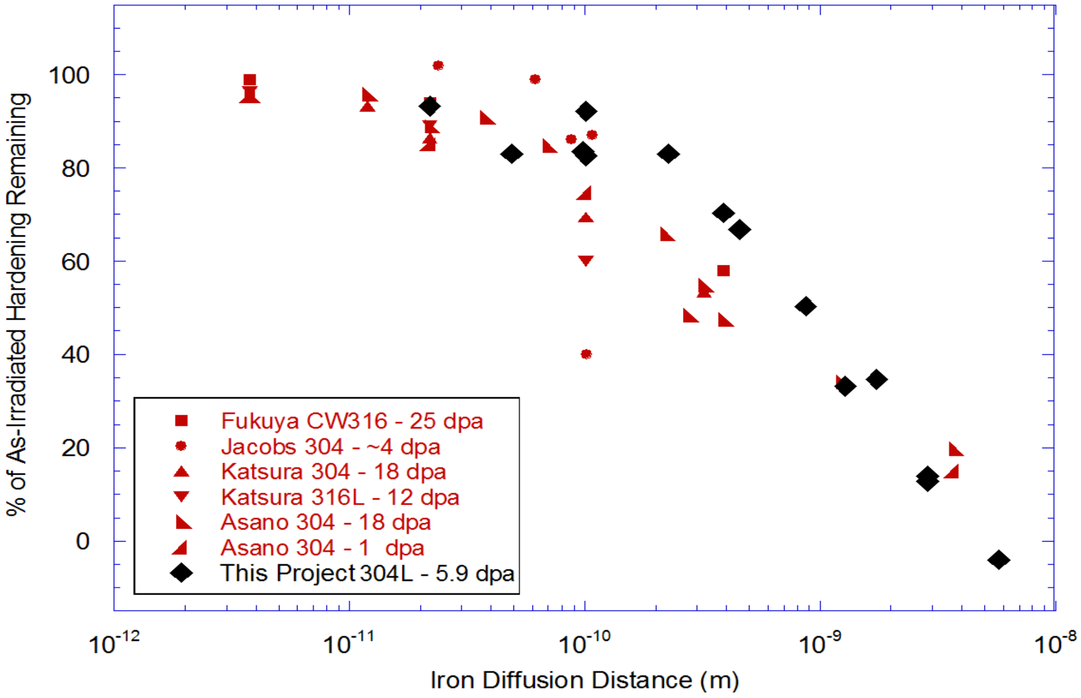

Figure 4-1. Comparison of the removal of the irradiation hardening following a wide variety of annealing times and temperatures between the material for this project (304L at 5.9 dpa) and various other neutron-irradiated stainless steels in literature [2]–[4], [23].

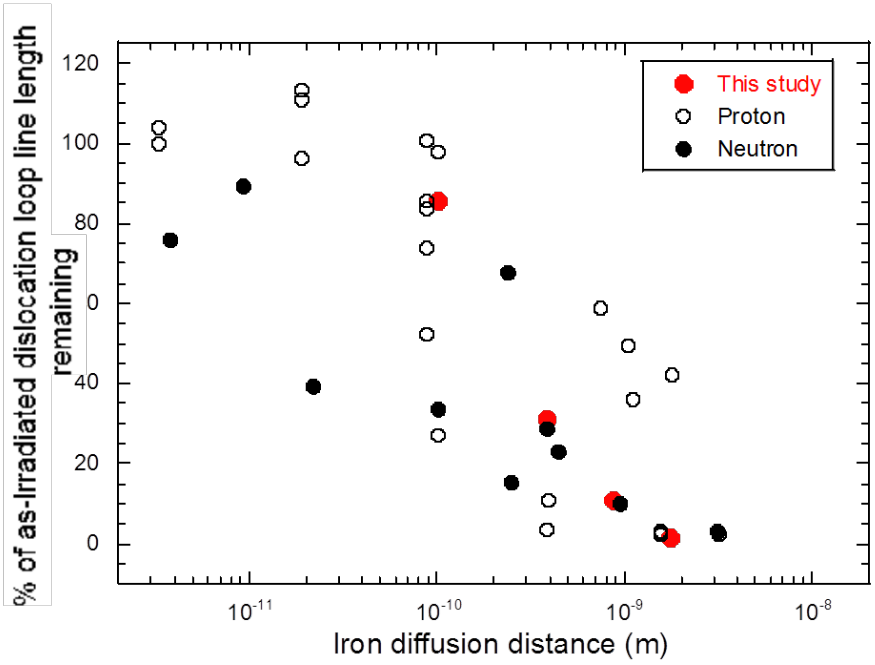

Figure 4-2. Comparison of dislocation loop line remaining after post-irradiation annealing with literature data.

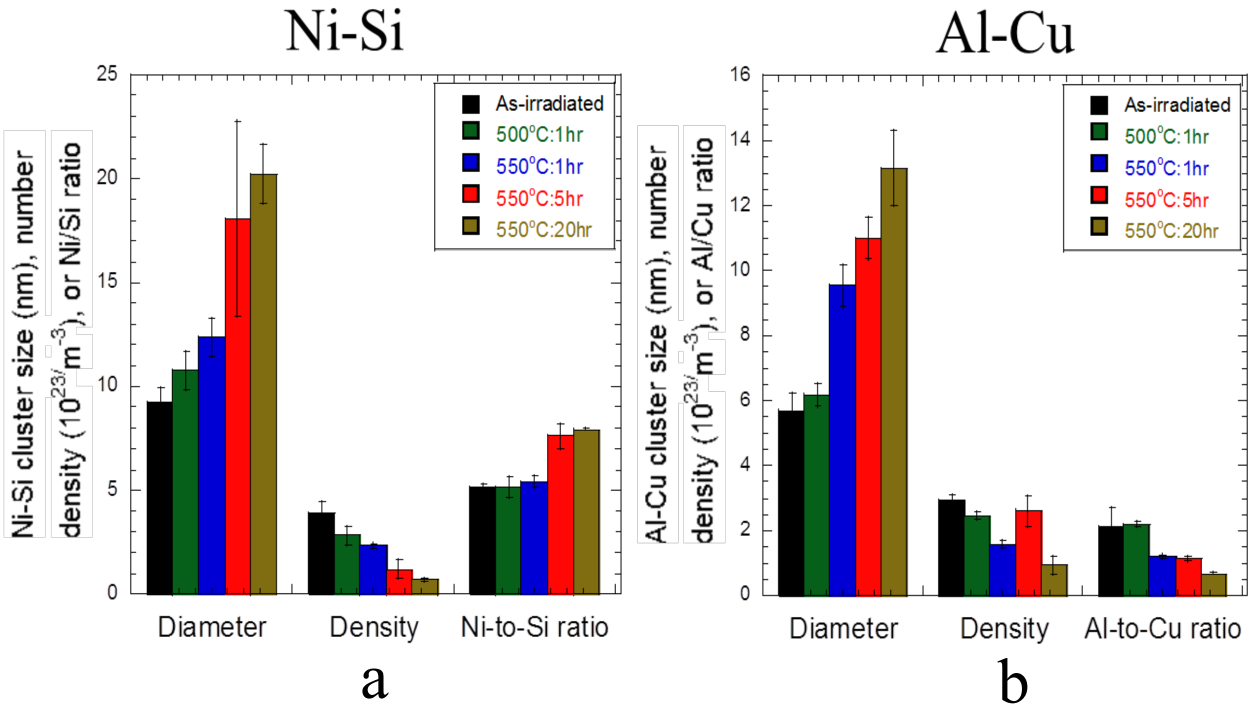

Figure 2. Comparison of solute cluster size, density and solute ratio in 304L SS irradiated to 5.9 dpa in BWR and after post-irradiation annealing at various conditions for (a) Ni-Si clusters, and (b) Al-Cu clusters.

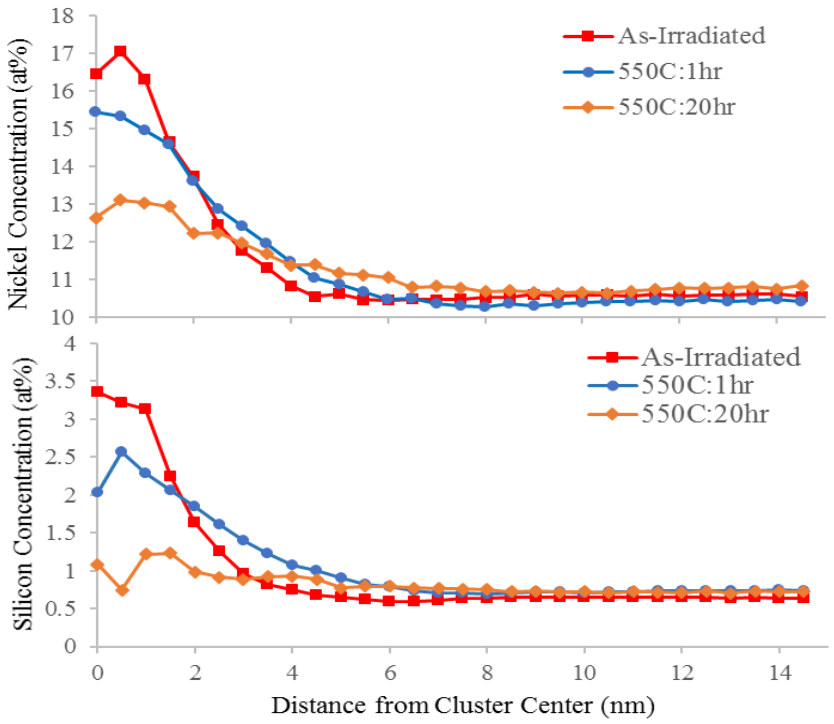

Figure 4-4. Composition of the Ni-Si clusters in the as-irradiated 304L SS and their evolution after post-irradiation annealing at 550°C:1h and 550°C:20h.

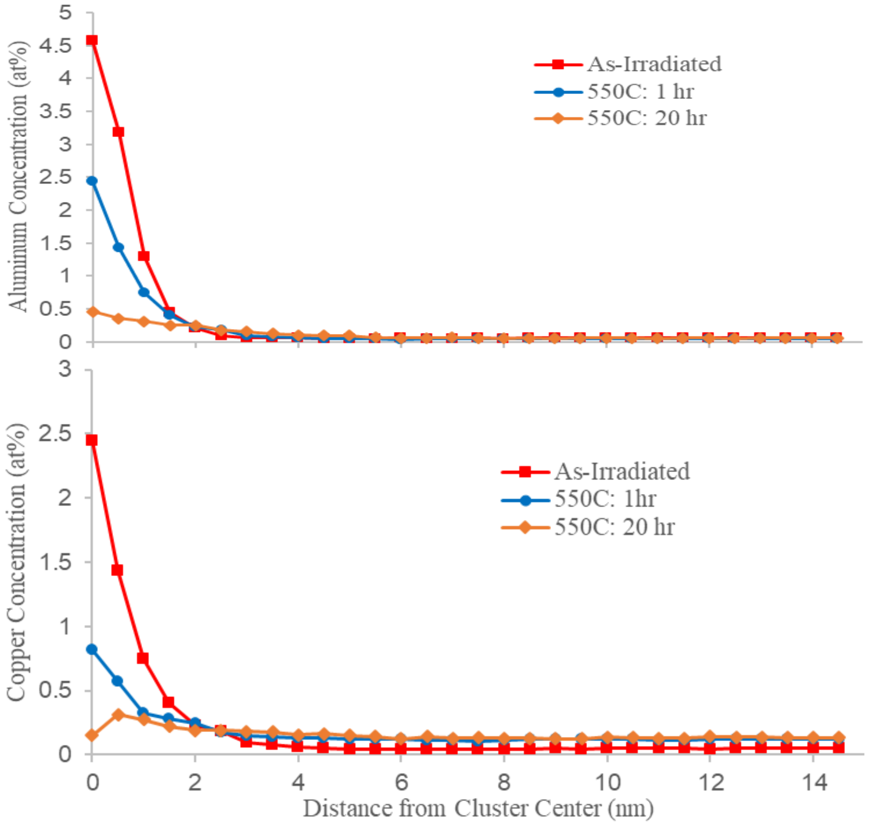

Figure 4-5. Composition of the Al-Cu clusters in the as-irradiated 304L SS and their evolution after post-irradiation annealing at 550°C:1h and 550°C:20h.

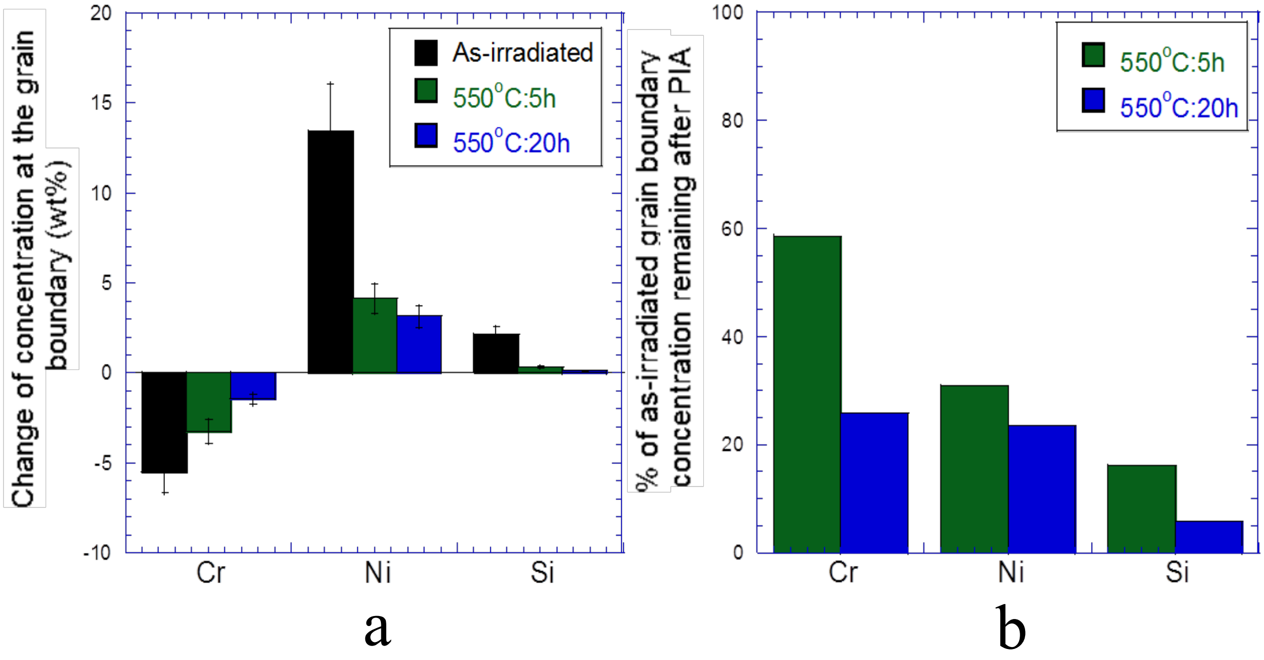

Figure 4-6. Post-irradiation annealing effect on radiation-induced segregation of (a) Cr, Ni and Si, and (b) remaining RIS of Cr, Ni and Si after post-irradiation annealing.

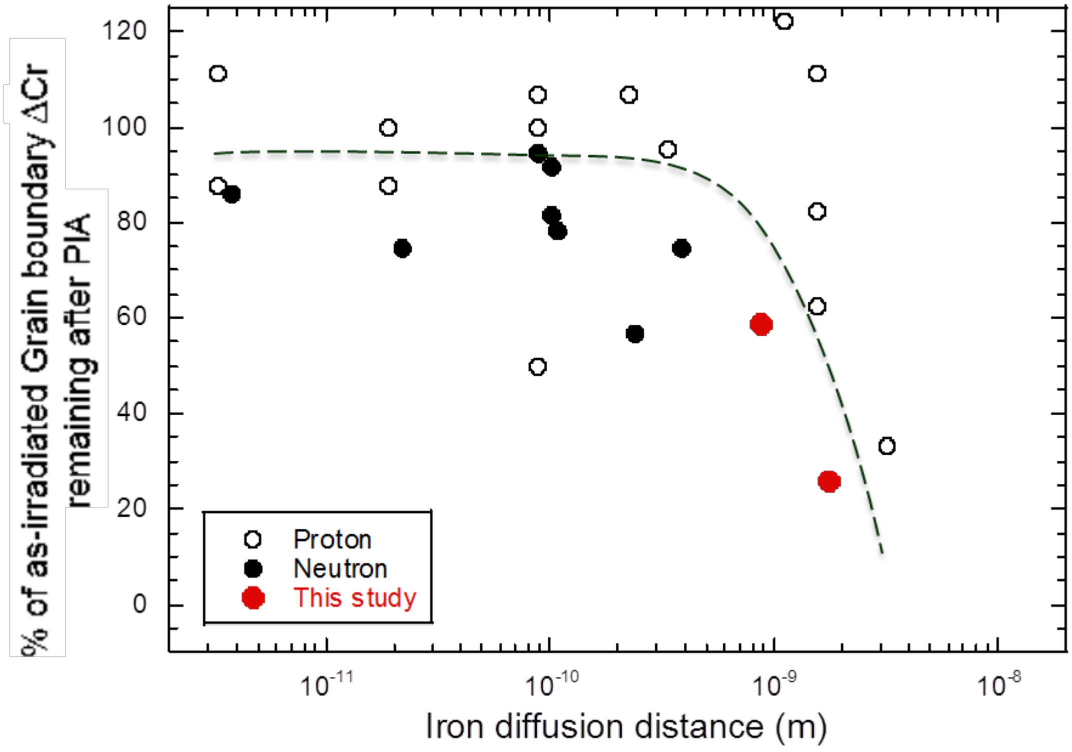

Figure 4-7. Comparison of RIS remaining with literature data.

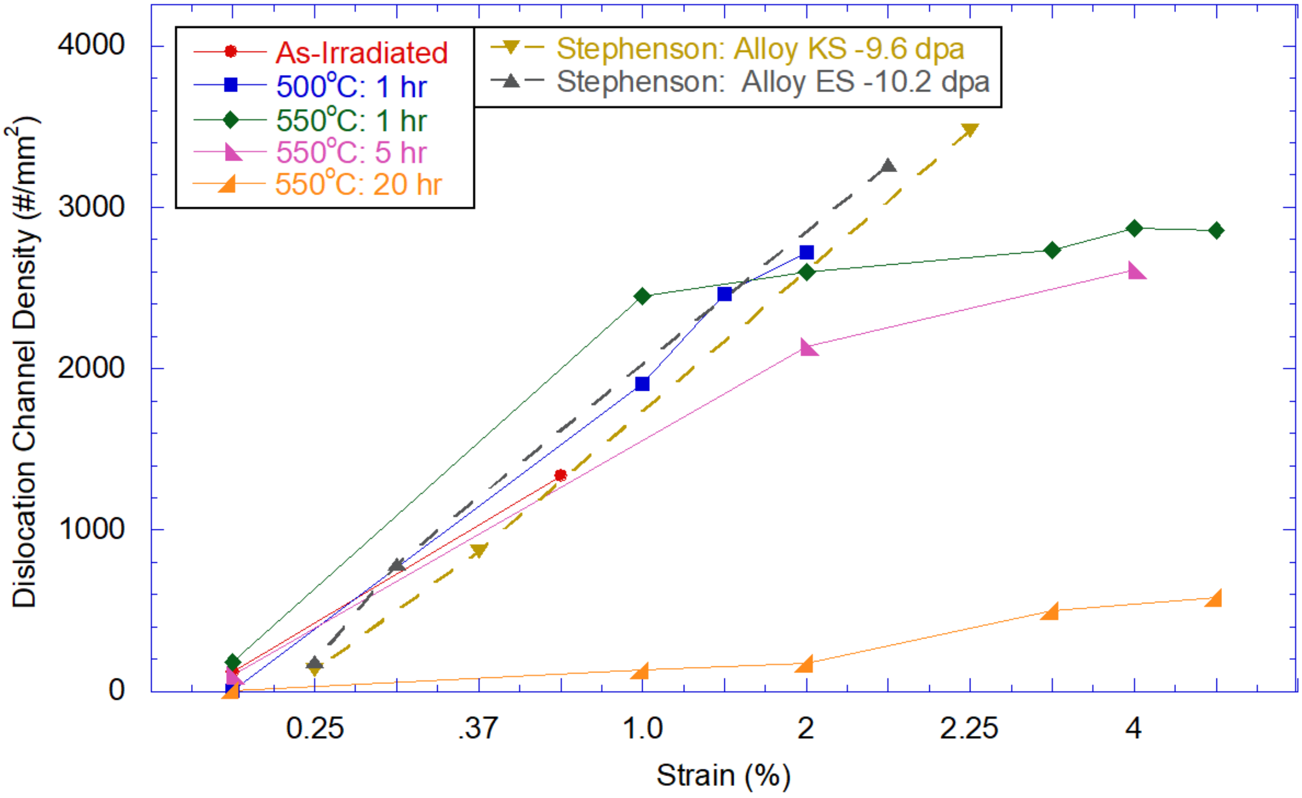

Figure 4-8. Comparison of the measured dislocation channel density as compared to prior work by Stephenson *et al.*[22].

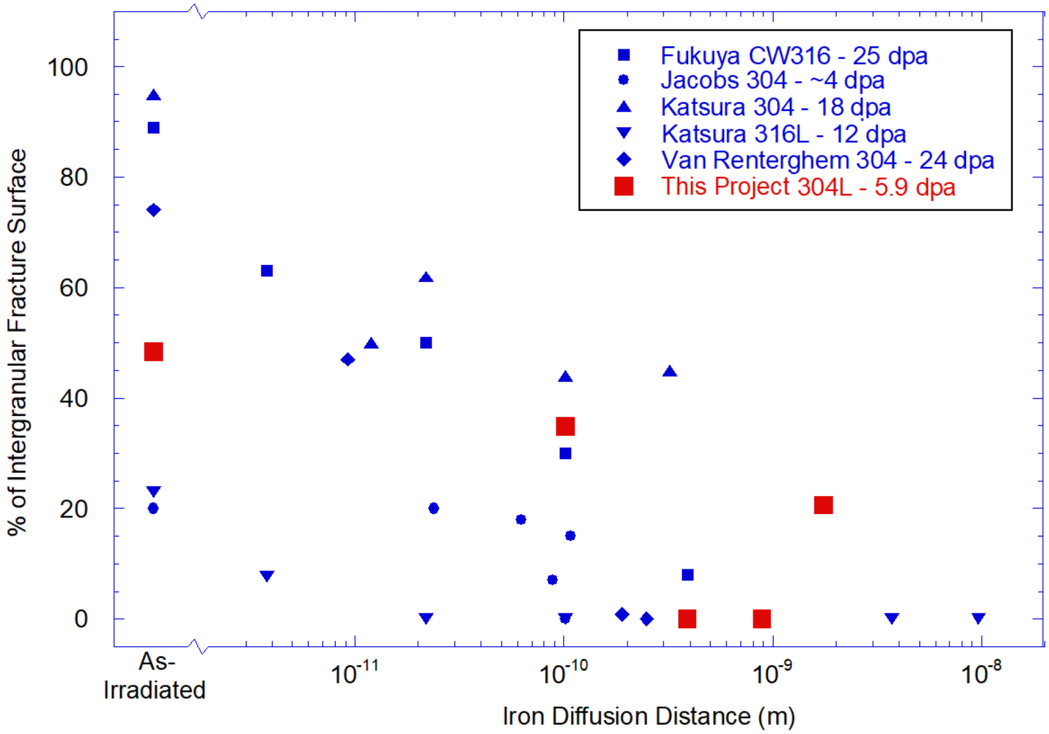

Figure 4-9. Comparison of the measured intergranular fracture area as a percentage of the final fracture area from this project and several neutron-irradiated PIA specimens in the literature.

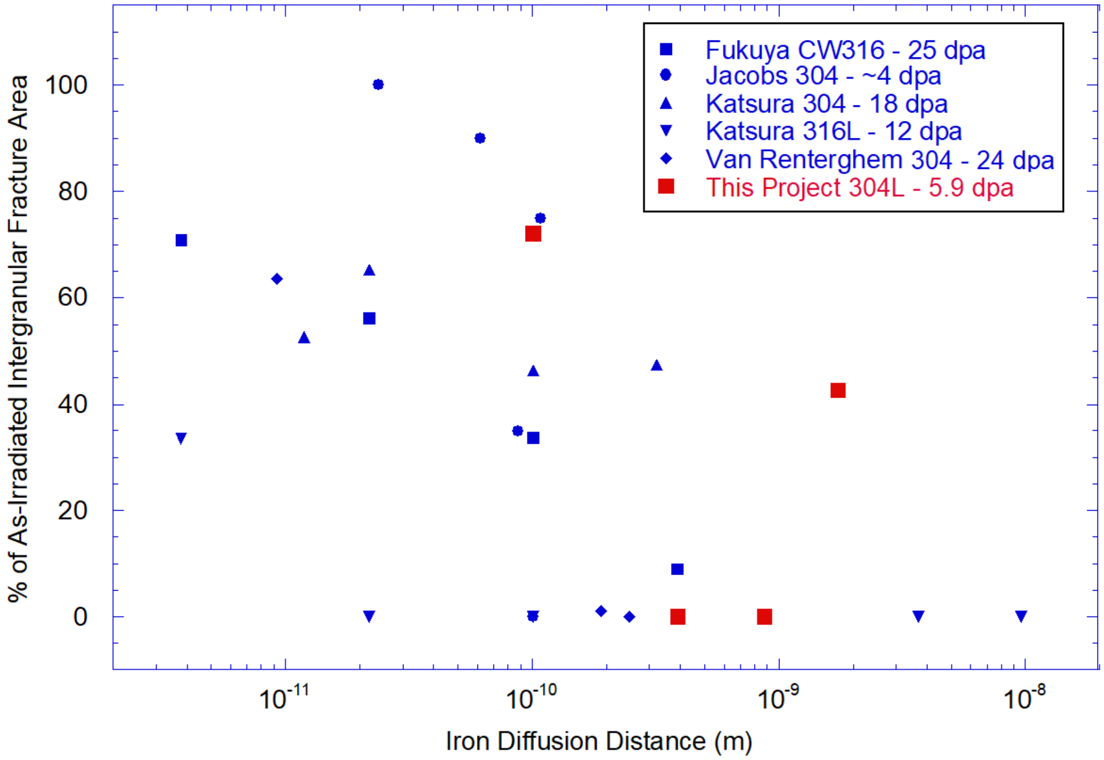

Figure 4-10. Comparison of the measured intergranular fracture area as a percentage of the as-irradiated condition from this project and several neutron-irradiated PIA specimens in the literature.

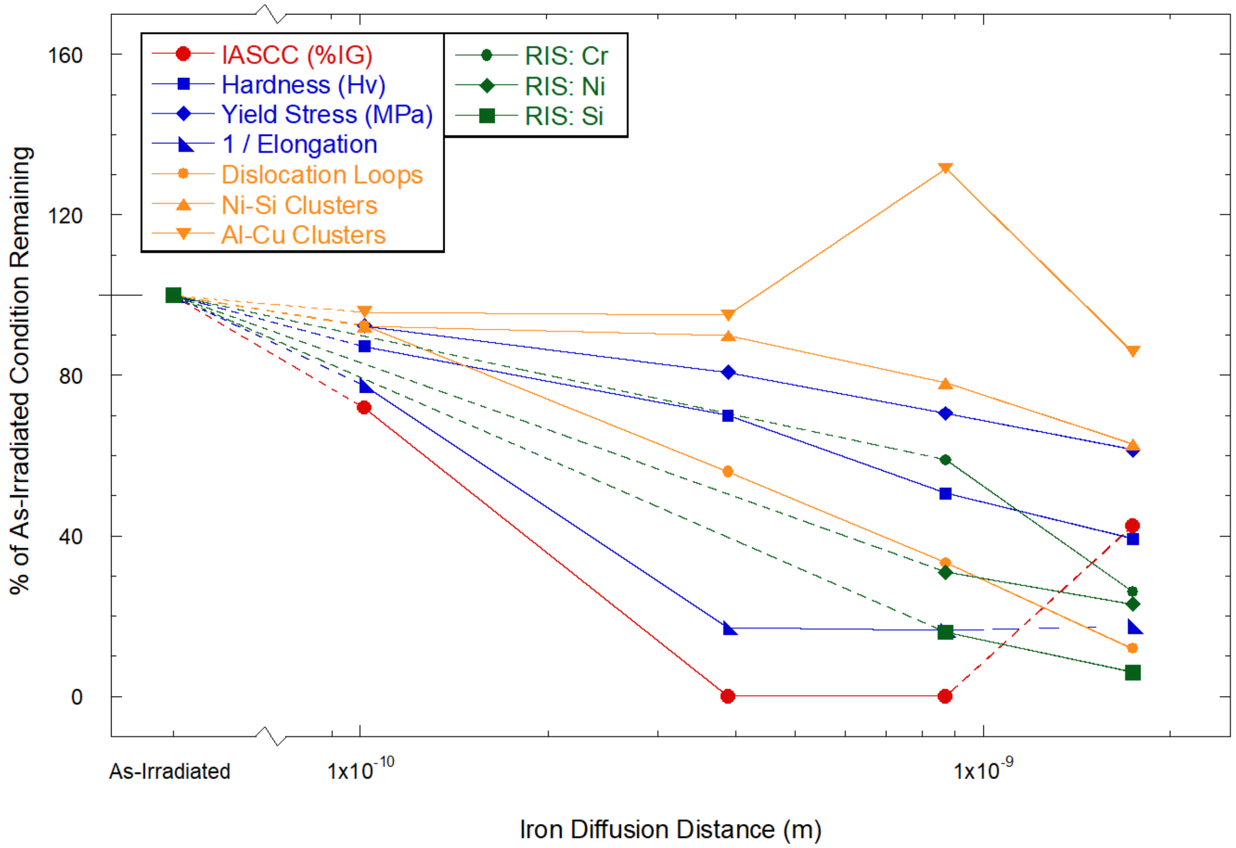

Figure 4-11. Comparison of the IASCC susceptibility to the mechanical properties and irradiated microstructure as a percentage of the as-irradiated condition.

5. Conclusions

Microstructural examination, CERT, and CGR tests were conducted on a 304L stainless steel irradiated to 5.9 dpa in the Barseback 1 BWR in Sweden, both in the as-irradiated condition and following annealing treatments of 500°C: 1 hr, 550°C: 1 hr, 550°C: 5 hr, and 550°C: 20 hr. This project was designed to identify the key factors affecting IASCC initiation and growth, through evaluating the mitigation behavior following PIA treatments. Due to significant delays in the delivery of the required irradiated specimens, the originally planned major objectives were not met, however, major findings include:

- PIA treatments greater than 450°C were highly effective in reducing the irradiated-induced microstructural defects in the as-received material.
    - The irradiation hardening for the project material was unaffected by annealing treatments at 450°C, but was incrementally removed at higher temperatures and times, leading to full removal after 600°C: 20 hr.
    - The average dislocation loop size does not change significantly after PIA at 500°C:1h and 550°C, 1 and 5 hr but the number density decreases after PIA. The number density becomes negligible after PIA at 550°C:20h. Preference annihilation of small dislocation loops and coarsening of large loops were observed after PIA at 500°C:1h, which is consistent with the thermal annihilation theory. However, this was not observed after annealing at 550°C.
    - Both Ni-Si and Al-Cu clusters decrease in density and increase in size after PIA due to thermal diffusion of solute atoms. The ratio of Ni to Si increases after PIA, as Si is a faster diffuser than Ni.
    - Significant recovery of Cr and Ni was observed after PIA at 550°C:5h but neither Cr nor Ni was fully recovered after 550°C:20h.
- PIA treatments at 500°C: 1 hr, 550°C: 1, 5, and 20 hr were observed to significantly change the deformation behavior of the as-received material during CERT experiments. Furthermore, the 550°C: 20 hr condition was observed to significantly alter the measured localized deformation
    - The yield stress of the alloy following PIA treatments was observed to closely correspond to the measured changes in the irradiation hardness.
    - Elongation was observed to by slightly increased after annealing at 500°C: 1hr to ~125% of the as-irradiated specimen. However, elongation was significantly enhanced after annealing at 550°C, with 1 hr and 20 hr annealing having ~550% of the as-irradiated elongation.
    - The density of dislocation channels with strain appeared largely unchanged after annealing at 500°C: 1hr and 550°C: 1hr as compared to the as-irradiated condition, but the channel density was slightly decreased after PIA 550°C: 5hr, and was significantly reduced for the 550°C: 20 hr condition.

    - The percentage of discontinuous channel-grain boundary interaction sites was observed to remain relatively constant, regardless of PIA or strain. Thus, there was no observed trend in the ratio discontinuous to continuous channel-grain boundary interaction sites following the annealing treatments.
    - Hardening is best described using a root-mean-square model for superposition of obstacles and was dominated by dislocation loops. A least squares analysis revealed that the hardening coefficient of loops was ~0.2. That for Ni-Si precipitates was less half this value and that for Al-Cu clusters was even smaller.
- PIA treatments at 550^{o}C: 1 hr and 550^{o}C: 5 hr were observed to fully remove the IASCC susceptibility of the as-received material. However, annealing at 550^{o}C: 20 hr showed susceptibility to IG SCC, which is unexpected.
    - As compared to other neutron-irradiated material in literature, our as-received material was observed to have a moderate IASCC susceptibility with an intergranular fracture of 48.4%. This relative area was observed to decrease with increasing annealing, but there was a measured 20.6% after 550^{o}C: 20 hr, which appears higher than the observed trend in literature.
    - Reduction in area of the final fracture surfaces was significantly enhanced by the annealing treatments, thus representing an increased ductility of the material and lower IASCC susceptibility following annealing.
    - As the measured CGR of an RCT specimen after annealing at 550^{o}C:20hr seem to be lower than similar as-irradiated specimens at similar K values from literature, thus indicating some mitigation from the PIA. However, as the CGR data in literature is observed to have a high degree of scatter, this comparison is to be taken in caution with the lack of an as-irradiated benchmark CGR for our material.

From these conclusions, it is apparent that PIA treatments had a significant impact on the irradiated microstructure, dislocation channeling, and cracking susceptibility. However, while the irradiation hardening and microstructural defect populations were removed in a manner similarly to previous results in literature, the as-received material appeared to be more resistant to the mitigation of IASCC susceptibility as compared to previous literature studies.

6. References

[1] G. Was and P. Andresen, "Stress Corrosion Cracking Behavior of Alloys in Aggressive Nuclear Reactor Core Environments," *Corrosion*, vol. 63, pp. 19–45, 2007.

[2] R. Katsura, Y. Ishiyama, N. Yokota, T. Kato, K. Nakata, K. Fukuya, H. Sakamoto, and K. Asano, "Post-Irradiation Annealing Effect of Austenitic Stainless Steels on IASCC," *Corrosion*, no. 132, 1998.

[3] K. Fukuya, M. Nakano, K. Fujii, T. Torimaru, and Y. Kitsunai, "Separation of Microstructural and Microchemical Effects in Irradiation Assisted Stress Corrosion Cracking using Post-irradiation Annealing," *J. Nucl. Sci. Technol.*, vol. 41, no. 12, pp. 1218–1227, Dec. 2004.

[4] A. Jacobs and S. Dumbill, "Effects of low-temperature annealing on the microstructure and grain boundary chemistry of irradiated type 304SS and correlations with IASCC resistance," in *7th International Conference on Environmental Degradation of Materials in Nuclear Power Systems*, 1995, pp. 1021–1031.

[5] A. Jacobs, G. Wozadlo, and G. Gordon, "Low-Temperature Annealing: A Process to Mitigate Irradiation-Assisted Stress Corrosion Cracking," *Corrosion*, vol. 51, no. 10, pp. 731–737, Oct. 1995.

[6] J. Busby, G. Was, and E. Kenik, "Isolating the effect of radiation-induced segregation in irradiation-assisted stress corrosion cracking of austenitic stainless steels," *J. Nucl. Mater.*, vol. 302, no. 1, pp. 20–40, Apr. 2002.

[7] Z. Jiao, Y. Chen, J. Hesterberg, E. Marquis, and G. Was, "Post-Irradiation Annealing in Mitigation of IASCC of Proton-Irradiated Stainless Steel," in *16th International Conference on Environmental Degradation*, 2013, vol. 2.

[8] W. Van Renterghem, A. Al Mazouzi, and S. Van Dyck, "Influence of post irradiation annealing on the mechanical properties and defect structure of AISI 304 steel," *J. Nucl. Mater.*, vol. 413, no. 2, pp. 95–102, Jun. 2011.

[9] W. Van Renterghem, M. Konstantinovic, and M. Vankeerberghen, "Evolution of the radiation-induced defect structure in 316 type stainless steel after post-irradiation annealing," *J. Nucl. Mater.*, vol. 452, pp. 158–165, 2014.

[10] Y. Chimi, "Final Report on the BWR Crack Growth Rate Investigation IFA-745," HWR-1079, 2013.

[11] T. Onchi, K. Dohi, N. Soneda, M. Navas, and M. Castaño, "Mechanism of irradiation assisted stress corrosion crack initiation in thermally sensitized 304 stainless steel," *J. Nucl. Mater.*, vol. 340, no. 2–3, pp. 219–236, Apr. 2005.

[12] Z. Jiao and G. Was, "Localized deformation and IASCC initiation in austenitic stainless steels," *J. Nucl. Mater.*, vol. 382, no. 2–3, pp. 203–209, Dec. 2008.

[13] Z. Jiao and G. Was, "The role of irradiated microstructure in the localized deformation of austenitic stainless steels," *J. Nucl. Mater.*, vol. 407, no. 1, pp. 34–43, 2010.

[14] M. McMurtrey, G. Was, L. Patrick, and D. Farkas, "Relationship between localized strain and irradiation assisted stress corrosion cracking in an austenitic alloy," *Mater. Sci. Eng. A*, vol. 528, no. 10–11, pp. 3730–3740, Apr. 2011.

[15] M. McMurtrey, G. Was, B. Cui, I. Robertson, L. Smith, and D. Farkas, "Strain localization at dislocation channel-grain boundary intersections in irradiated stainless steel," *Int. J. Plast.*, vol. 56, pp. 219–231, 2014.

[16] M. McMurtrey and G. Was, "Quantification of Stress and Strain States at Dislocation

Channel-Grain Boundary Intersections and their Relation to IASCC in Austenitic Steels," in *Proceedings of 16th International Conference on Environmental Degradation of Materials in Nuclear Power Systems-Water Reactors*, 2014.

[17] Z. Jiao, M. McMurtrey, and G. Was, "Strain-induced precipitate dissolution in an irradiated austenitic alloy," *Scr. Mater.*, vol. 65, no. 2, pp. 159–162, Jul. 2011.

[18] N. Soneda, K. Nishida, and P. Chou, "Characterization of solute atom distribution in grain interior of neutron-irradiated 304L and 304 stainless steels," 2011.

[19] J. Busby, M. Hash, and G. Was, "The relationship between hardness and yield stress in irradiated austenitic and ferritic steels," *J. Nucl. Mater.*, vol. 336, no. 2–3, pp. 267–278, Feb. 2005.

[20] M. Gussev, K. Field, and J. Busby, "Deformation localization and dislocation channel dynamics in neutron-irradiated austenitic stainless steels," *J. Nucl. Mater.*, vol. 460, pp. 139–152, 2015.

[21] D. Edwards and B. Singh, "Evolution of cleared channels in neutron-irradiated pure copper as a function of tensile strain," *J. Nucl. Mater.*, vol. 329–333, pp. 1072–1077, 2004.

[22] K. Stephenson and G. Was, "Development of a Novel SCC Test for Isolating Crack Initiation in Neutron Irradiated Stainless Steel," in *17th International Conference on Environmental Degradation*, 2015.

[23] K. Asano, R. Katsura, M. Kodama, S. Nishimura, K. Fukuya, and K. Nakata, "Post-irradiation annealing effects on hardness and intergranular corrosion in type 304 stainless steel," in *7th International Conference on Environmental Degradation of Materials in Nuclear Power Systems*, 1995, pp. 1033–1042.

[24] B. Burton, "Theoretical analysis of annealing behaviour of mixed distributions of dislocation loops , voids , and gas bubbles: comparison with annealing behaviour of irradiated reactor component irradiated reactor component," *Mater. Sci. Technol.*, vol. 8, pp. 602–610, 1992.

[25] J. Arunkumar, C. David, K. Nair, B. Panigrahi, and C. Sundar, "Application of Resonant Nuclear Reactions for Studying the Diffusion of Nitrogen and Silicon in Ti-Modified Stainless Steel," *Adv. Mater. Sci. Eng.*, pp. 1–6, 2012.

[26] G. Salje and M. Kniepmeier, "The Diffusion and Solubility of Copper in Iron," *J. Appl. Phys.*, vol. 48, p. 1833, 1977.

[27] Z. Tokei, J. Bernardini, P. Gas, and D. Beke, "Volume Diffusion of Iron in Fe3Al: Influence of Ordering," *Acta Mater.*, vol. 45, no. 2, pp. 541–546, 1997.

[28] A. Seeger, "On the theory of radiation damage and radiation hardening," in *Proceedings of 2nd United Nations International Conference on the Peaceful Uses of Atomic Energy: Volume 6*, 1958, vol. 48, no. 12, p. 250.

[29] G. Odette and G. Lucas, "Recent progress in understanding reactor pressure vessel steel embrittlement," *Radiat. Eff. Defects Solids*, vol. 144, no. 1–4, pp. 189–231, Aug. 1998.

[30] G. Was, *Fundamentals of Radiation Materials Science*. 2007.

[31] T. Toyama, Y. Nozawa, W. Van Renterghem, Y. Matsukawa, M. Hatakeyama, Y. Nagai, A. Al Mazouzi, and S. Van Dyck, "Irradiation-induced precipitates in a neutron irradiated 304 stainless steel studied by three-dimensional atom probe," *J. Nucl. Mater.*, vol. 418, no. 1–3, pp. 62–68, Nov. 2011.

[32] T. Allen, J. Busby, E. Kenik, and G. Was, "Modeling the effect of irradiation and post-irradiation annealing on grain boundary composition in austenitic Fe-Cr-Ni alloys," in

Materials Research Society Symposium, 1998, vol. 52701998, pp. 291–298.

[33] F. Bergner, C. Pareige, M. Hernández-Mayoral, L. Malerba, and C. Heintze, "Application of a three-feature dispersed-barrier hardening model to neutron-irradiated Fe – Cr model alloys," *J. Nucl. Mater.*, vol. 448, no. 1–3, pp. 96–102, 2014.